MULTI-FRAGMENT DISINTEGRATIONS IN INTERMEDIATE ENERGY NUCLEUS-NUCLEUS COLLISIONS

By

Yeongduk Kim

A DISSERTATION

Submitted to
Michigan State University
in partial fulfillment of the requirements
for the degree of

DOCTOR OF PHILOSOPHY

Department of Physics and Astronomy

1991

ABSTRACT

MULTI-FRAGMENT DISINTEGRATIONS IN INTERMEDIATE ENERGY NUCLEUS-NUCLEUS COLLISIONS

By

Yeongduk Kim

The possibility for the highly excited nuclear matter to break into multi-fragment final states has been predicted by various theoretical calculations. Experimental information about low-density nuclear equation of state may be obtainable from detailed studies of multi-fragment emission processes. A new low-threshold 4π charged particle detector array, the MSU Miniball, has been constructed for the study of multi-fragmentation. Intermediate mass fragment(IMF) emission has been studied using beams of ^{14}N at E/A=50MeV and ^{36}Ar at E/A=20,35MeV on ^{238}U and ^{197}Au targets. Most IMFs are emitted in central collisions characterized by large charged-particle multiplicities. Energy spectra and angular distributions indicate the non-equilibrium nature of IMF emission.

Time-scales for multi-fragment emission, key in distinguishing the various reaction mechanisms, have been studied using two-fragment correlation functions. The experimental two-fragment correlation functions were found to depend mainly on the reduced relative velocity, $v_{red} = v_{rel}/\sqrt{Z_1+Z_2}$, of the fragment pairs. It is therefore possible to sum over different pair combinations with little loss in resolution. From the comparisons of the inclusive experimental correlation functions with the classical expression of Koonin-Pratt formula, mean

emission times of the order of 100-200 fm/c have been extracted with about 50% uncertainty. Three-body Coulomb trajectory calculations were also performed to estimate the uncertainty from the interaction with the heavy residue. A more detailed study indicates that fragment emission in central collisions begins at the very early stages of the reaction and continues throughout the later equilibrated stages.

ACKNOWLEDGEMENT

I would like to express my heartful thanks to my advisor, Professor Claus-Konrad Gelbke, for his invaluable supervision over my research and support. Without his continuous encouragement, intuitive suggestions, and enthusiasm for best experiments, it would not have been possible for me to finish this thesis. I have learned how to do physics experiments right here NSCL from him. His advices at each time step of my research period have been always appropriate and critical.

Professor William Lynch deserves a great deal of recognition for his valuable advice during many experiments I worked on and helpful criticism on my research. Dr. Romualdo de Souza contributed a lot on this thesis through the construction of Miniball. I especially appreciate very much for his letters of recommendation. It was very pleasant to work with Dr. Nelson Carlin and I appreciate very much his help and suggestions on the Miniball project and sincere friendship.

I have greatly benefited from co-workers, Drs Betty Tsang, Tatsuya Murakami, and David Bowman in learning the computer programs for data acquisition and experimental skills. I want to thank very much Dr. Scott Pratt at University of Wisconsin for his support with a nice classical formula calculating correlation functions. I also appreciate Professor William Friedman for valuable discussions about time scales and IMF emission.

It has been a great pleasure working with the excellent NSCL staff; Dr. John Yurkon and Dennis Swan at detector lab. informed me on the techniques used in making Miniball and other detectors. Jack Ottarson was extremely helpful with Miniball design. Without his clever design work Miniball would be in a different shape. I appreciate greatly the assistance of Reg Ronningen, Dave Sanderson,

Ron Fox during the preparation for Miniball experiment. I want to thank Fred Denovich at Machine Shop, Mike Noe at Purchasing Dept., Orilla McHarris at Graphics, Jim Vincent at Electronics Shop and many other people I may forget to refer to here for their help.

I also acknowledge my fellow graduate students. I have had many valuable discussions with Wen-Guang Gong about correlation functions. Ziping Chen, Tapan Nayak, Hongming Xu, Fan Zhu, Larry Phair, Michael Lisa, Wen Chien Hsi have helped me and shared their knowledge and friendship with me, making my work much easier than it would have been without them.

Finally I sincerely thank my family in Korea; my parents, my brother(Yeongsoo), and my sister for their encouragement and support. When I felt very tired, I was always comforted by just thinking of them. It is a little sad that I have been away so long from my friends in Korea still struggling against the military government. I can never thank enough my wife, Junghee Cho, who has been my perfect companion with criticism, encouragement, and love even though she has been so busy with her own research and our daughter. Errie, who was born during my thesis experiment, deserves my greatest thanks for her husky laughs.

To my brother, Yeongsoo Kim

TABLE OF CONTENTS

LIST OF TABLES

LIST OF FIGURES

Chapter 1 Introduction

1.1 Overview

In this thesis we will present a study of intermediate mass fragment emission in nucleus-nucleus collisions at energies between E/A=20-50MeV. At lower energies(E/A≤10MeV) quasi-elastic, deep inelastic, and complete fusion reactions dominate the exit channel in proportions which depend on the impact parameter of the collision. At these energies mean-field dynamics plays a predominant role. In contrast, the experimental data at higher energies (E/A≥200MeV) indicate a geometrical picture (participant-spectator model), where the role of nucleon-nucleon collisions is more important. At intermediate energies, one observes the interplay between mean-field and nucleon-nucleon collisions and a transition between two different reaction mechanisms at lower and higher energies [Gel87,Lyn87]. In addition a new phenomenon may appear in this energy regime, namely the liquid-gas phase transition of highly excited nuclear matter [Cse86].

When the excitation energy is not too large, the decay of an excited nuclear system is believed to be a succession of evaporation steps of neutron and light charged particles (H and He isotopes). As the excitation energy is raised to about several MeV per nucleon, however, decays by intermediate mass fragment (IMF : Z=3-20) emission are predicted and observed to become important. For sufficiently high excitation energies, 4-5 MeV/nucleon, a number of theoretical calculations predict a simultaneous breakup of an excited nuclear system into several IMFs (Multi-fragmentation). This process should be qualitatively different from the conventional decay process like evaporation or fission. Over

the last decade there has bee a great deal of interest in multi-fragmentation processes because information about the low-density nuclear equation of state and the liquid-gas phase transition of nuclear matter may be obtainable from detailed studies of multi-fragment emission processes.

1.2 Theories of nuclear fragmentation

1.2.A Nuclear equation of state : liquid-gas phase transition

The thermodynamical properties of nuclear matter at finite temperatures have been studied to investigate the nuclear equation of state at low density($\rho<\rho_0$) [Sau76]. A simple pedagogical example of the nuclear equation of state assuming Skyrme-type interaction can be written as a virial expansion in density ρ [Jaq83],

$$P = \rho kT - a_0\rho^2 + 2a_3\rho^3, \qquad (1.1)$$

where P is the pressure, T is temperature, and a_0 and a_3 are constants related to the binding energy of a nucleon and normal nuclear density. The first term represents the pressure from kinetic motion of the nucleons. The second and third terms arise from the nuclear interaction; the reduction in pressure due to long range attractive interaction and increase in pressure due to short range repulsion between nucleons respectively. The isotherms of this equation of state [Sau76] are similar to those of Van der Waals gas as shown in Figure 1.1 with the critical point at $T_C \approx 18$MeV and $\rho_C \approx 0.3\rho_0$. The possibility of a liquid-gas phase

transition of excited nuclear matter was conjectured from this analogy [Sau76,Dan79], but how to detect this effect experimentally was not clear.

The dispute about the possibility of the liquid-gas phase transition and multi-fragmentation of low density nuclear matter has been stimulated by the interpretation of the experimental data on the mass distribution measured for ultrarelativistic proton induced reactions by Purdue Group [Fin82,Min82]. The mass distribution for the IMFs was measured and rather well described by a power law, $\sigma_A \propto A^{-\tau}$, with critical exponent τ=2.64. Discussing the analogy of the power-law behavior with the general clustering models like a droplet model by Fisher and a percolation model [Sta79], they concluded that "fragments are formed statistically in the multibody breakup of a highly excited nuclear remnant" [Fin82]. In one reaction scenario that leads to such a phase mixture, the energetic collisions of two heavy nuclei can generate a gas of unbound and heated nucleons. As the system cools and expands, nuclear binding could cause some of the nucleons to clump into IMF's; these "liquid drops" are imbedded in the remaining gas. The phase transition continues and the IMF's present at breakup can be detected [Jaq83]. According to the model of [Fis67], the size of the liquid drop formed inside the excited nuclear matter at and below the critical point can be estimated to have the distribution [Sie83,Pan84],

$$P_A \propto A^{-\tau} \exp(-b(T)A^{2/3}), \qquad (1.2)$$

where A is the fragment size, b(T) is a measure of the surface tension depending on temperature, and τ is the critical exponent. At the critical point this distribution becomes $P_A \propto A^{-\tau}$, which was the basis for the Purdue Group's conclusion.

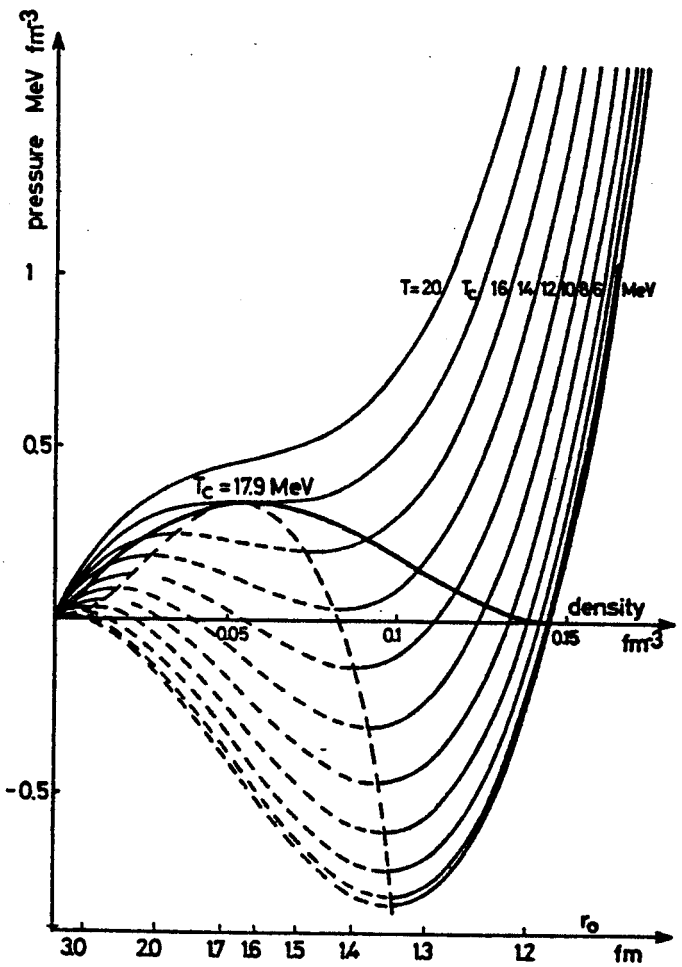

Figure 1.1 Equation of state for nuclear matter with the Skyrme force. The solid lines show the pressure of nuclear matter as a function of the density for various fixed temperatures(isotherms). The unstable states of the homogeneous system are indicated by the dashed lines [from Sau76].

This interpretation stimulated many experimental measurements of IMF emission and theoretical studies of multi-fragmentation. Before long, similar fragment mass distributions have also been observed in heavy-ion experiments at high energy [Gut82] and intermediate energy [Chi83] nucleus-nucleus reactions. By fitting the IMF mass distributions with eq. 1.2 and fragment energy spectra with a Boltzmann distribution to obtain the fragment temperature T, Panagiotou et al. obtained a relationship between these two quantities to obtain the "critical exponent" parameter τ for the available data which existed over a large range of incident energies and projectile target combinations [Pan84] in an attempt to find an experimental evidence of a phase transition. However, the power law behavior of the mass distributions proved to be an ambiguous signature of the phase transition; similar behavior has been predicted from completely different theoretical approaches based upon the percolation model [Bau86], or the sequential decay of an excited compound nucleus [Fri83]. It is now clear that we need more exclusive experimental data than the inclusive mass distribution to understand the phenomenon of multi-fragmentation.

A different picture of multi-fragmentation was presented by Bertsch and Siemens [Ber83]. The solid curve in Figure 1.2 shows the S=0 isentrope for a schematic nuclear equation of state. The left hatched area is the mechanical instability region where the compressibility ($\kappa = n \frac{\partial P}{\partial n}\Big|_S$) is negative (isentropic spinodal region). In this spinodal region a local accumulation of density would lead to a lower pressure, which causes more matter to flow into the high-density region leading a separation into liquid (high density) and gaseous (low density) phases. If the initial condition is to the right of the dashed line (overstressed zone), the system has enough energy to expand into the unstable region (fragmentation zone). A possible reaction trajectory for a heavy-ion collision reaching the unstable region has been drawn as a dashed line (details of the

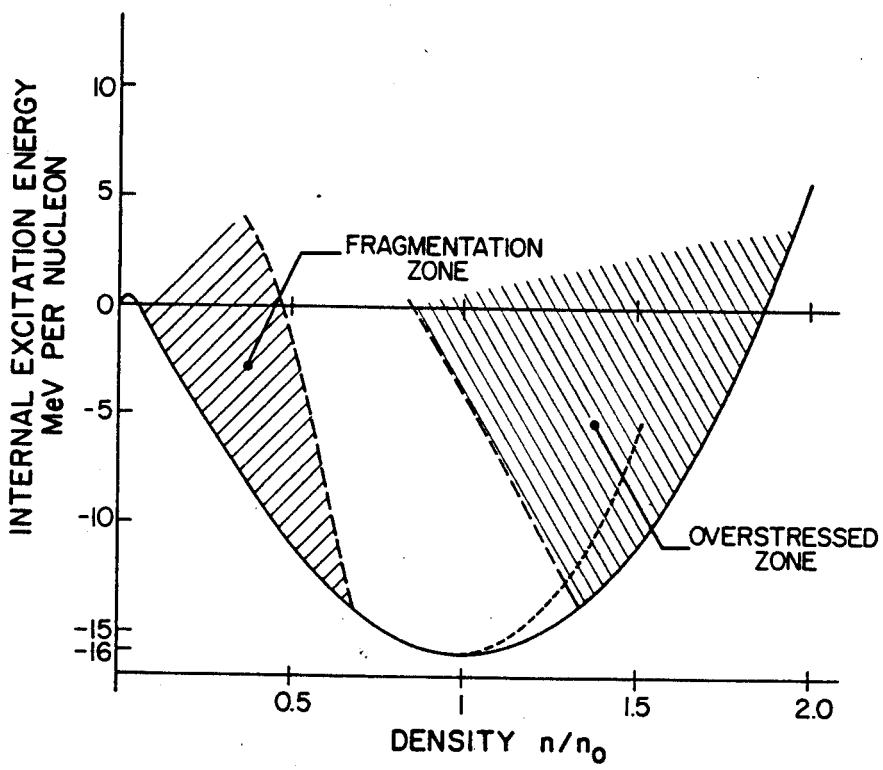

Figure 1.2 Instabilities of nuclear matter. Left grating:region of hydrodynamic instability,$(\frac{\partial P}{\partial n})_S<0$. Right grating: initial conditions leading to breakup after expansion [from Ber83].

considerations behind this curve can be found in reference [Ber83]). In this region instablities can grow exponentially from small amplitude, thus can split the system into liquid and gas phases rapidly. The possibility of reaching the fragmentation zone via heavy ion collisions presents a persuasive argument for investigating multi-fragmentation process in such collisions.

1.2.B Microscopic Models

The schematic arguments described in the previous section predict the existence of multi-fragmentation processes. A detailed investigations of fragmentation processes requestes theories that can be compared directly with the experimental observables. Such a quantitative comparisons are only provided by microscopic simulations of nucleus-nucleus collisions, in which one can introduce finite size effects, surface and Coulomb energy effects, and a reasonable dissipative dynamics [Sur89].

In most statistical multi-fragmentation models, the basic assumption is that a compound nucleus has been formed with given excitation energy, angular momentum and parity. Once formed, such a nucleus is assumed to decay according to the statistical weights of the various allowed decay configurations. Bondorf et al. and Gross et al. predict the onset of multifragmentation at temparatures of about 5-6 MeV [Bon85b,Gro86] within canonical and microcanonical treatments respectively. Recently Friedman explored multi-fragmentation with an evaporation model of an expanding nuclei. This calculations predict a multi-fragment rapid massive cluster formation for an excitation energy of about 1.5 GeV in a mass 190 system [Fri90]. However, statistical calculations generally have several limitations : (1) Thermodynamical equilibrium is a priori assumed, while the experimental angular distributions of

IMFs indicate nonequilibrium emissions, (2) The formation step of the outgoing fragments is not described due to the lack of dynamical effects.

A number of microscopic dynamical calculations indicate that the reaction trajectories of excited nuclear systems produced in heavy-ion collisions may indeed enter the mechanical instablity region [Vic85,Boa86,Sur89], in which density fluctuations can grow exponentially [Boa90a]. The initial conditions leading to evaporation, multi-fragmentation and total vaporization have been studied by mapping reaction trajectories on the phase diagram [Vic85,Boa86,Sur89]. Recent calculations for Ca+Ca collisions at b=0fm estimate a multi-fragmentation threshold at around E/A ≈ 30-35 MeV [Sur89]. These calculations, however, may not contain sufficient fluctuations to describe the fragmentation process. For this reason, it is also interesting to explore statistical fragmentation approaches.

1.3 Detection of multi-fragment emission

A number of experiments on the IMF production in heavy-ion reactions have been performed at intermediate energies for a variety of systems and energies [Chi83, FieJ84, FieJ86, Jac87, Bow87]. To identify IMF emission as a multi-fragmentation clearly, however, one must examine the multi-fragment final states on an event-by-event basis. First experimental evidence of multi-fragment emission was established from Plastic Ball data obtained by the GSI/LBL collaboration. The Plastic Ball/Wall [Bad82] consists of 815 CaF_2-plastic telescope modules covering the angular region from $10° \leq \theta_{lab} \leq 160°$. For Au+Au collisions at E/A=200MeV, IMFs($3 \leq Z \leq 10$) were detected at $\theta_{lab} \leq 30°$ corresponding to the forward hemisphere in the center of mass system. These measurements were performed with an energy threshold of E_{th}/A=35-40MeV.

Figure 1.3 shows IMF multiplicity distributions gated on various participant charge multiplicities thereby representing different regions of impact parameter [Jac87]. On average, 3-4 fragments were detected per central collision. Therefore the data clearly established the existence of multi-fragment emission. Also, the data show a smooth increase in the probability of IMF emission as the participant charge multiplicity increases or as the impact parameter decreases.

At intermediate energies, a few experimental measurements of multi-fragment emission have been performed with relatively restricted phase space coverage. Bougault et al. studied Kr+Au and Kr+Ag at E/A=43MeV using multi-detector system covering about 50% of 4π [Bou88]. They detected IMF multiplicities as large as $N_{IMF} = 6$ with non-negligible cross sections. They concluded that even though the multi-fragmentation is observed in these measurements, it does not result from a simultaneous explosion of the total system. Recently Trockel et al. reported multi-fragment emission from O + Au at E/A = 84 MeV with mean IMF multiplicity about 0.5 [Tro89,Fri90]. Comparisons of data with both statistical multi-fragmentation calculations [Bon85b] and calculations with a sequential binary decay model [Cha88] were inconclusive. Earlier a series of experiments have been performed by Berkeley Group using reverse kinematics. From the coincident measurement of fission fragments for La + C at E/A = 50 MeV, they concluded that sequential binary decay dominates this reaction with an estimated excitation energy of the composite system of about 280 MeV [Bow87]. This conclusion was challenged by Gross [Gro88]. He showed that his microcanonical multi-fragmentation model could reproduce the experimental binary charge correlations reasonably, and concluded that the real cranking should be observable at excitation energy above 600 MeV for nuclei in this mass range.

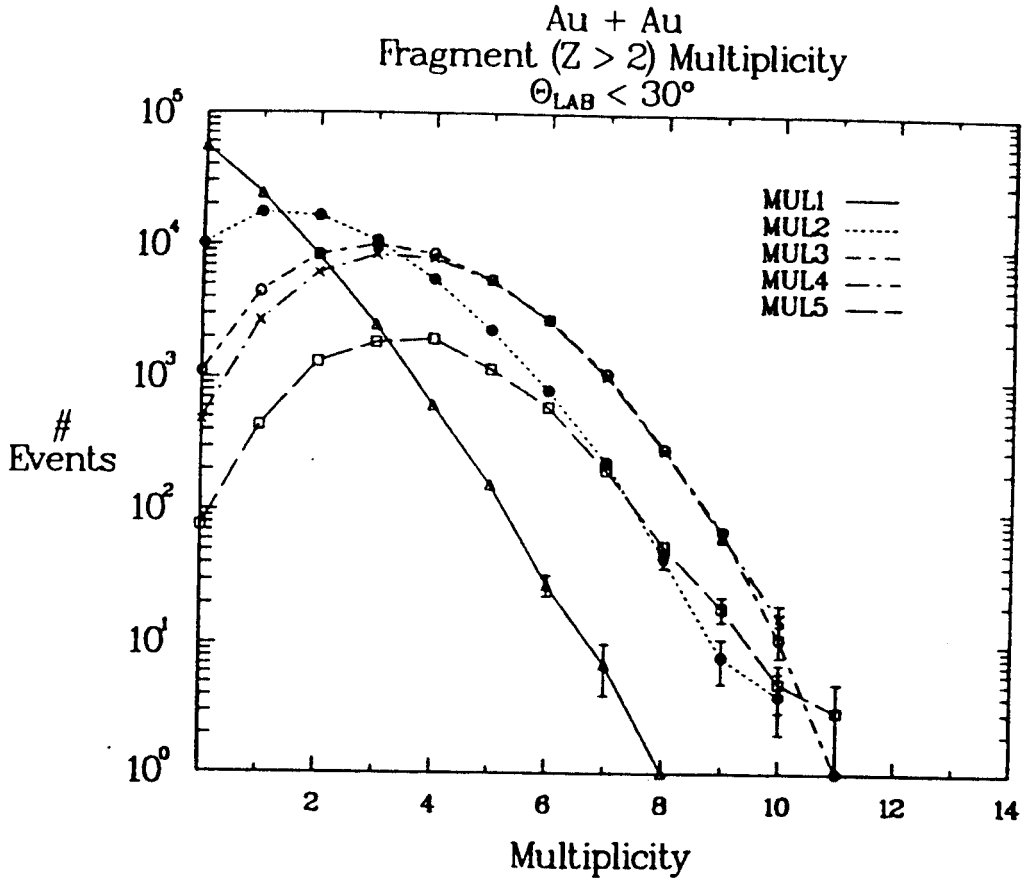

Figure 1.3 IMF multiplicity distributions for Au + Au at E/A=200MeV. Five participant charge multiplicity bins increase from MUL1 to MUL5 [from Jac87].

It has become clear that more exclusive experimental data are needed for an understanding of multi-fragment emission processes. For example, impact parameter selection could eliminate less interesting peripheral collisions. A systematic study of the excitation function of IMF production could reveal the onset of multi-fragmentation reactions. Dynamical calculations suggest that the probability or onset for multi-fragmentation may be sensitive to the nuclear equation of state at low density [Sur89]. Therefore we can expect to gain information about the equation of state of low density nuclear matter from a detailed studies of the multi-fragment emission processes. The first task of the present work was to measure exclusively multi-fragment emissions with an apparatus of large phase space coverage.

1.4 Time scales of multi-fragment emission

At present, it is not clear that the theoretical calculations described in Section 1.2 predict final states which are different from final states predicted by conventional evaporation or fission like processes. In principle one cannot exclude the possibility that sequential multi-step binary decay mechanisms can generate multi-fragment final states [Mor88].

As pointed out by Bertsch [Ber83], the usual liquid-gas phase transition is a first order transition that applies to processes that occur slowly enough for an equilibrium to be established across a phase boundary. A lower limit for the time required for such decays is given by the time required for exponential growth of density fluctuations or the expansion of the nuclear system; this time scales are of the order of 50fm/c in dynamical calculations [Sur89,Boa90]. On the other hand, conventional evaporation-like binary decay assumes a nearly complete relaxation of the excited composite system between each decay. For example, the time scale

of fission at initial nuclear temperatures of about 5 MeV is estimated to be fo the order of 10^{-20}second or several thousand fm/c [Hil89]. The time scale for evaporative processes is predicted to be of the order of 1-5x10^{-21}($\approx$1000 fm/c) [DeY89]. Therefore key to experimental confirmation can be provided by the measurement of the fragment emission time scales for the breakup.

One of the first experimental time scale measurements were obtained by Trockel et. al. [Tro87]. They constructed correlation functions between heavy residues, fission fragments, and intermediate mass fragments as a function of relative velocity as shown in Figure 1.4. Comparing the IMF-IMF correlation functions with trajectory calculations, they extracted mean IMF emission times of the order of 300-1400fm/c (the mean emission time, τ, and the "half-life" for IMF emission, $\tau_{IMF-IMF}$, defined by [Tro87], are related by : $\tau = 1.44\tau_{IMF-IMF}$). The similar time scales of HR(heavy residue)-IMF and IMF-IMF decay processes led them to conclude a sequential nature of multi-fragment emission. However the range of possible time scales extracted is quite large in this measurement. A qualitatively similar result has been obtained by Bougault et. al. who quote a mean emission time 300fm/c without a corresponding estimate of the uncertainty [Bou89]. More experimental data are needed to explore these issues. The second part of this thesis will address this problem.

1.5 Organization of the thesis

We first performed an exploratory experiment to begin the investigation of the multi-fragment emission processes. In Chapter 2, we describe this experiment which combined the Dwarf Ball/Wall 4π phoswhich detector with two parallel plate avalanche counters(PPAC) [Bre77]. After this experiment, we began to develop our own 4π detector with improved characteristics. Chapter 3 explains

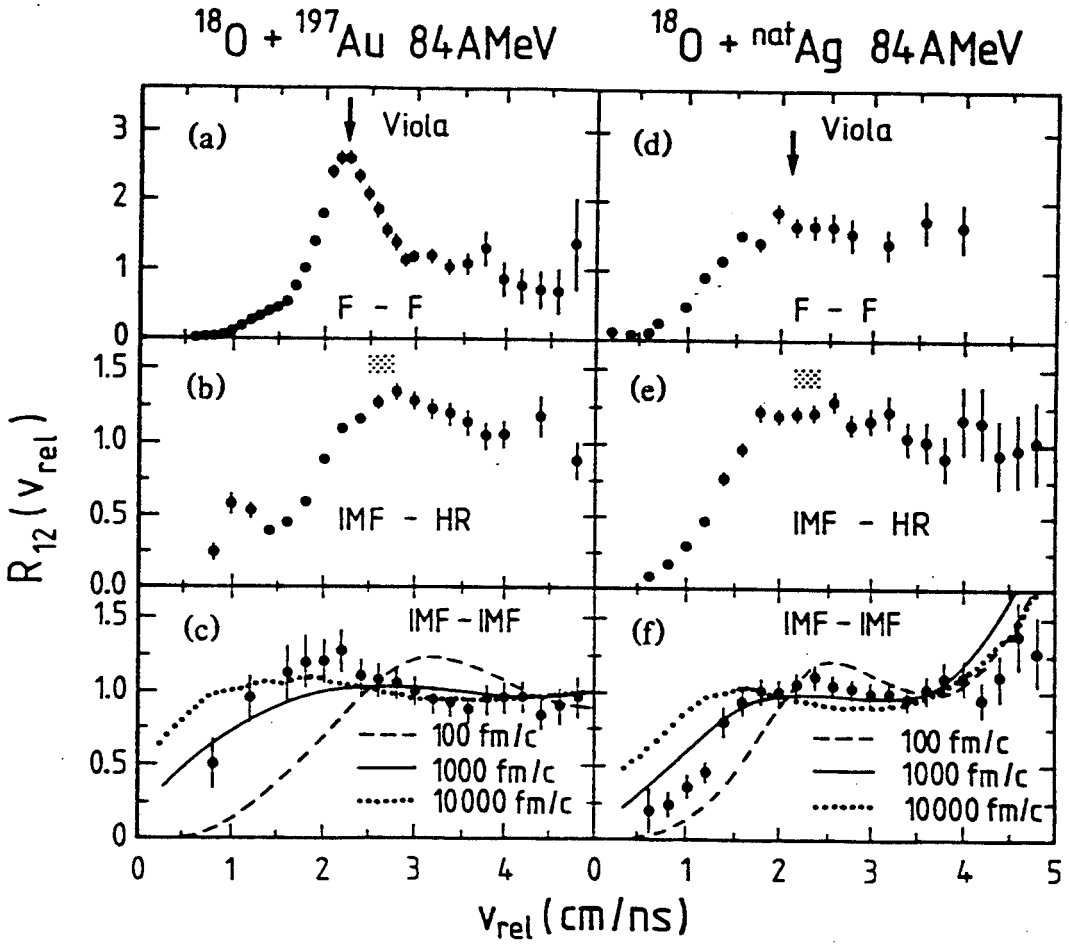

Figure 1.4 Two-fragment correlation functions measured with reactions on Au(left) and Ag(right) [from Tro87].

the detailed technical aspects of the MSU Miniball. The first experiment with the MSU Miniball was a study of the reaction of $^{36}Ar + ^{197}Au$ at E/A = 35MeV. In Chapter 4, we describe the experimental setup and the methods of data reduction. In Chapter 5 we present experimental results; elemental and angular fragment distributions, total and IMF multiplicity, distributions, and charge correlation functions.

To obtain informations about the time scale of IMF emission we employed the technique of intensity interferometry. In Chapter 6 we present a simple theoretical expression for the two-fragment correlation functions and investigate the validity of the approximations used in the calculations. In Chapter 7 our experimental two-fragment correlation functions are compared to calculations and the time scales are extracted. Summary and conclusions are provided in Chapter 8.

Chapter 2 Observation of Multi-fragment Emission with Dwarf Ball.

To study multi-fragment emission processes in intermediate energy heavy-ion collisions we performed an exploratory experiment with a newly developed 4π detector from Washington University [Sar88,Str90]. Two additional PPACs were constructed for this experiment by our group. To clarify the relative importance of single and multi-fragment emission mechanisms, we have measured the IMF multiplicity distributions for fragments emitted beyond the grazing angle for the reactions $^{36}Ar + ^{238}U$ at E/A = 20 and 35 MeV and $^{14}N + ^{238}U$ at E/A = 50MeV. To discriminate between fusion-like central and less violent peripheral collisions, the IMF multiplicity distributions were measured in coincidence with two fission fragments and light charged particles from the decay of the associated heavy reaction residues.

2.1 Experimental setup

In the experiment, a $^{238}UF_4$ target of 400 $\mu g/cm^2$ areal density was bombarded by ^{14}N and ^{36}Ar beam of three different energies from the K500 cyclotron at Michigan State University. Charged particles were detected with 96 phoswich detectors of the "Dwarf Ball/Wall" array developed at Washington University[Sar88,Str90]. A schematic diagram of the experimental setup is shown in Figure 2.1. The geometrical front view of the Wall and ball detectors is shown at the bottom part of the figure. Each phoswich detector consisted of a thin fast plastic scintillator foil followed by a thick CsI(Tl) scintillator, with 200 μm plastic

Dwarf Ball/Wall + PPAC

Experimental Setup

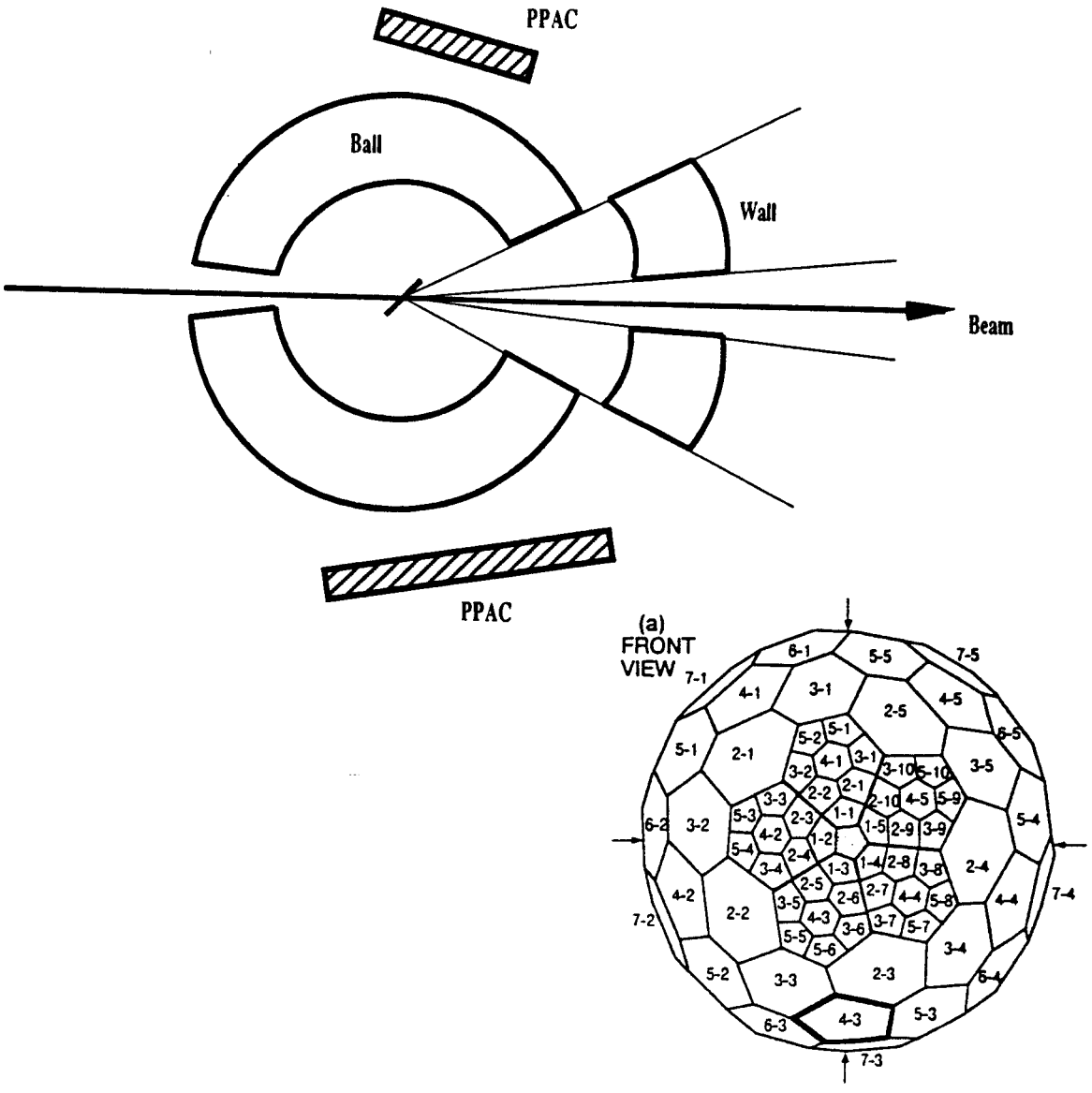

Figure 2.1 Schematic of experimental set-up using Dwarf Ball/Wall and two PPACs; bottom part is the geometrical front view of Dwarf Ball/Wall system consisting of hexagons and pentagons.

scintillation foils and 20 mm CsI(Tl) scintillators at the forward angles, reducing to 40 μm foils and 4 mm CsI(Tl) scintillators at the backward angles. To suppress secondary electrons and X-rays, the Dwarf Ball detectors (located at $\Theta \gtrsim 35°$) and Dwarf Wall detectors (located at $12° \lesssim \Theta \lesssim 35°$) were covered by 5 mg/cm^2 thick Au foils and 10 mg/cm^2 thick Ta foils, respectively. The most forward detectors at $\Theta \lesssim 12°$, covering the grazing angle, were shielded by 1 g/cm^2 Pb absorbers to stop elastically scattered projectile nuclei. These absorbers also stopped IMF's, but allowed the detection of energetic light particles. For light particles, the detection array provided an angular coverage corresponding to about 85% of 4π. For heavy fragments, the coverage was reduced to about 78% of 4π; about 1% of the loss in coverage is due to the Pb absorbers with additional losses due to poor elemental resolution for detectors located at $\Theta \gtrsim 150°$.

Particle identification was achieved by integrating the photomultiplier anode current over three different time gates (See Section 3.3). This information was combined to obtain the energy of the detected particle as well as elemental identification up to about $Z \approx 6$ and isotopic identification for light particles ($Z \leq 2$) stopped in the CsI(Tl) scintillators. Fission fragments were detected with two X-Y-position sensitive parallel plate multiwire detectors [Bre84] covering angular ranges of $\Theta_1 = 36°\text{-}116°$, and $\Theta_2 = -(39°\text{-}89°)$ in the reaction plane. In the off-line analysis, the energy thresholds for the Dwarf Ball detectors were set to 12 and 18 MeV for hydrogen and helium nuclei, respectively; for the Dwarf Wall detectors they were set to 20 MeV for both hydrogen and helium. All heavier particles which passed through the absorber and scintillator foils were analyzed, corresponding to thresholds of $E/A \approx 6\text{-}9$ MeV and $E/A \approx 2\text{-}3$ MeV for the Dwarf Wall and Dwarf Ball detectors, respectively. Unfortunately, double-hits by two α-particles caused significant contaminations in the Z=3 particle identification gate. Therefore, IMF multiplicity distributions for fragments with $Z \geq 4$ have been

constructed. Contributions from random events were negligible for all observables discussed in this thesis.

2.2 Reaction filter: Impact parameter selection

Inclusive experiments determine only impact-parameter averaged quantities, while the detailed reaction mechanism largely depend on the impact parameter. The resulting loss of information can lead to ambiguous interpretations, which could be overcome by employing suitable reaction filters capable of selecting specific classes of collisions. Such filters are particularly useful if they can be used to select well defined narrow ranges of impact parameters.

A number of different techniques have been explored. The folding angle, $\Theta_{ff} = \Theta_{f1} + \Theta_{f2}$, between coincident fission fragments provides information about the linear momentum transfer to fissionable heavy reaction residues [Fat85,Che87]. (Θ_{f1} and Θ_{f2} are the polar angles of the two fission fragments with respect to the beam axis.) Folding angle measurements can discriminate between peripheral, quasi-elastic collisions and central, fusion-like reactions. An alternative technique employs neutron multiplicity measurements [Gal85]. For the ^{20}Ne+U reaction at E/A=14.5 MeV, the measured neutron multiplicity was found to exhibit a monotonic and nearly linear dependence on folding angle, indicating a close relation between these two kinds of reaction filters, at least at low incident energies.

Existing 4π neutron detectors are mostly sensitive to low-energy neutrons emitted in the statistical decay of fully equilibrated reaction products. Hence, the measured neutron multiplicity is closely related to the amount of energy deposited into equilibrated degrees of freedom. Since energies and angles of the

emitted neutrons are not measured, other details of the reaction remain undetermined, e.g. the orientation of the reaction plane or the transverse momentum of the emitted particles [Dan85]. Charged particle detector arrays can overcome such limitations and provide information about the multiplicities of energetic emissions for which 4π neutron detectors become inefficient.

For low incident energies, the multiplicity of charged particles emitted statistically to backward angles will largely reflect the excitation energies of the nearly equilibrated reaction residues. The multiplicities of charged particles emitted to forward angles, on the other hand, are dominated by nonequilibrium processes. With increasing energy, the multiplicities of these nonequilibrium emissions should reflect to an increasing degree the impact parameter dependent geometry or "participant volume" characteristic of the early stages of the collision [Wes76]. At intermediate energies, both equilibrium and nonequilibrium emissions are present. The sensitivity of any charged particle array to either process may depend strongly upon the angular range subtended by the device. Therefore we have performed a cross calibration of charged particle multiplicity filters for intermediate energy collisions, through an experimental investigation of the relationship between charged particle multiplicities and fission fragment folding angles for the reactions $^{36}Ar + ^{238}U$ at $E/A = 35$ MeV and $^{14}N + ^{238}U$ at $E/A = 50$ MeV.

Figure 2.2 shows two-dimensional contour diagrams of folding angle, Θ_{ff}, versus measured charged particle multiplicities. (These raw multiplicities are not corrected for efficiency losses due to detection thresholds and incomplete solid angle coverage; therefore, they are slightly smaller than the true charged particle multiplicities.) The left and right hand panels show data for the $^{14}N+^{238}U$ and $^{36}Ar+^{238}U$ reactions, respectively. For orientation, the upper scales give the linear momentum transfer, $\Delta P/P$, to the heavy reaction residue in units of the projectile

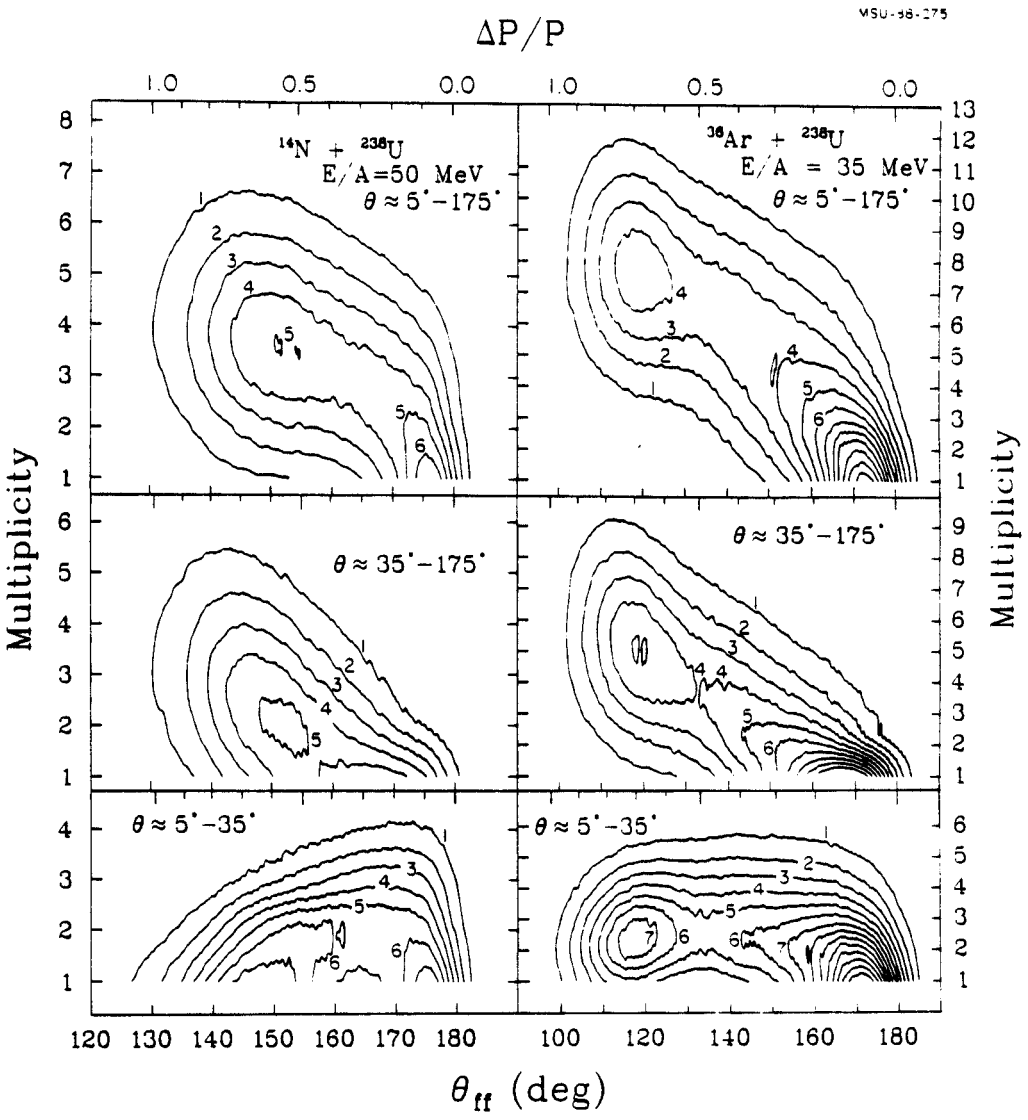

Figure 2.2 Measured correlation between charged particle multiplicity and folding angle for the $^{14}N+^{238}U$ reaction at E/A=50 MeV (left hand side) and for the $^{36}Ar+^{238}U$ reaction at E/A=35 MeV (right hand side). The angular range over which the charged particles are detected is indicated for each panel. The numbers of events (divided by a factor 1,000) for individual contours are given in the figure.

momentum, P, assuming symmetric fission of the compound nucleus. The upper panels show the total multiplicities, M, measured with the entire array (covering the angular range of $\Theta \approx 5°$-$170°$). The center panels show the number of particles detected with the "Dwarf Ball" (covering the angular range of $\Theta \approx 35°$-$170°$) and the lower panels show the number of particles detected with the "Dwarf Wall" (covering the angular range of $\Theta \approx 5°$-$35°$).

For both reactions, the average multiplicity of charged particles emitted over the entire angular range ($\Theta \approx 5°$-$170°$) increases monotonically with increasing linear momentum transfer to the heavy reaction residue. This dependence is qualitatively similar to the monotonic relation between neutron multiplicity and folding angle which has been established for reactions at lower incident energies [Gal85,Mor88]. For the $^{36}Ar+^{238}U$ reaction, the dependence of the average multiplicity on folding angle is similar to the results obtained for a similar reaction at a slightly lower energy [Jacq85]. A nearly linear correlation between multiplicity and linear momentum transfer is observed for charged particles emitted at intermediate and large angles ($\Theta \approx 35°$-$170°$). In contrast, the multiplicity of charged particles emitted at forward angles ($\Theta \approx 5°$-$35°$) is nearly independent of the linear momentum transfer to the heavy reaction residue [Jacq85]. At least for the present reactions, the multiplicities detected in forward arrays [Biz86] cannot be used to select violent projectile-target interactions in which large amounts of energy and/or momentum are dissipated.

Charged particle multiplicity as well as folding angle measurements represent reaction filters of finite resolution. Even for the ideal case of formation and decay of a composite nuclear system with unique spin, excitation energy, and recoil momentum, multiplicity and folding angle distributions have finite widths. The widths of folding angle distributions reflect the finite widths of the mass and kinetic energy distributions of the fission fragments as well as

smearing from light particle evaporation. For more energetic collisions, additional broadening can be caused by the emission of intermediate mass fragments [Fat87]. The widths of charged particle multiplicity distributions reflect the stochastic nature of neutron and charged particle emission mechanisms. Particularly at lower energies, where the charged particle multiplicities are small, statistical fluctuations in the multiplicities can be comparable to the mean values and the selectivity of charged particle multiplicities as reaction filters can be reduced.

The widths of various gated distributions are shown in Figure 2.3. The upper and lower sections show data for the $^{14}N+^{238}U$ and the $^{36}Ar+^{238}U$ reactions, respectively. The left hand panels show distributions for total charged particle multiplicity gated by folding angle intervals, 1° wide and centered at the indicated angles. The right hand panels show folding angle distributions measured for different total charged particle multiplicities, M = 1, 3, 6 for the $^{14}N + ^{238}U$ reaction and M = 1, 6, 12 for the $^{36}Ar + ^{238}U$ reaction. The high multiplicity gates (M=6 for $^{14}N + ^{238}U$ and M=12 for $^{36}Ar + ^{238}U$) represent cuts in the tails of the charged particle multiplicity distributions, at values approximately 50% larger than the most probable multiplicity observed for fusion-like collisions (see left hand panels, or Figure 2.2).

Charged particle multiplicity distributions gated by large folding angles, $\Theta_{ff} \approx 175°$, are clearly peaked at M≤1. However, they exhibit remarkably long tails extending to high multiplicities. Multiplicity distributions gated by small folding angles (or fusion-like collisions) are peaked at M≈4 and 8 for the $^{14}N+^{238}U$ and $^{36}Ar+^{238}U$ reactions, respectively. They are rather broad indicating significant fluctuations of the number of emitted charged particles. There is considerable overlap between the multiplicity distributions gated by very different folding angles.

MSU-88-274

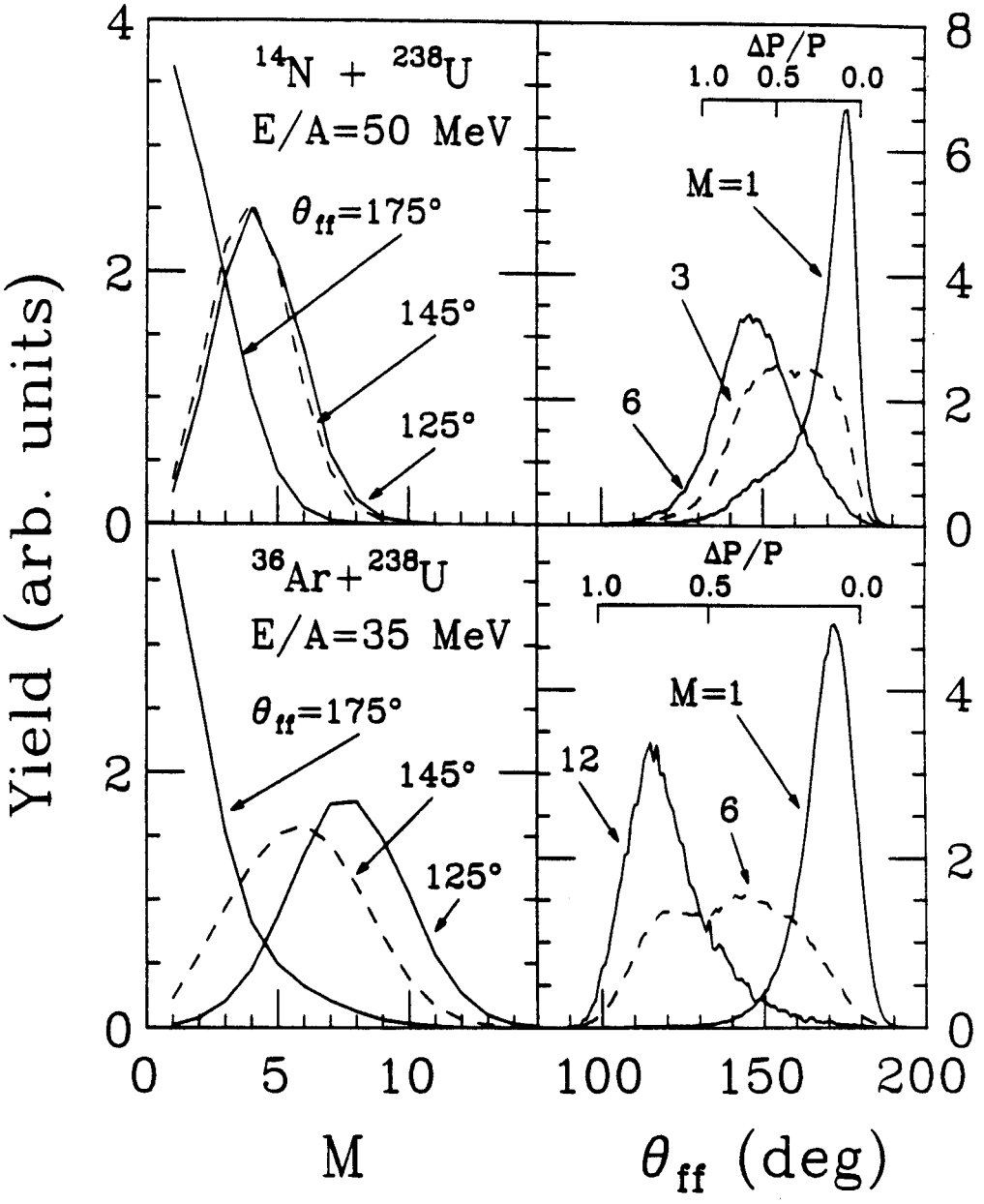

Figure 2.3 Gated multiplicity (left hand panels) and folding angle (right hand panels) distributions measured for the reactions ^{14}N+^{238}U at E/A=50 MeV (upper part) and ^{36}Ar+^{238}U at E/A=35 MeV (lower part). The distributions for each panel are normalized to the same integrated yield. The gates on folding angle, Θ_{ff}, are 1° wide; their centers are indicated in the left hand panels. The gates on multiplicity, M, are indicated in the right hand panels.

Folding angle distributions gated by low (high) charged particle multiplicities are peaked at large (small) folding angles, respectively. The widths of these distributions are very similar to the widths measured for the out-of-plane distributions of fission fragments selected by the same multiplicity gates, indicating that these gates do not introduce significant broadening beyond the intrinsic resolution of the folding angle technique. In contrast, folding angle distributions gated by intermediate charged particle multiplicities (M=3 for $^{14}N+^{238}U$ and M=6 for $^{36}Ar+^{238}U$) are significantly broader indicating that such multiplicity gates are less selective.

2.3 Multi-fragment emission

The solid line in Figure 2.4 shows the inclusive folding angle distribution for fission-fission coincidences. The dashed and dotted-dashed curves show folding angle distributions gated by the detection of at least one and three intermediate mass fragments at backward angles ($\theta \gtrsim 35°$) in the Dwarf Ball, $N_{IMF}^{(b)} \geq 1$ and 3, respectively. Distributions gated by $N_{IMF}^{(\tilde{b})} \geq 1$ and 3 are remarkably similar indicating that single and multi-fragment emissions to intermediate and large angles can be associated with violent, fusion-like collisions characterized by large linear momentum transfers [Fat85]. The light and heavy dotted curves show distributions gated by the detection of at least one and three intermediate mass fragments at forward angles ($\theta \lesssim 35°$) in the Dwarf Wall, $N_{IMF}^{(w)} \geq 1$ and 3, respectively. The condition $N_{IMF}^{(w)} \geq 1$ does not select a very specific class of collisions, with contributions from both incomplete fusion reactions and peripheral collisions. The requirement $N_{IMF}^{(w)} \geq 3$, On the other hand, clearly selects more peripheral collisions with smaller linear momentum transfers to the heavy reaction residue.

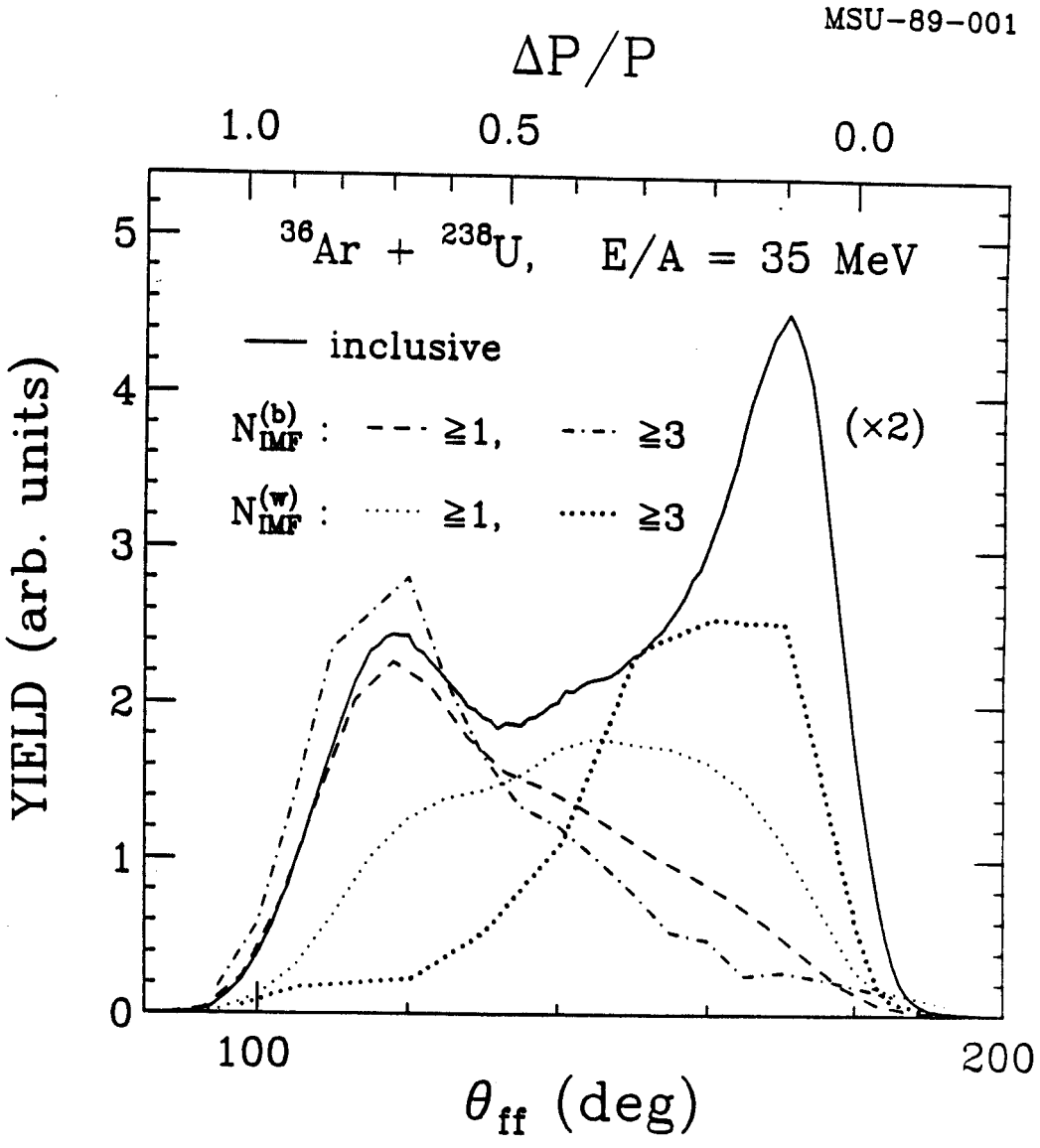

Figure 2.4 Folding angle distributions between coincident fission fragments. The upper scale gives the linear momentum transfer, ΔP/P, in units of the projectile momentum to the heavy reaction residue assuming symmetric fission. The various gating conditions are explained in the text. For comparison, the distributions are normalized to give the same integrated yields, with the inclusive distribution multiplied by an additional factor of 2.0. The measured yields of the inclusive, $N_{IMF}^{(b)}=1$, $N_{IMF}^{(b)}=3$, $N_{IMF}^{(w)}=1$, and $N_{IMF}^{(w)}=3$ spectra are 2.2×10^{6}, 3.1×10^{5}, 2.6×10^{3}, 3.8×10^{5}, 2.1×10^{3} counts, respectively.

Figure 2.5 shows associated charged-particle multiplicities, $N_C = N_{tot} - N_{IMF}^{(gate)}$, where N_{tot} is the total observed charged particle multiplicity (excluding fission fragments) and $N_{IMF}^{(gate)}$ denotes the number of fragments in the gate. The curves are defined as in Figure 2.4: the solid line shows the inclusive distribution for fission-fission coincidences; the dashed and dotted-dashed light and heavy dotted) curves show distributions gated by $N_{IMF}^{(b)} \geq 1$ and 3 ($N_{IMF}^{(w)} \geq 1$ and 3), respectively. Consistent with this finding, the observed associated charged particle multiplicities are large for IMF's emitted at $\Theta \gtrsim 35°$ and rather similar for the $N_{IMF}^{(b)} \geq 1$ and 3 gates. The requirement $N_{IMF}^{(w)} \geq 3$ leads to lower mean associated charged particle multiplicities consistent with a bias towards more peripheral collisions. The different gates discussed in Figs. 2.4 and 2.5 clearly select different classes of collisions reflecting impact parameter ambiguities which obscure the interpretation of inclusive data. These ambiguities can be removed by suitable choices of reaction filters.

Figure 2.6 shows probabilities for observed multiplicities, N_{IMF}, of intermediate mass fragments for different gates on folding angle. Open circles correspond to the inclusive distributions for fission-fission coincidences; open squares correspond to small momentum transfer collisions gated by $\Theta_{ff} > 160°$ ($\Delta P/P<0.2$); solid points correspond to large momentum transfer collisions gated by $\Theta_{ff} \leq 133°$ ($\Delta P/P \geq 0.5$). Both single and multifragment emission occur with significantly higher probabilities in central collisions characterized by large linear momentum transfers. However, since all events in this experiment required coincident fission fragments in the exit channel, we cannot exclude the possibility that even higher multiplicities might occur in collisions which do not lead to fission. Even though most IMF's are produced in events with $N_{IMF}=1$ [Bor88], unit IMF multiplicity does not appear uniquely significant. Instead, the multiplicity distributions decrease monotonically from $N_{IMF}=0$ and are rather well described

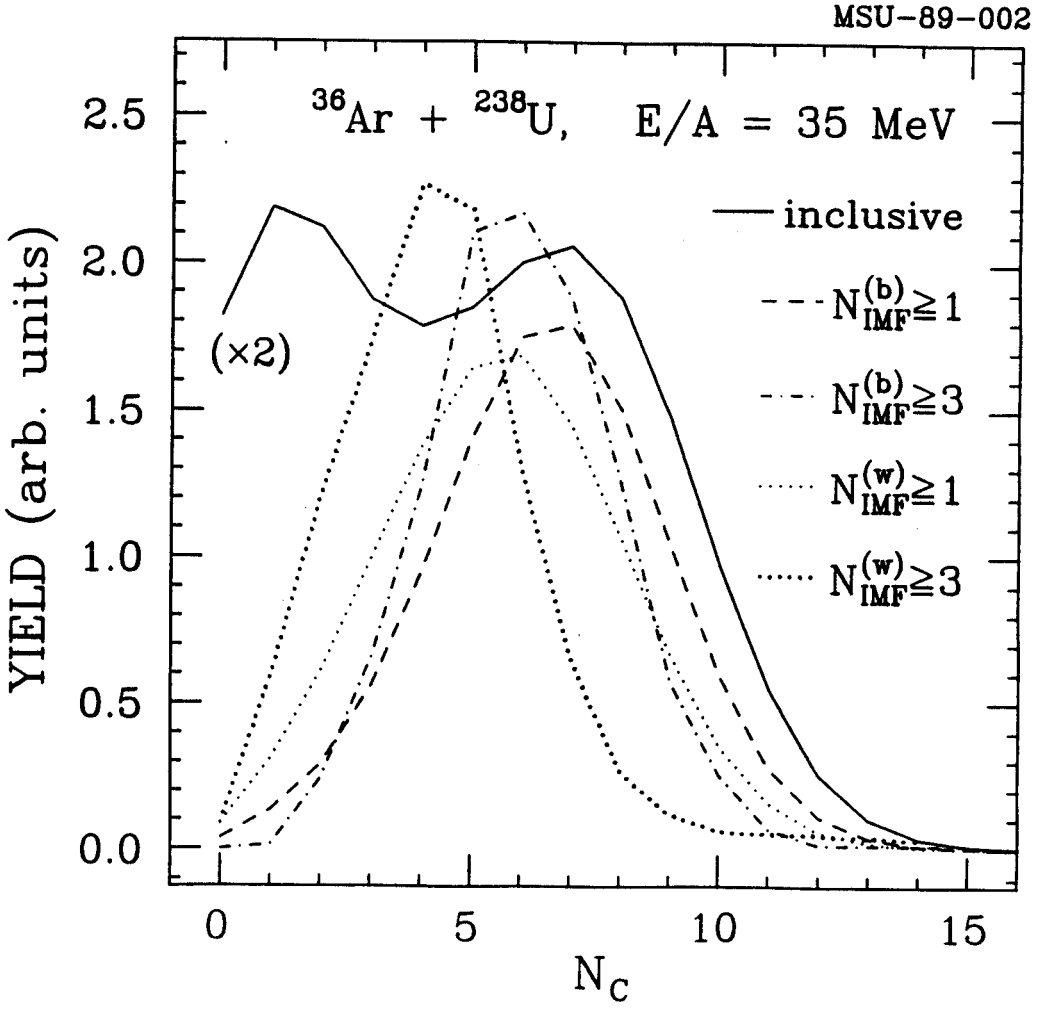

Figure 2.5 Associated charged-particle multiplicities, N_C. The various gating conditions are explained in the text. For comparison, the distributions are normalized to give the same integrated yields, with the inclusive distribution multiplied by an additional factor of 2.0.

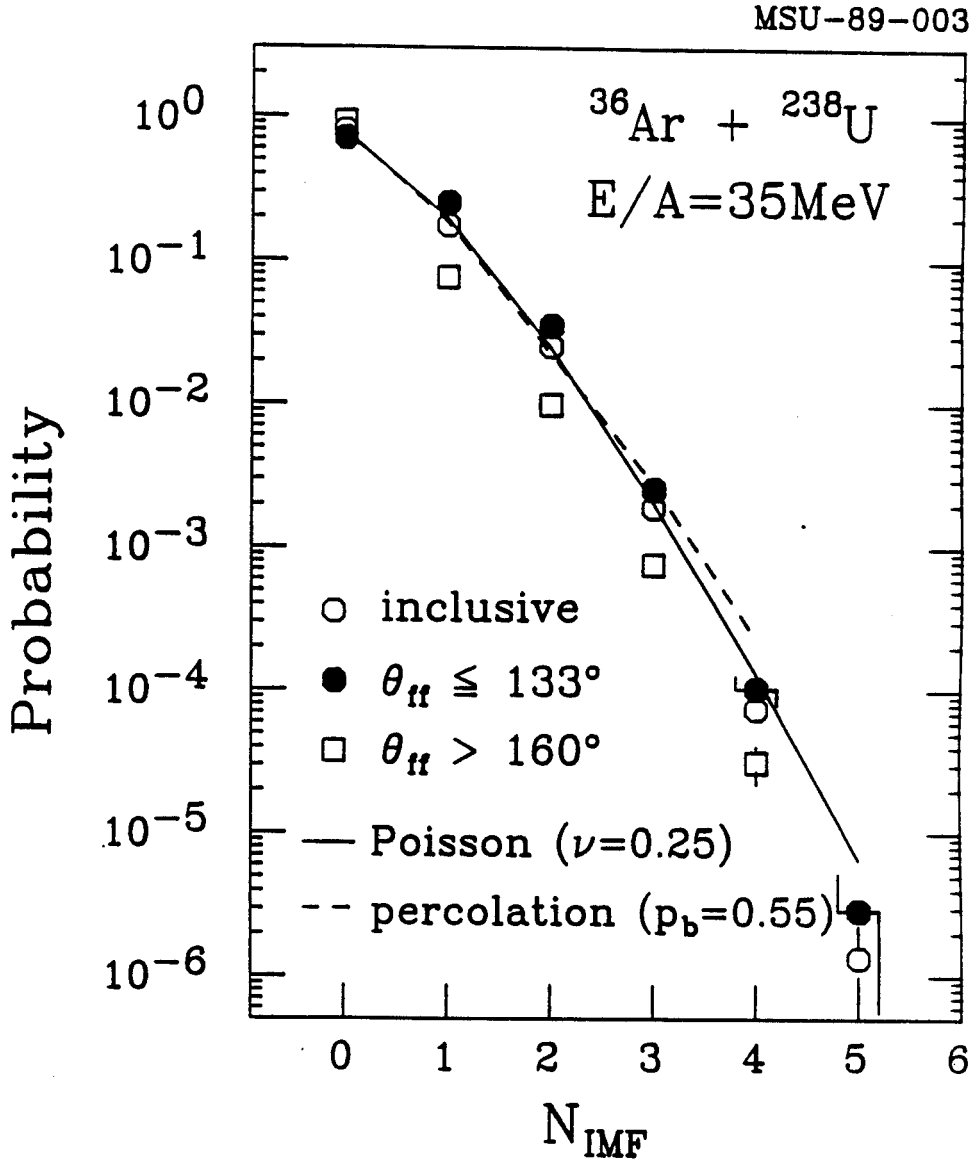

Figure 2.6 Probabilities per fission trigger for the detection of single and multiple fragments with Z ≥ 4. Open circles: no gate on Θ_{ff}; open squares: Θ_{ff}>160°; solid points: Θ_{ff}≤133°. Solid curve: Poisson distribution, $P(N,\nu) = e^{-\nu}\nu^N/N!$, with ν=0.25; dashed curve: prediction of the percolation model [Bau86] for p_b=0.55.

by Poisson probability distributions (an example is shown by the solid curve).

Poisson distributions are characteristic of processes which occur with a low and constant probability. Such conditions may prevail for nuclear decays at high excitation energies and with low fragment multiplicities. For example, the statistical weight for fragment emission is small as compared to that for light particle emission when calculated in a statistical rate equation approach such as a sequential evaporation model [Mor75,Fri83]. In this case, deviations from Poisson distributions would be expected to occur mainly for high fragment multiplicities or small systems when emission probabilities are affected by energy or mass conservation. To illustrate that Poisson distributions may also be expected in a static theory which encompasses a phase transition we show in Figure 2.6 a distribution predicted by the percolation model [Bau86]. While the IMF detection efficiency of the present experiment is sufficient to reveal the qualitative trends of the multiplicity distributions, the IMF yields below the detection thresholds of the present apparatus would be required to determine the exact shape of the multiplicity distributions and hence, definitive values for the percolation parameter, p_b, or the average ν of the Poisson distribution. A model independent correction of the IMF detection efficiency is beyond the scope of the present measurement.

To see the dependence of IMF production probability on the system and incident energy Figure 2.7 shows the IMF multiplicity distribution for all three reactions preformed in this experiment with central gate, $\Delta P/P>0.5.$, on the folding angle. For all three cases the data can be described by the Poisson distributions shown by the curves in the figure.

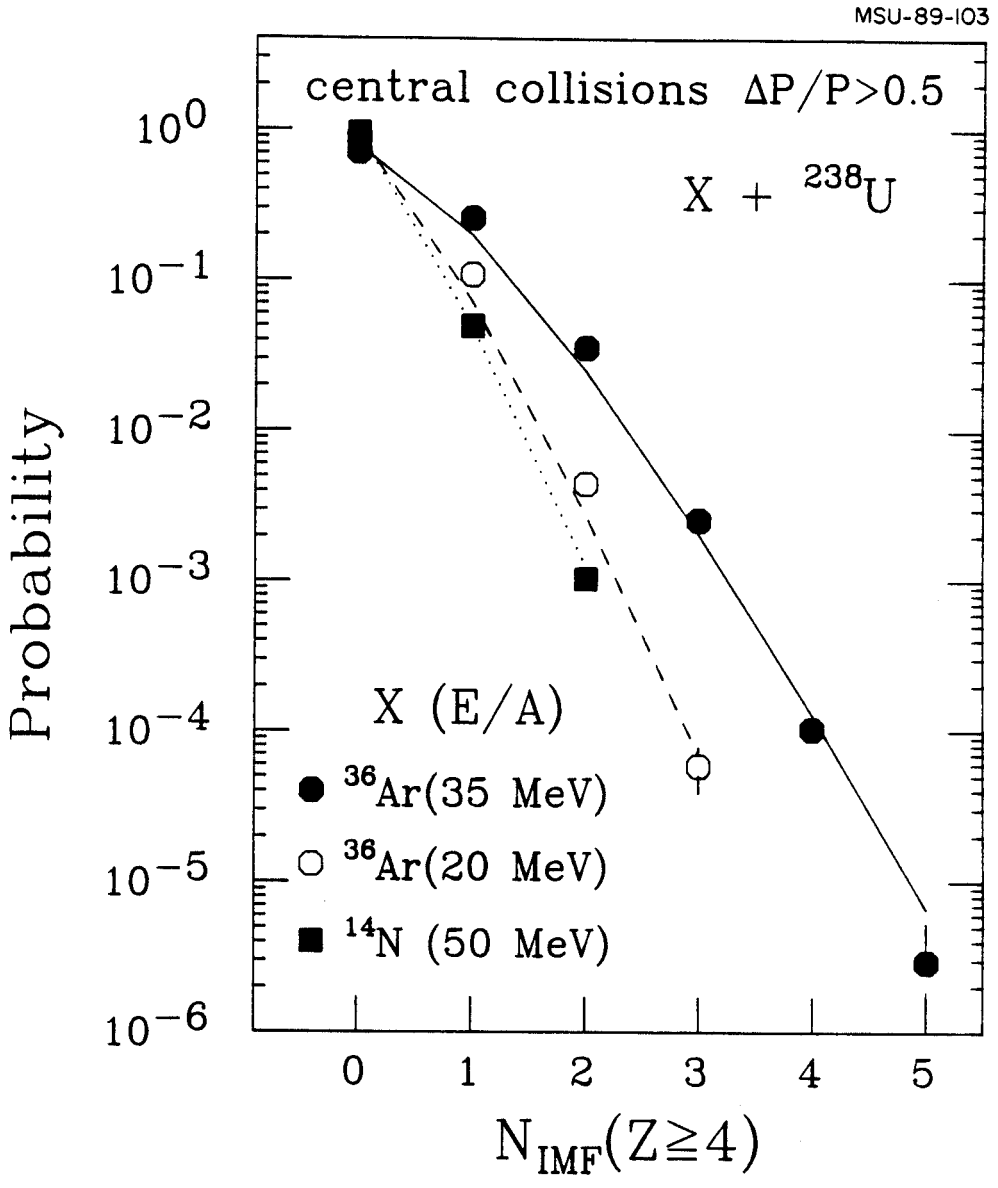

Figure 2.7 Probabilities per fission trigger for the detection of N_{IMF} fragments with Z≥4 gated on central collision(ΔP/P>0.5). Curves are Poisson distributions.

2.4 Summary

This experiment was the first 4π experiment at NSCL which was performed with nearly 4π solid angle coverage. The detector, "Dwarf Ball/Wall", was a pioneering device for intermediate energy heavy-ion nuclear collision experiments. It has a larger phase space coverage and dynamic range than that which characterized the previous devices used to study multi-fragment emission at intermediate energies [Bou87]. Nevertheless, this device also display some limitations such as a poor resolution in particle identification specially for IMFs, a non-polar geometry, a relatively small dynamic range($1 \leq Z \leq 10$), and a low granularity. Moreover, energy calibrations for the response of the Dwarf Ball/Wall were not performed for this first experiment, which seriously limited the directions of the data analysis. Therefore our group decided to build a new 4π detector which could overcome some of these limitations. This new 4π detector, the MSU Miniball, was completed in the spring of 1990 after 2 years of design work, test runs, and the mass- production of the detectors. The next chapter describes the technical details of this device.

Chapter 3 MSU Miniball - 4π fragment detection array

In order to study multi-fragment disintegrations of hot nuclear systems with nearly 4π coverage, we have constructed a fragment detection array of high granularity and low detection thresholds. The design criteria we considered were as follows :

(1) High granularity to handle large multiplicity events.

(2) Good particle identification for Z = 1-20.

(3) Low energy threshold.

(4) Large solid angle coverage.

(5) Mass identification for light charged particles (H+He).

(6) Good energy resolution.

(7) Modular design; compact and portable.

(8) Polar coordinate geometry.

In its original configuration, the device covers the angular range of $\theta_{lab} = 9^{\circ}$-160° with 188 phoswich detectors consisting of 40 μm thick plastic scintillator foils and 2 cm thick CsI(Tl) scintillators. Thresholds for particle identification range from E/A≈1.5 MeV for alpha particles to E/A≈3 MeV for Ca ions. Individual detectors can resolve elements from Z≈1-18, as well as isotopes of hydrogen and helium. Fission fragments can also be identified. Charged particle detector arrays based on similar techniques have also been built by two other groups [Sar88,Dra89].

3.1 Mechanical Construction of the Array

The Miniball phoswich detector array is designed to operate in vacuum. Figure 3.1 shows an artist's perspective of the three-dimensional geometrical assembly of the Miniball sitting on the turntable of the 92" scattering chamber. The array consists of 11 independent rings coaxial about the beam axis. For ease of assembly and servicing, the individual rings are mounted on separate base plates which slide on two precision rails. The rings and detector mounts are made of aluminum. Good thermal conductivity between detectors and the mounting structure allows the conduction of heat generated by the photomultiplier voltage divider network into the array superstructure. This heat is removed from the Miniball by cooling the base plates to the desired temperature by circulating ethanol through a copper pipe attached to the base plates. By this means, constant operating temperature in vacuum is achieved after a brief equilibration time. The individual detector mounts are designed to allow the removal of any detector without interfering with the alignment of neighboring detectors. The entire assembly is placed on an adjustable mounting structure which allows for the alignment of the apparatus with respect to the beam axis.

Figure 3.2 shows a half-plane section of the array in the vertical plane which contains the beam axis. Individual rings are labelled by the ring numbers 1-11 which increase from forward to backward angles. For each ring, the number of detectors is given in parentheses. For a given ring, the detectors are identical in shape and have the same polar angle coordinates with respect to the beam axis; these angles are indicated in Figure 3.2. In Table 3.1, we list the solid angles and the ranges of polar and azimuthal angles which are covered by inidvidual detectors of the Miniball. Since the angular distributions of the emitted particles

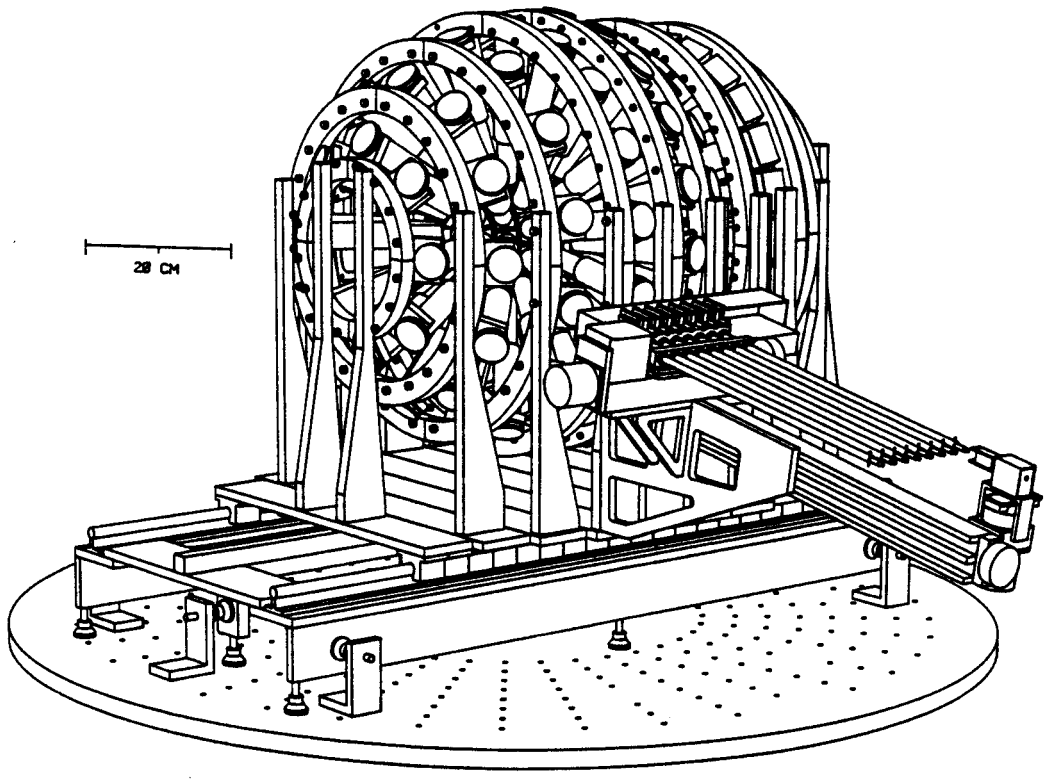

Figure 3.1 Artist's perspective of the assembly structure of the Miniball 4π fragment detection array. For clarity, electrical connections, the light pulsing system, the cooling system, and the target insertion mechanism have been omitted.

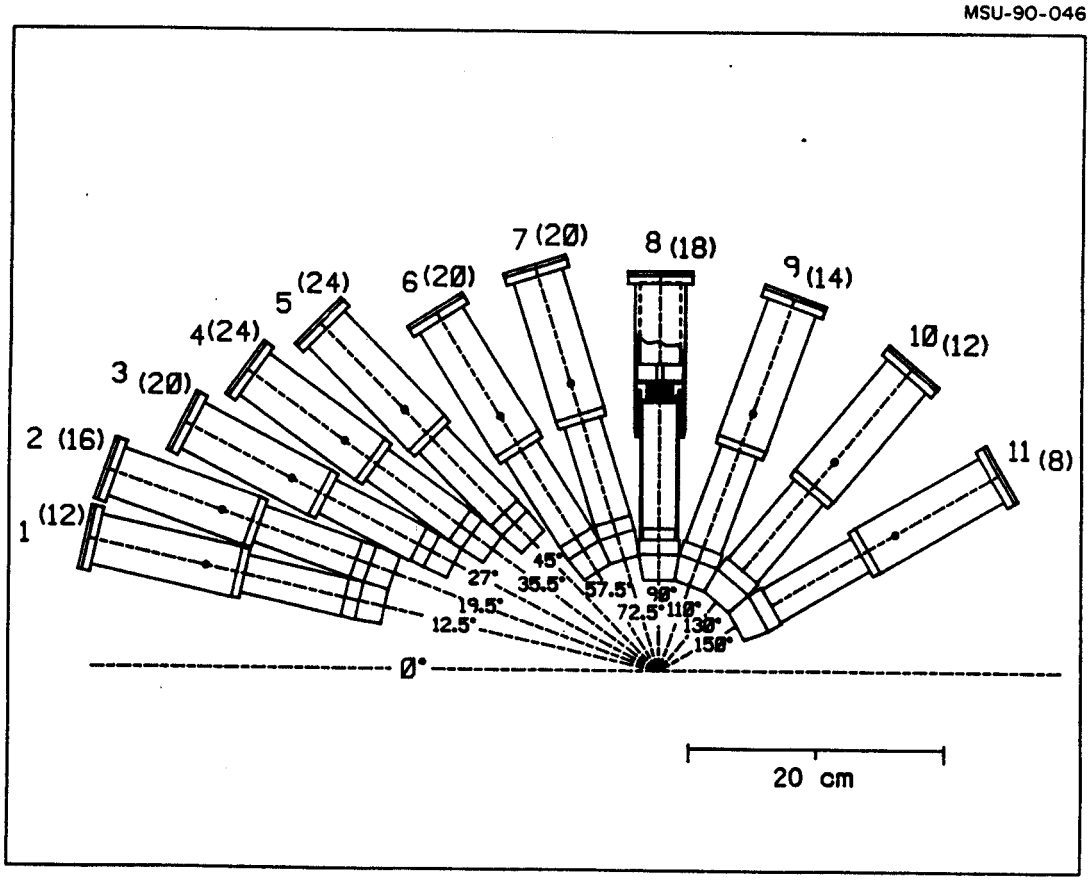

Figure 3.2 Half-plane section of the Miniball array. Individual detector rings are labelled 1 through 11; numbers of detectors per ring are given in parentheses; the polar angles for the centers of the rings are indicated. The dashed horizontal line indicates the beam axis.

Table 3.1 Coverage in solid angle, polar and azimuthal angles for individual detectors of the Miniball. Ring 1 was not used in this experiment.

Ring #	Θ(deg)	ΔΩ(msr)	ΔΘ(deg)	Δφ(deg)
1	12.5	12.3	7	30
2	19.5	14.7	7	22.5
3	27.0	18.5	8	18.0
4	35.5	22.9	9	15.0
5	45.0	30.8	10	15.0
6	57.5	64.8	15	18.0
7	72.5	74.0	15	18.0
8	90.0	113.3	20	20.0
9	110.0	135.1	20	25.7
10	130.0	128.3	20	30.0
11	150.0	125.7	20	45.0

are strongly forward peaked, the solid angle subtended by forward detectors is smaller than for detectors at backward angles. Variations in solid angle were achieved largely by placing detectors at different distances from the target while keeping their size approximately constant. The front face geometries of the individual CsI(Tl) crystals are shown in Figure 3.3. Different detector shapes are labelled by the respective ring numbers with the number of detectors per ring given in parentheses (see Figure 3.2 for the definition of the ring numbers). The crystals are tapered such that front and back surfaces subtend the same solid angle with respect to the target location. In order to save cost of fabrication, the curved surfaces corresponding to constant polar angle were approximated by planar surfaces. The resulting loss in solid angle coverage is on the order of 2%, comparable in magnitude to the loss in solid angle coverage resulting from gaps between individual detectors (which must be provided to allow for mechanical tolerances and optical isolation between neighboring crystals).

An isometric drawing of the target insertion mechanism is shown in Figure 3.4. The targets are mounted on frames made of flat shim stock of 0.2 mm thickness. Each target frame is attached to an insertion rod. The insertion rods are mounted on a tray which can be moved parallel to the beam axis. An electromagnetic clutch provides the coupling to the insertion and retraction drive once a target rod is located at the appropriate position. A third drive allows rotation of an inserted target about the axis of the insertion rod. This rotation of the target plane is useful for the determination of the shadowing a detector experiences when it is located in the plane of the target frame. All the motions of the target system are remotely controlled by a computer program through controllers located outside of the vacuum chamber.

In its present configuration, the detector array covers a solid angle corresponding to about 89% of 4π. The loss in solid angle can be decomposed

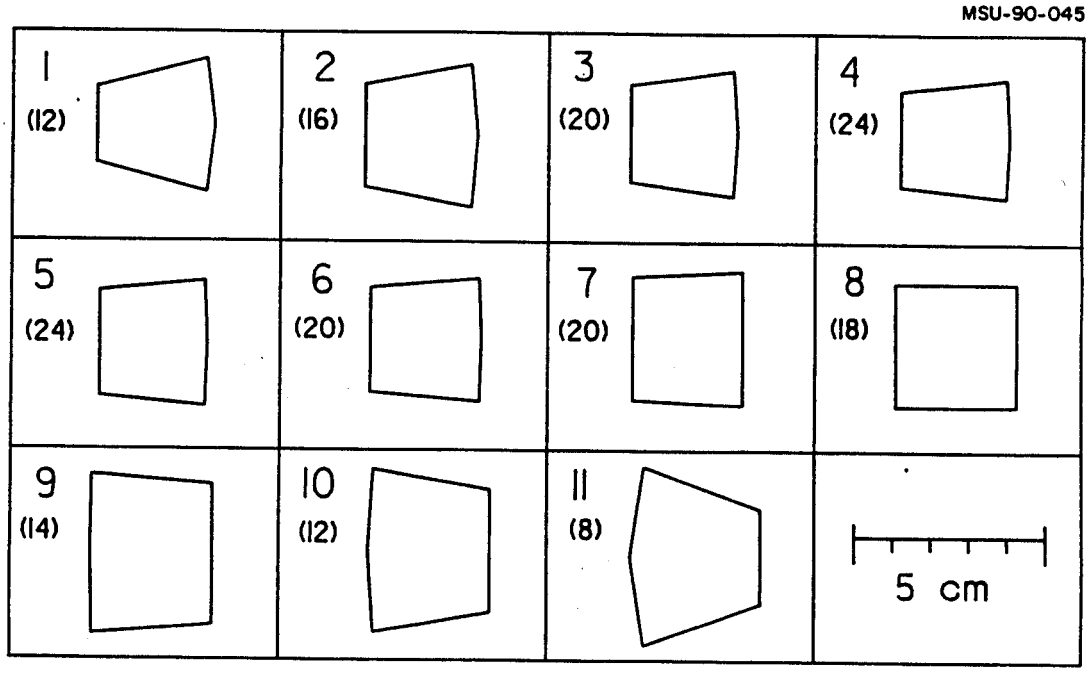

Figure 3.3 Front views of different detector shapes. The detectors are labelled by their ring number; numbers of detectors per ring are given in parentheses.

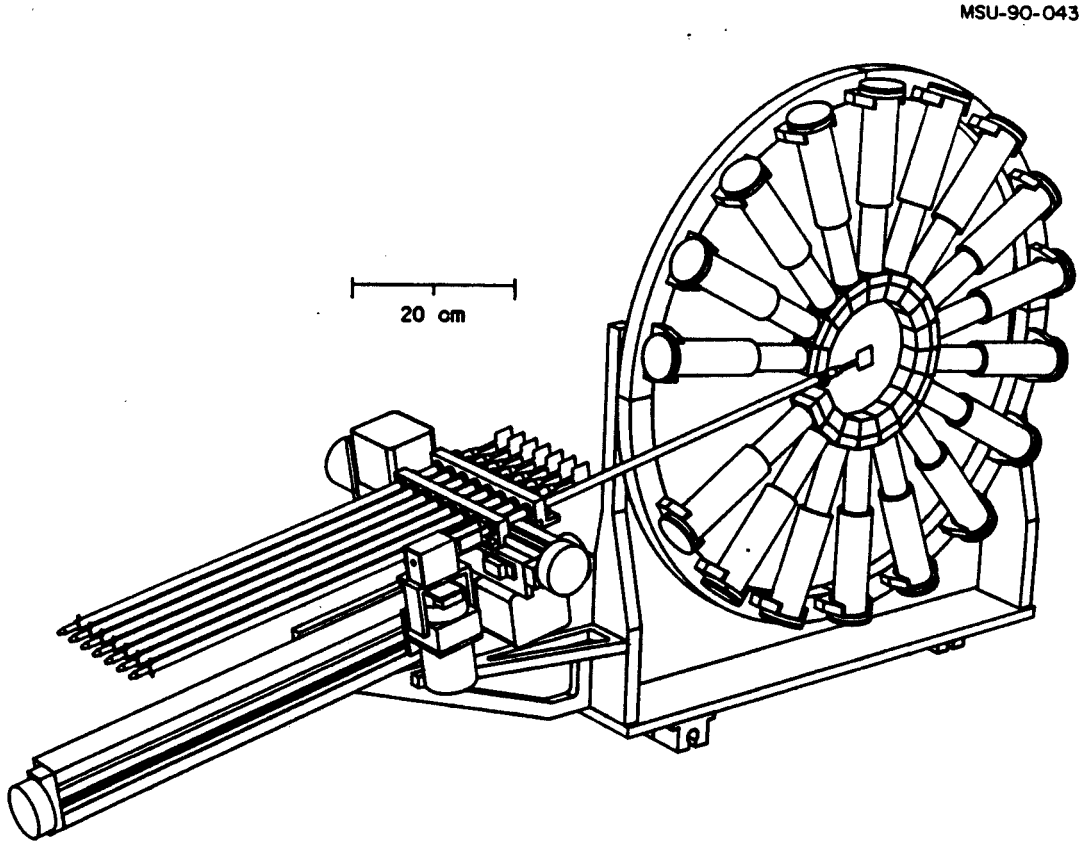

Figure 3.4 Isometric view of the target insertion mechanism.

into the following contributions: (i) beam entrance and exit holes (4% of 4π); (ii) approximation of the curved surfaces corresponding to constant polar angle by planar surfaces (2% of 4π); (iii) optical isolation of detectors and allowance for mechanical tolerances (4% of 4π); (iv) removal of one detector at $\theta=90°$ to provide space for target insertion mechanism (1% of 4π).

3.2 Detector Design

All phoswich detectors of the array are composed of a thin (typical thickness: 4 mg/cm^2 or 40 μm) plastic scintillator foil, spun from Bicron BC-498X scintillator solution, and a 2 cm thick CsI(Tl) scintillator crystal. A schematic of the detector design is given in Figure 3.5. In order to retain flexibility in the choice of scintillator foil thickness, the scintillator foil is placed on the front face of the CsI(Tl) crystal without bonding material. (Tests indicated that a slightly improved resolution could be achieved when the two scintillators are coupled via a thin layer of optical cement, see Section 3.8 below.) The back face of the CsI(Tl) scintillator is glued with optical cement (Bicron BC600) to a flat light guide made of UVT plexiglas. This light guide is 12 mm thick and matches the geometrical shape of the back face of the CsI(Tl) crystal. This light guide is glued to a second cylindrical piece of UVT plexiglass (9.5 mm thick and 25 mm diameter) which, in turn, is glued to the front window of the photomultiplier tube (Burle Industries model C83062E). The photomultiplier tube and the cylindrical light guide are surrounded by a cylindrical μ-metal shield (not shown in the figure). Front and back faces of the CsI(Tl) crystals are polished; the tapered sides are sanded and wrapped with white teflon tape. The front face of the phoswich assembly is covered by an aluminized mylar foil (0.15 mg/cm^2 mylar and 0.02 mg/cm^2 aluminum).

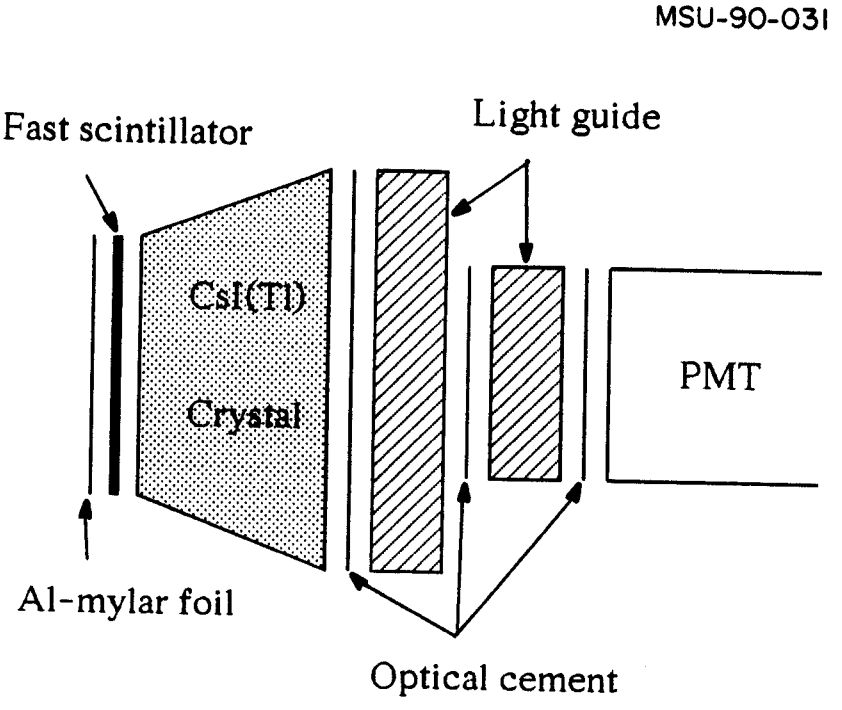

Figure 3.5 Schematic of phoswich assembly of individual detector elements. The μ-metal shield covering the photomultiplier is not included.

The Bicron Beta-paint (BC-498X) used to make fast scintillator foils is a ternary plastic scintillator consisting of a solvent (PVT:Polyvynyle Toluene), a primary solute, and a secondary solute, wave shifter, dissolved into xylene [Kno89,Hur85]. The primary scintillation of the plastic scintillator foil has its maximum intensity at 370 nm. In bulk material of the scintillator, the intensity maximum is shifted to 420 nm by the addition of a wavelength shifter. Our scintillator foils are, however, too thin for an effective wavelength shift and maximum emission remains in the far blue region of the spectrum (the full width at half maximum lies between 350 and 450 nm). The absorption of this light in CsI(Tl) places a constraint on the maximum useful thickness of the CsI(Tl) crystals. For example the transmittancy of visible light at 350nm through 20mm CsI crystal is about 79%, while it is about 85% at 450nm and reaches a maximum transmittancy at about 700nm [Har88]. Additional absorption in the light guides can be minimized by using UVT plexiglas rather than standard plexiglas light guides. The transmittancy of the 24mm thick standard plexiglas is almost 0% at 350 nm and about 50% at 380 nm., which can seriously reduce the blue light of Beta-paint [Bic90]. On the other hand the transmittancy of UVT of the same thickness is about 90% over 350nm. The cathode responsivity of our photomultiplier tube has maximum of 70% at between 350 and 450 nm, which fits the emission spectrum of Beta-paint well. Such considerations become particularly important for phoswich detectors utilizing thin scintillator foils in efforts to reduce particle detection thresholds.

Figure 3.6 shows a photograph of the basic photomultiplier assembly used for all detectors. The phoswich and matching first light guide have not yet been attached in this photograph. A precision- machined aluminum ring is glued to the μ-metal shield surrounding the photomultiplier and the cylindrical light

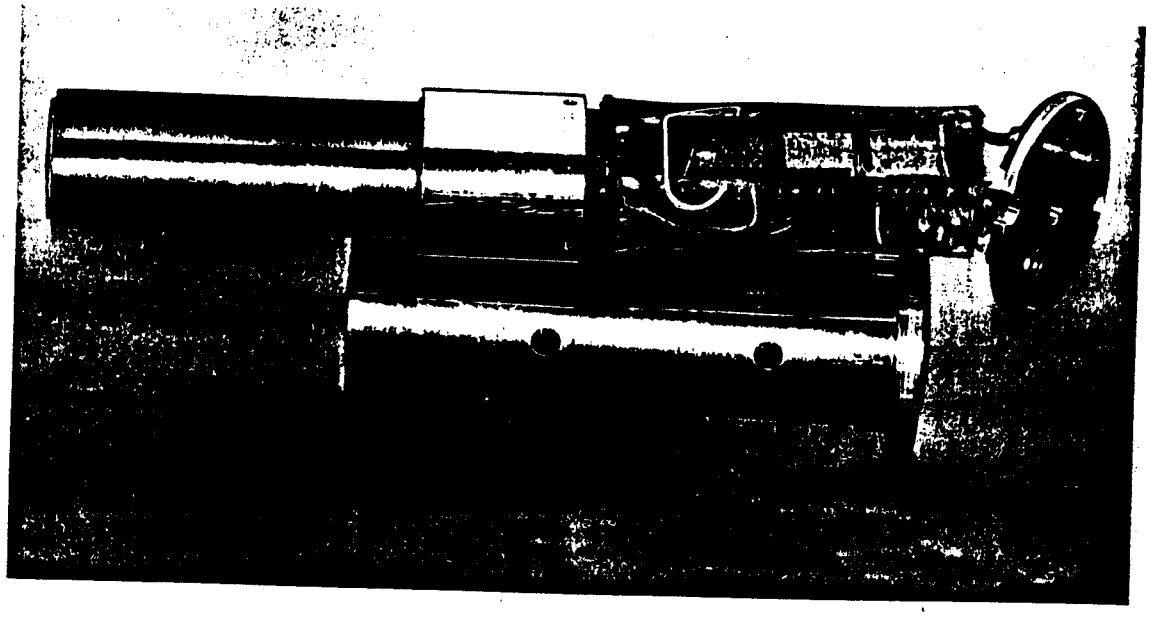

Figure 3.6 Photograph of photomultiplier assembly. The scintillator and the first matching light guide are removed. The ring glued to the μ-metal shield defines the alignment of the can housing the voltage divider. The can has been removed to expose the voltage divider.

guide. This ring provides the alignment for a precision machined aluminum can which houses the voltage divider and which defines the detector alignment when bolted to the rings of the array support structure. In order to expose the voltage divider chain, this aluminum can has been removed and placed next to the photomultiplier. The active voltage divider chain is soldered to the flying leads of the phototube. To prevent destruction of the FETs by sparking during operation in poor vacuum, the entire divider chain, including the leads to the photomultiplier tube, is encapsulated in silicone rubber (Dow Chemical Sylgard 184). Vacuum accidents occurring with fully biased detectors do not lead to divider chain failures. In fact, the detectors are designed to survive a full pumping cycle from atmospheric pressure to vacuum with bias applied to them.

The 10-stage Burle Industries model C83062E photomultiplier tube was chosen because of its good timing characteristics ($\tau_R \approx 2.3$ ns), its large nominal gain ($\approx 10^7$), and its good linearity for fast signals. Since the apparatus is designed to operate in vacuum, active divider chains were chosen to minimize the generation of heat. (The base circuit was designed by M. Maier.) A schematic of the active divider chain is given in Figure 3.7. The final stages of the divider chain are of the "booster" type which provides improved linearity for high peak currents generated by large signals of the fast scintillator.

3.3 Detection Principle

With this highly granular geometry the additional requirements for the Miniball telescope are good particle identification, energy resolution, and low energy threshold. The detection principle of the Miniball telescope is based on the plastic-CsI(Tl) phoswich technique employed for example in the Washington University's Dwarf Wall/Ball. The anode signal from the photomultiplier tube

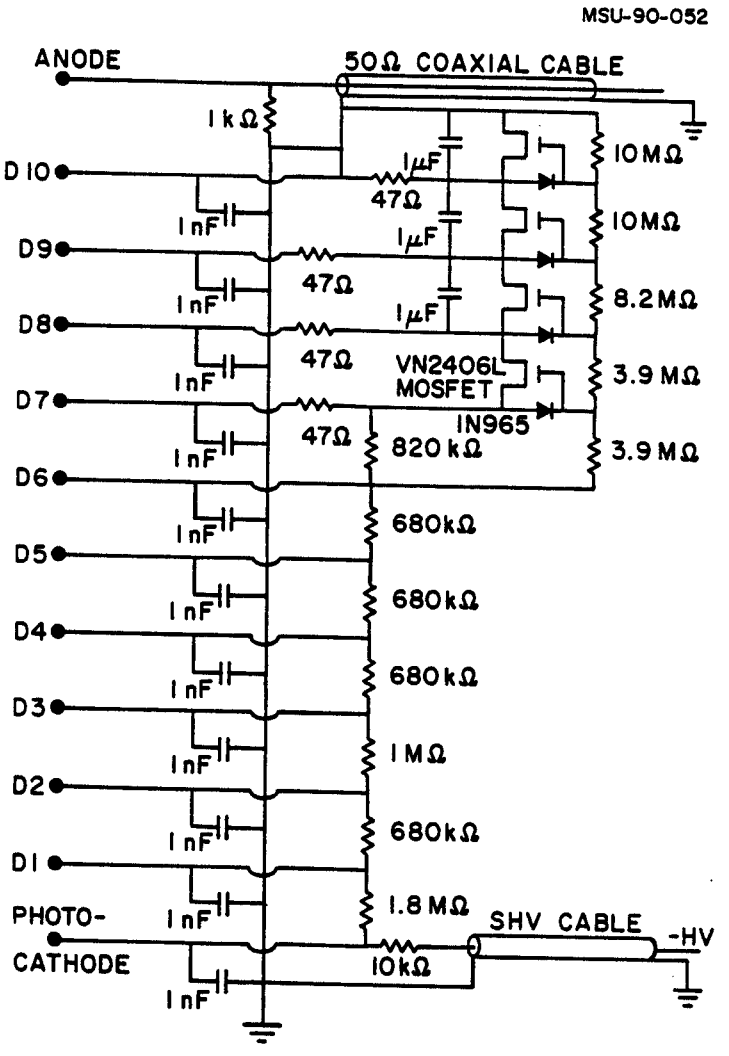

Figure 3.7 Schematic of the active voltage divider used for the Miniball detectors.

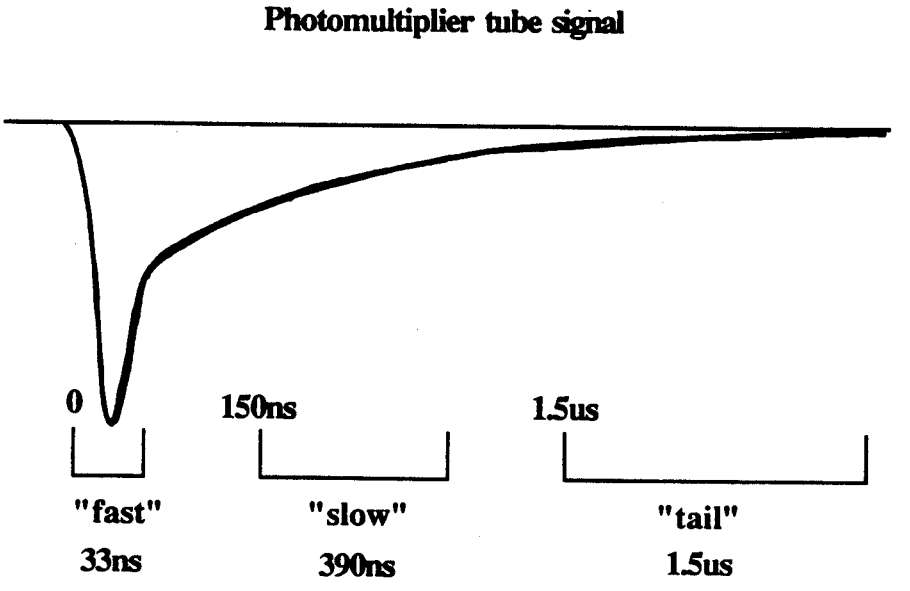

Figure 3.8 Schematic of photomultiplier sygnal with three time gates applied.

has the shape depicted in Figure 3.8. It consists of fast and slow light components. We apply and integrate the charges with three different gates, "fast", "slow", and "tail". The "fast" and "slow" signals represent approximate ΔE (energy loss in fast plastic foil) and E (energy loss in CsI(Tl) crystal) signals. The elemental resolution is achieved in the 2-dimensional map of the "fast" and "slow" signals because of the dependence of stopping power dE/dx on the particle charge, mass, and energy.

The CsI(Tl) crystal has several good characteristics as a stopping scintillator. First, it has large stopping power because of its relatively large density ($4.51 g/cm^3$). Hence a large dynamic range could be achieved with relatively short crystals. Second, its light output has two components of different decay times. One component (dominating the "slow" signal) has decay times of 0.4 - 1 μs, depending on various particle type and energy [Sto58,Ben89,Kes69]. The second component is governed by decay times of the order of 4-7 μs [Ben89,Sto58,Kes69]. This component dominates the "tail" signal. The relative intensity of the "slow" and "tail" components depends on the specific energy loss of the detected particles. From this property the mass resolution of H and He isotopes can be achieved using the pulse shape discrimination [Ala86,Ben89]. An example of the applied time gates is shown in Figure 3.8. Third, CsI(Tl) has good energy resolution for charged particles (about 1% for 100MeV α particle) compared with other scintillator materials such as plastic scintillator [Gon88]. So to achieve the requirements listed earlier we investigated the characteristics and fabrication methods of these scintillators in great detail.

3.4 Uniformity of Scintillation Efficiency of CsI(Tl)

Previous experience with CsI(Tl) crystals used for the detection of energetic particles had revealed difficulties with the production of scintillators with uniform scintillation response [Gon88,Gon90c]. Therefore, considerable attention was paid to select CsI(Tl) crystals of uniform scintillation efficiency. In previous tests of large cylindrical CsI(Tl) crystals [Gon88,Gon90c], non-uniformities of the scintillation efficiency were detected by measuring the response to collimated γ-rays. Such measurements are relatively easy to perform since they can be done in air. However, they are less suitable for small volume crystals, since collimated γ-rays sample a relatively large volume of the crystal. Small scale fluctuations of the scintillation efficiency may stay undetected. In addition, measurements for small non-cylindrical crystals are less precise, since the shape of the Compton background depends on the position of the collimated γ-ray source. Such dependences lead to additional uncertainties in the extraction of the photopeak position.

It was determined, however, that nonuniformities of the scintillation efficiency can be detected very sensitively by scanning the CsI(Tl) crystals with a collimated α-source in vacuum. All crystals ordered from various manufacturers were rectangular in shape with dimensions of 2"×1.5"×1". They were polished at the front and back faces (with dimensions of 2"×1.5") and sanded at the sides. The back face was optically coupled to a clear acrylic light guide with the same dimensions as the crystal. This light guide, in turn, was optically connected to a photomultiplier tube of 1" diameter. The sides of the CsI(Tl) crystal and of the light guide were wrapped with white teflon tape. By covering the front face of the CsI(Tl) scintillator with an aluminized mylar foil, a uniform light collection efficiency was achieved. (Without a reflective entrance foil, the light collection

efficiency decreased by about 5% from the center of the front face to its sides.) The front face of the crystal was scanned in vacuum and the peak location of the 8.785 MeV α-line from a collimated ^{228}Th α-source was monitored. In order to avoid edge effects, regions within about 2 mm of the side boundaries of the crystal were not scanned. Most tests were performed with a simple multichannel analyzer equipped with a peak sensing ADC; in those instances the anode signal of the photomultiplier was shaped and amplified with standard electronics, using integration and differentiation times of 1 μs.

Figure 3.9 shows the results of a scan for a crystal exhibiting a large gradient of the scintillation efficiency. The horizontal axis of the plot shows the location of the collimated α-source with respect to the center, along the short symmetry axis of the front face. Different surface treatments of the front face of the scintillator did not affect the measured variation of the scintillation efficiency. In order to demonstrate that such variations were related to the bulk material of the scintillator we exchanged the role of front and back faces of this scintillator and performed an equivalent scan of the parallel surface (i.e. the previous back face). The results of the two scans are compared by the solid and open points in Figure 3.9. (The coordinate system was kept fixed with respect to the CsI(Tl) crystal.) Nearly identical variations of the scintillation efficiency are observed across the two parallel scintillator surfaces indicating that the measured large gradient of the scintillation efficiency persists through the bulk material of the sample.

The measurements shown in Figure 3.10 were performed by integrating the anode current of the photomultiplier with a charge integrating ADC using time gates of Δt = 0.1-0.5 μs and Δt = 1.1-4.1 μs which select the fast and slow scintillation components of CsI(Tl). The fast component exhibits a larger variation of the scintillation efficiency than the slow component. Since the

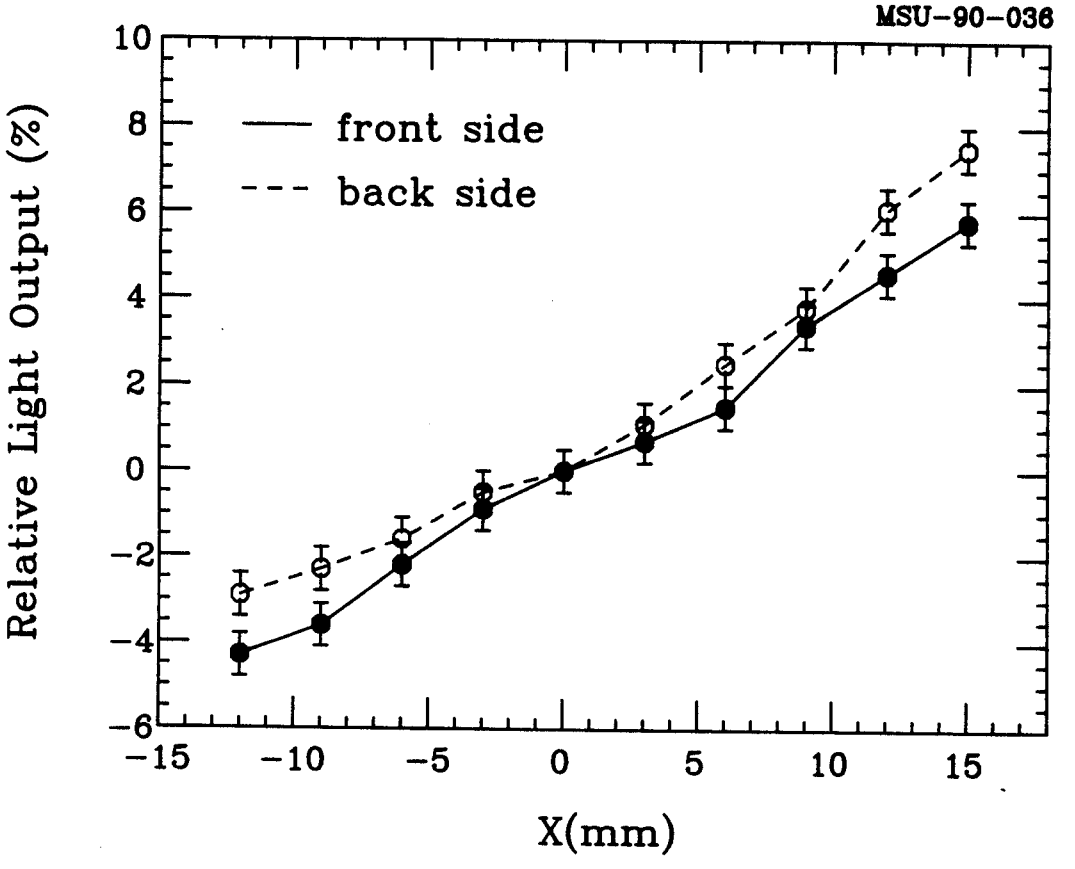

Figure 3.9 Relative variation of scintillation efficiency measured for two parallel surfaces of a CsI(Tl) crystal by using a collimated α-source. The axes of the coordinate system are parallel to the sides of the scintillator; the coordinates are fixed with respect to the scintillator.

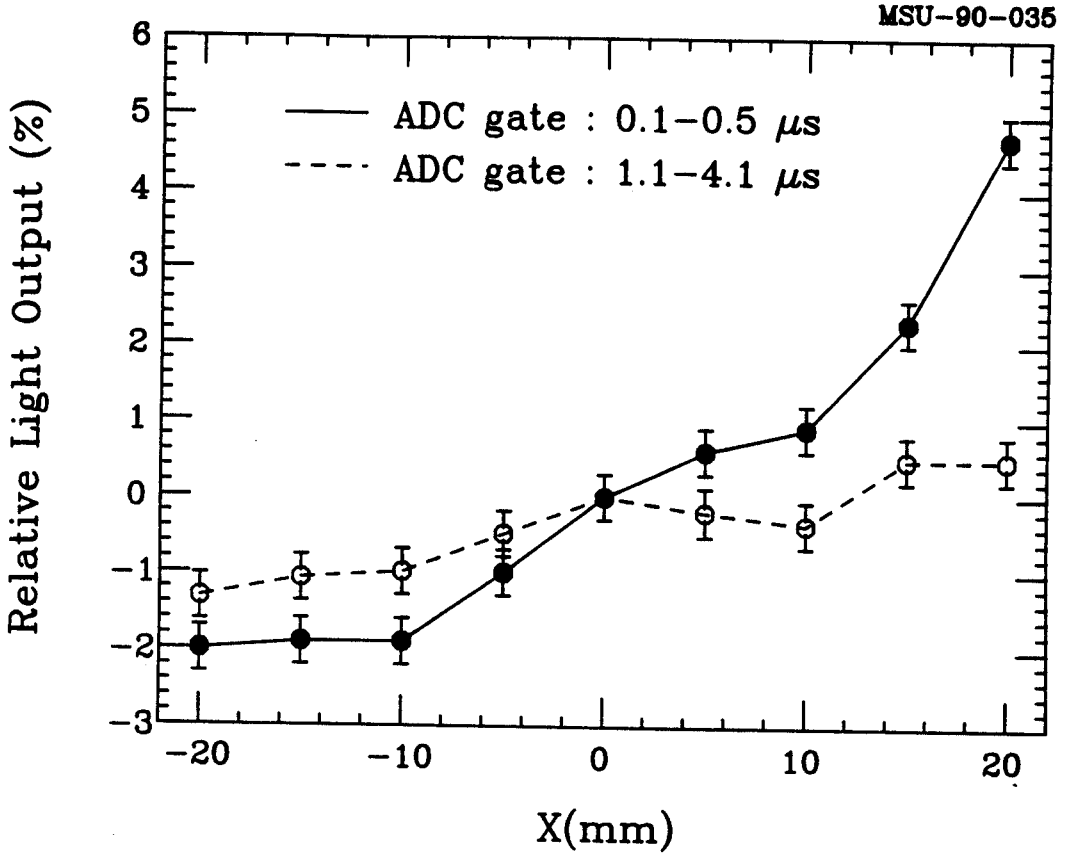

Figure 3.10 Variations of scintillation efficiency measured with a charge integrating ADC for two different time gates selecting the fast and slow components of scintillation for CsI(Tl).

relative intensity of fast and slow scintillation components depends strongly on the Tl concentration [Bir64,Man62], the observed variations of scintillation efficiency are most likely due to gradients in the Tl concentration.

Crystals incorporated into the Miniball were preselected by scanning the 1.5"×2.0" rectangular surface of original crystals along two perpendicular axes and requiring a uniformity of scintillation response better than 3%. The preselected crystals were then milled into their final shapes and scanned a second time, requiring uniformity of response within 2.5%. The preselection process avoided expensive machining of poor quality crystals; it was about 90% efficient for the selection of crystals of the desired quality.

Figure 3.11 compares variations of scintillation efficiency detected with collimated α-particles of 8.785 MeV energy (source: ^{228}Th) and γ-rays of 662 keV energy (source: ^{137}Cs). The left and right hand panels give examples for a rejected and an accepted crystal, respectively. The enhanced sensitivity of the α-particle scan is obvious. It is probably caused by the fact that α-particles sample a much smaller volume than γ-rays and that the two kinds of radiation exhibit different sensitivities to the Tl concentration [Bir64,Man62].

The results of our standardized prescans are displayed in Figure 3.12. The histogram shows the number of scanned crystals, obtained from different companies, as a function of maximum detected scintillation uniformity. Crystals obtained from one supplier (a) were grown with the Czochralski technique [Czo18,Bric65]; crystals obtained from three other suppliers (b-d) were grown with the Stockbarger-Bridgman technique [Bric65,Brid25]. Crystals grown with the Czochralski technique exhibited, on average, more uniform scintillation efficiencies than crystals grown with the Stockbarger-Bridgman technique. Quality differences between different suppliers using the Stockbarger-Bridgman technique may not be significant since only a limited number of crystals were

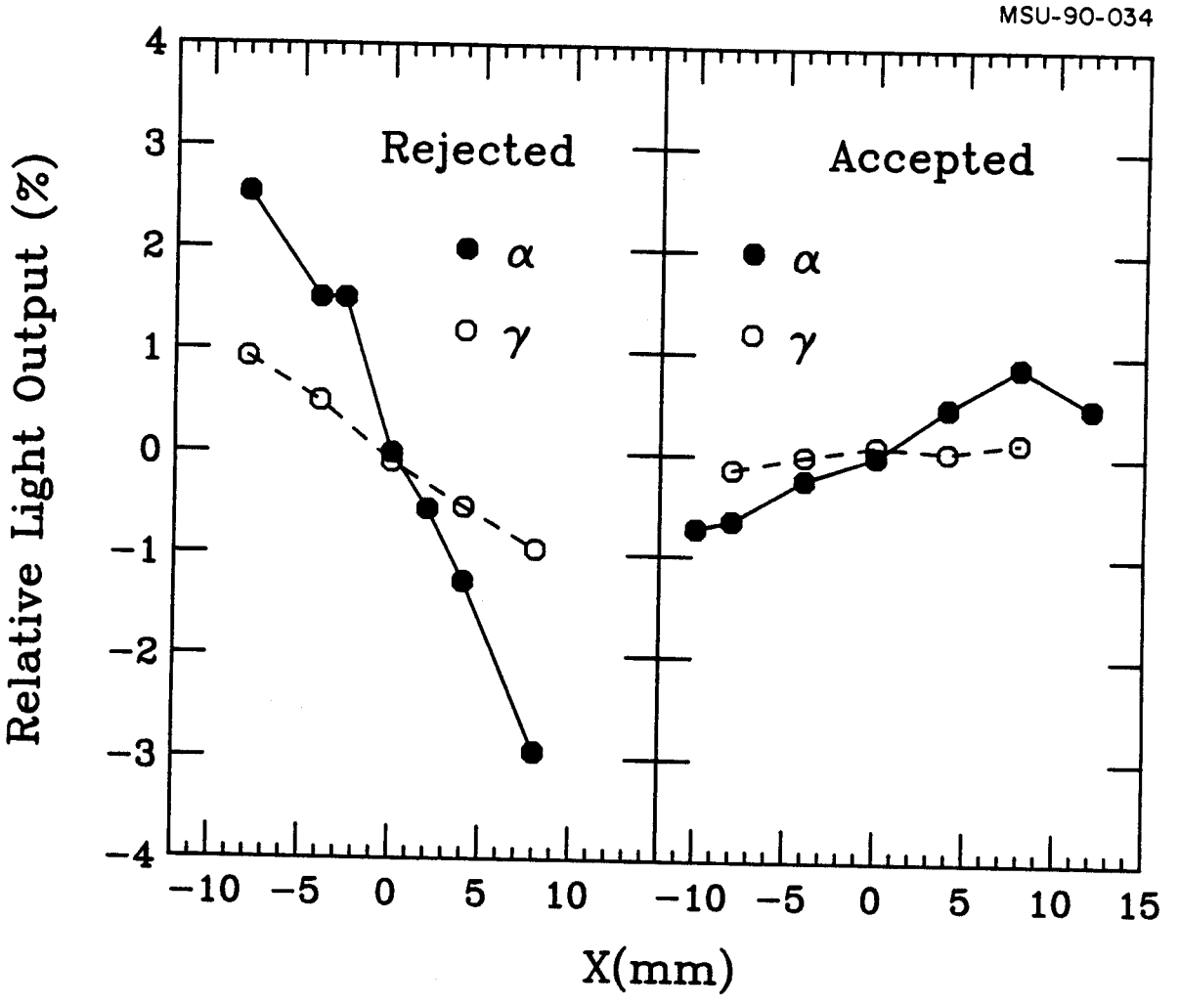

Figure 3.11 Variations of scintillation efficiency detected with collimated α-particles of 8.785 MeV energy (solid points) and collimated γ-rays of 662 keV energy (open points). The left hand panel shows the measurement for a detector which was rejected. The right hand panel shows the measurement for a detector which was incorporated into the Miniball.

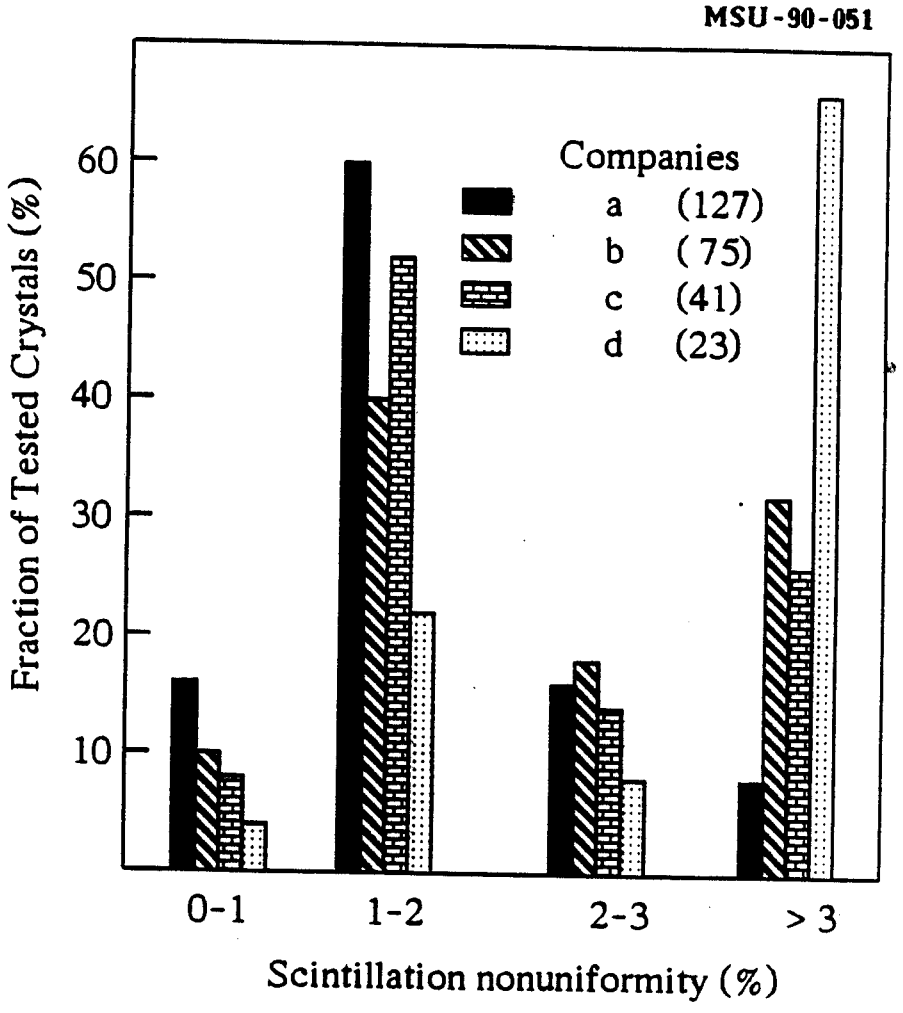

Figure 3.12 Maximum detected scintillation nonuniformity for crystals obtained from different suppliers. The number of crystals scanned for each supplier is given in parenthesis.

scanned for each supplier. (The number of crystals scanned from each supplier is given in parentheses in Figure 3.12.) Furthermore, some differences are expected to result from different ways of cutting the 2"×1.5"×1" crystals from the ingot, since Tl concentration gradients build up largely in the vertical crystal growth direction. Our standard scan of the 1.5"×2.0" face of each crystal should then reveal an especially large gradient of the scintillation efficiency when the 2" long side was cut parallel to the vertical growth direction of the ingot. Selective cuts of some crystals from various locations of the ingot and with different orientations with respect to the crystal growth direction provided supporting evidence for the relationship between the Tl concentration and the uniformity of scintillation response. For most of the crystals, such detailed information was not available to us.

3.5 Fabrication of Scintillator Foils

Scintillator foils were made by using the so called "spin-coating method" [Mey78,Nor87]. The original Beta-paint solution was ordered with a 40% weight ratio of scintillator material to xylene. It was then diluted by adding more xylene to about 30% until the solution had the desired viscosity of 20-30 poise. After we measured the viscosity of the solution, we stirred this solution inside a brown bottle using a stainless steel rod for about 5-10 minutes to mix it well and achieve optical uniformity. Then we let the solution in this bottle setle for about half day before spinning to remove all the bubbles generated during stirring.

The viscosity was determined by measuring the terminal speed, v, of a steel ball sinking in a glass tube filled with a sample of Beta-paint. Correcting Stoke's Law for the finite diameter of the glass tube gives the following expression for the viscosity [Din62]:

$$\eta = \frac{2gr^2(\rho_o-\rho)}{9v}\left(1-2.104\left(\frac{r}{R}\right)+2.09\left(\frac{r}{R}\right)^3-0.95\left(\frac{r}{R}\right)^5\right). \qquad (3.1)$$

Here, η denotes the viscosity, r and R are the diameters of the steel ball and the glass tube, g is the gravitational acceleration, and ρ_o and ρ are the densities of the steel ball and the Beta-paint, respectively.

For the fabrication of scintillator foils, a glass plate of 23 cm diameter was mounted horizontally on a small platform connected to the drive of an electrical motor which allowed spinning of the plate about its center at a preselected speed. To facilitate the removal of spun foils, the glass plate was covered successively with metasilicate solution and Teepol 610 and then wiped to leave only a thin film of the releasing agents on the glass substrate. An appropriate amount of beta paint was poured on the center of a glass plate. In order to provide rapid spreading of the initial solution, the plate was spun at an enhanced speed for the first few seconds until the entire plate was covered with Beta-paint. Following this rapid startup, the glass plate was spun at the preset rotational frequency for a duration of approximately 4 min until a solid foil had formed. After spinning, the glass plate was stored in a flow of dry nitrogen for a duration of about eight hours. The foil was then peeled from the glass plate, mounted on a frame, and placed in a dry nitrogen atmosphere for another 24 hours to allow further evaporation of residual xylene.

We obtained good and reproducible results by using more dilute solutions and spinning at lower rotational frequencies than described in refence [Nor87]. A number of measurements were performed to determine the relation between rotational frequency and foil thickness in this operating range. The results of these measurements are shown in Figure 3.13. For each foil, thickness and homogeneity were determined by scanning the foil in vacuum with a collimated ^{228}Th α-source and measuring the energy of the transmitted α- particles in a

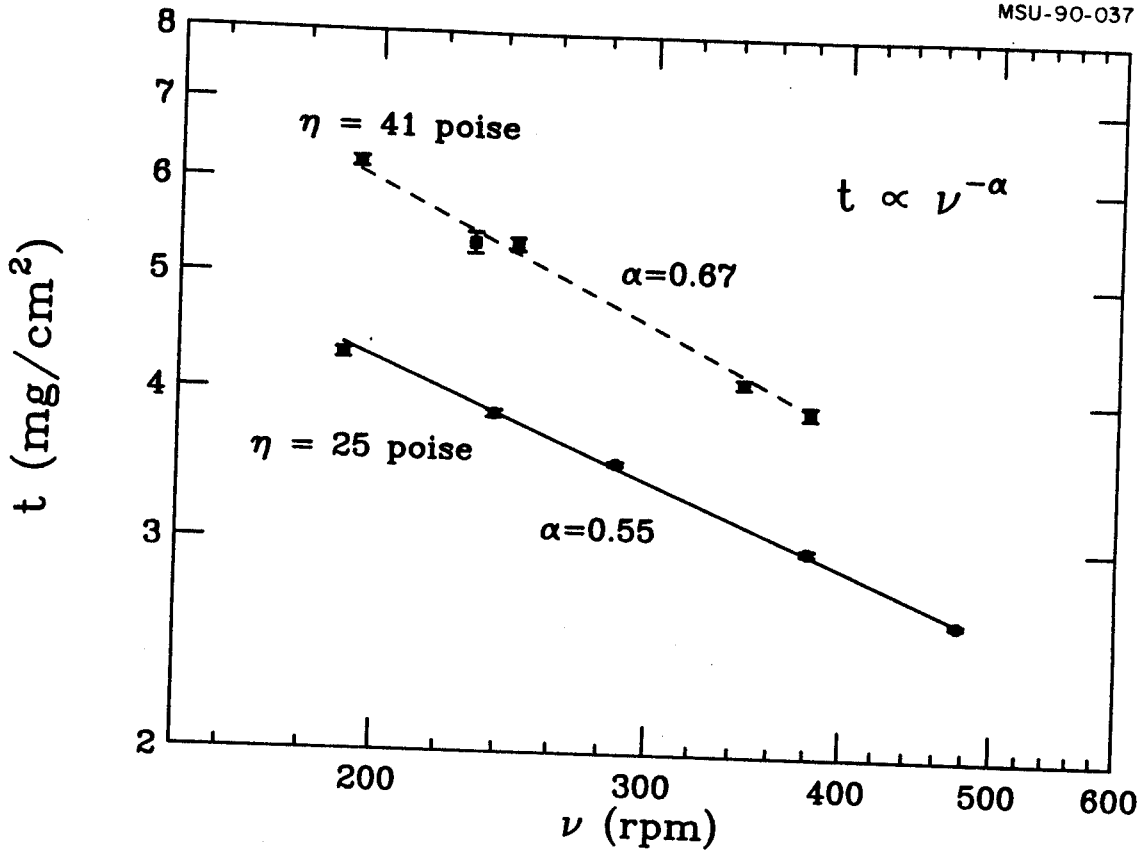

Figure 3.13 Relation between scintillator foil thickness and rotational frequency of spinning measured for solutions of Beta-paint of different viscosity. The lines show fits with the power law expression, $t \propto \nu^{-\alpha}$.

calibrated silicon detector. The energy loss in the foil was then converted to an areal density according to reference [Lit80]. The spun foils were uniform in thickness to within typically 1-2% over an area of 7×7 cm^2. Scintillator foils used for instrumenting the Miniball in its present configuration were selected to have a thickness of 4.0 ± 0.12 mg/cm^2.

We have explored the light collection efficiency for scintillator foils placed with and without optical cement on the front faces of the CsI(Tl) scintillators. Considerable effort was spent on developing a technique which provides an optically clear glue bond of minimum thickness between the plastic scintillator foil and CsI(Tl) crystal. Best results were obtained with Epo-tek 301 which has a low viscosity of 1 poise and a curing time of 1 day. A thin layer of the epoxy was distributed on the scintillator foil by spin coating. By means of a thin rubber pad and a weight, the epoxy coated foil was pressed onto the CsI(Tl) crystal in vacuum and cured in a clean and dry nitrogen atmosphere. The pressure applied by the weight was typically 13 kPa. Glue layers of 300-500 $\mu g/cm^2$ areal density were achieved, with nonuniformities of the order of 50%.

We investigated the position dependence of the light collection efficiency for phoswich detectors prepared with and without glue bonds between the plastic scintillator foil and the CsI(Tl) crystal, by measuring the response at various locations on the front face (labelled 1 through 11 in Figure 3.14). The upper and lower panels in Figure 3.14 show the relative variations of the plastic scintillator response (integrated over the time interval Δt_{fast} = 0-50 ns) and the fast CsI(Tl) component (integrated over the time interval Δt_{slow} = 60-400 ns) for α-particles sampling different locations of a phoswich fabricated with (upper panel) and without (lower panel) a glue bond between the two scintillators. Both detectors have sufficient uniformity of response to provide good particle identification (see also Section 3.7). In this bench test, a better uniformity of

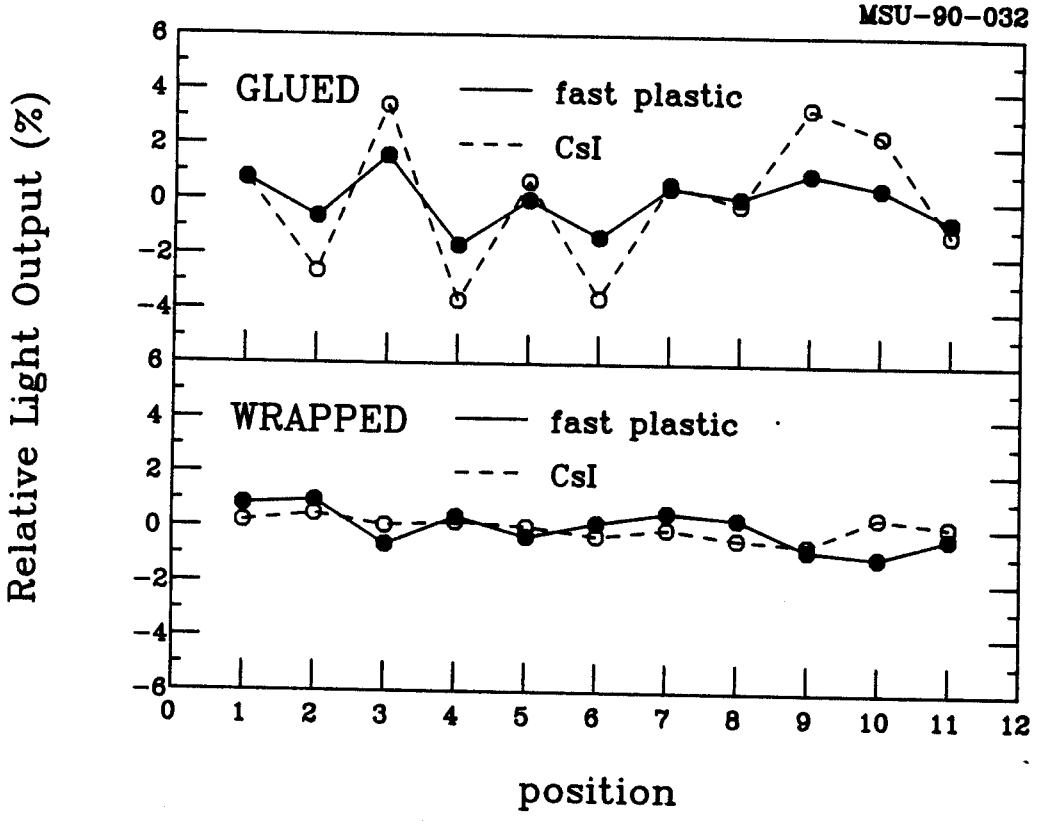

Figure 3.14 Position dependent response of phoswich detectors with (upper panel) and without (lower panel) glue bond between plastic and CsI(Tl) scintillators. Solid and open points show charges integrated by the "fast" and "slow" time gates, Δt_{fast}=0-50 ns and Δt_{slow}=60-400 ns, respectively. The same foil and CsI(Tl) crystal were used in this test. Various positions sampling the entrance window are labelled 1-11.

response was obtained for the phoswich without glue bond. Somewhat larger (but still tolerable) fluctuations are observed when a glue bond is applied. The observed fluctuations can be attributed to thickness variations of the glue layer which cause variations in energy deposition in the stopping CsI(Tl) scintillator (see open points in the top panel). Since some of the CsI(Tl) signal overlaps in time with the fast plastic scintillator signal, a correlated modulation appears in the charge integrated by the fast time gate. For more energetic particles, this effect should be less important as the energy loss in the glue layer decreases.

The fabrication of phoswich detectors without glue bond has the advantage of allowing changes in scintillator foil thickness to be made relatively easily. Glued phoswich detectors, on the other hand, are mechanically more rugged. In our test runs, improved particle identification was obtained with glued phoswich detectors (see Section 3.7). However, these improvements do not appear to be compelling enough to justify the initial use of glue bonds in the Miniball array. So all the experiments up to the present time (September of 1991) have been performed without glue layer between fast scintillator and CsI(Tl) crystal.

3.6 Data Acquisition Electronics

Figure 3.15 shows a block diagram of the data acquisition electronics. The anode current from the photomultipliers is split via passive splitters into the "fast", "slow", "tail", and "trigger" branches of relative amplitudes $I_{fast} : I_{slow} : I_{tail} : I_{trig} \approx 0.82 : 0.04 : 0.04 : 0.1$. The "slow" and "tail branches are connected directly from the splitter to their respective fast encoding readout analog-to-digital converters (FERAs). The gates for the "slow" and "tail" FERAs are 390 ns and 1.5 μs wide and open 150 ns and 1.5 μs after the leading edge of the linear signal, respectively. For the "fast" branch, a linear gate(Phillips 7145) is inserted between

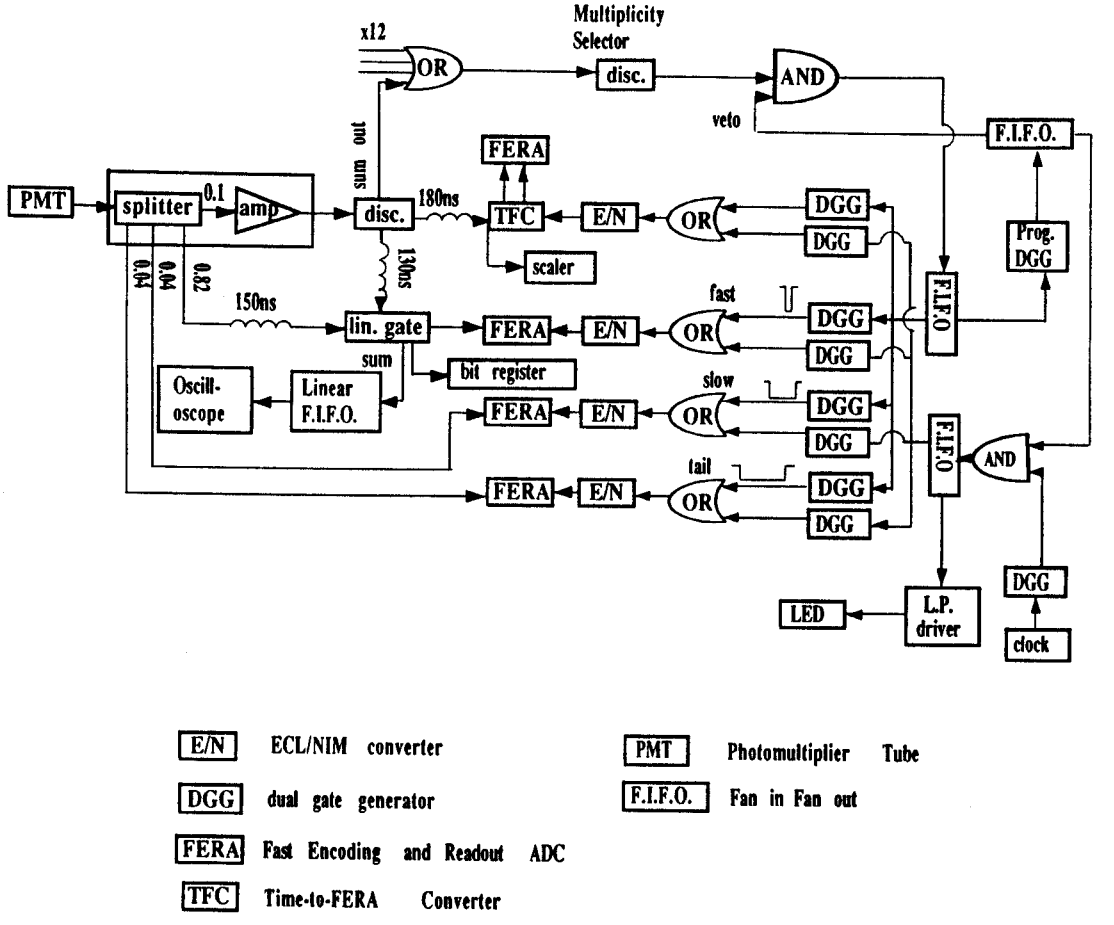

Figure 3.15 Schematic diagram of the data acquisition electronics of the Miniball.

the passive splitter and the "fast" FERA. This linear gate allows the individual gating of each "fast" channel which cannot be achieved with the common gate FERAs (see also the discussion in Section 3.7). The linear gate is opened 10ns prior to the leading edge of the linear signal and for a duration of 33 ns. The "fast" FERA is gated by a common gate of 140 ns width which begins approximately 60 ns prior to the leading edge of the linear input signal. The trigger branch, I_{trig}, is re-amplified by a fast amplifier and fed into a leading edge discriminator module (Phillips 7106), the output of which provides the stop signal for the time-to-FERA-converter and opens the linear gate for the "fast" channel. The detailed timing diagram is shown in Figure 3.16.

Each discriminator module provides a sum output for its 16 channels. The amplitude of this sum signal is proportional to the number of channels which have triggered. By setting a discriminator level on the linear addition of all discriminator sum outputs, a simple multiplicity trigger is obtained. Each discriminator channel has 1.5 μs internal dead time to prevent double triggering.

In order to reduce dispersive losses for the fast anode current pulse representing the response of the plastic scintillator, the data acquisition electronics is located close to the measurement station. Discriminator thresholds and photomultiplier gains are adjusted via remote computer control. Remote inspection of each detector signal is also possible by using the sum output of the linear gate modules and selectively masking the discriminators.

3.7 Particle Identification

The particle identification resolution of various phoswich detectors was tested for fragments emitted at about $\theta_{lab} \approx 35^\circ$ in the $^{40}Ar + ^{197}Au$ reaction at E/A=35 MeV. All data were taken with the standard electronics setup described

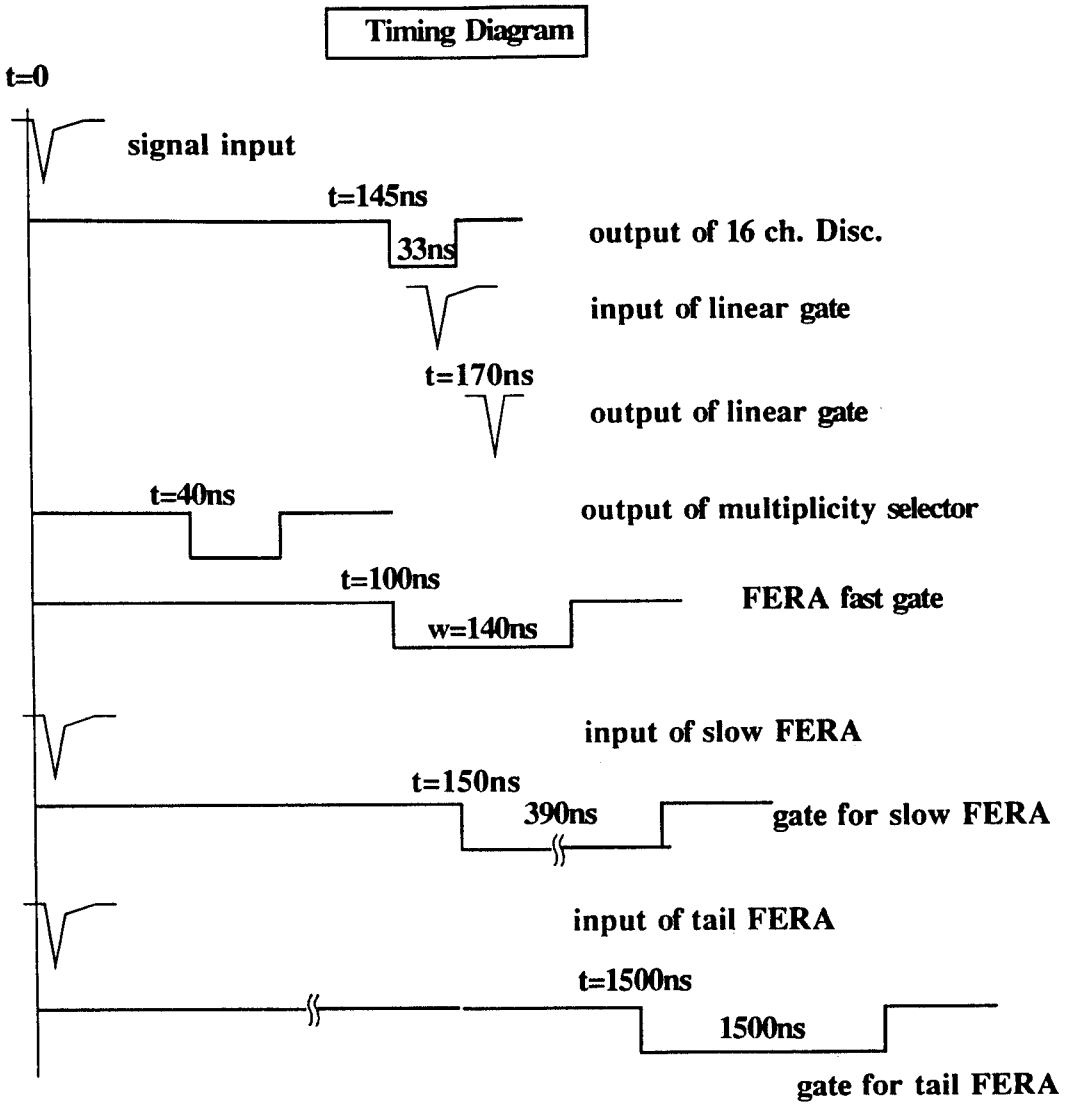

Figure 3.16 Timing diagram of analog signal and gates.

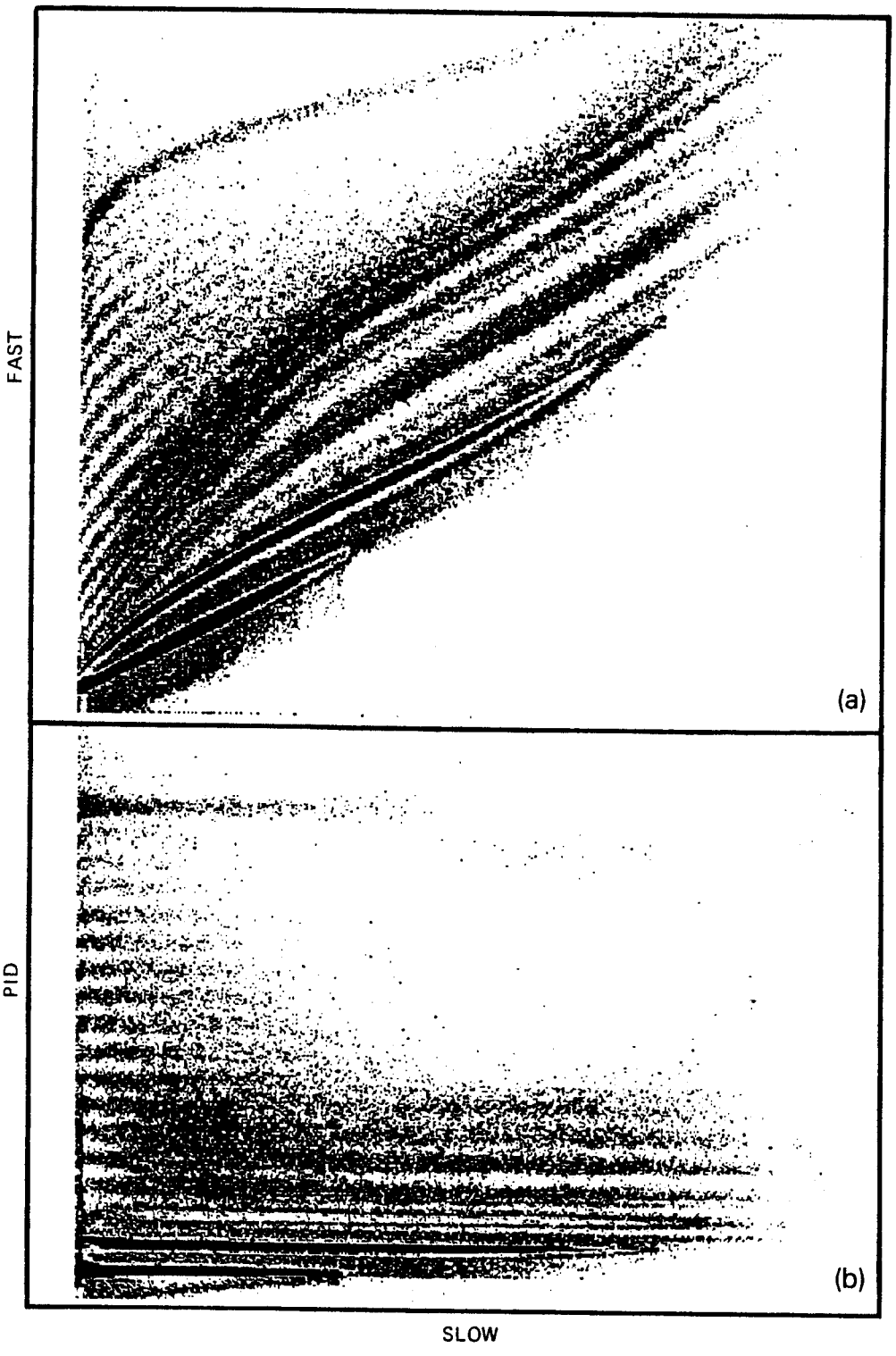

Figure 3.17 Particle identification obtained from two-dimensional "fast" vs. "slow" matrix for reaction products emitted at θ_{lab}=35° for the $^{40}Ar+^{197}Au$ reaction at E/A=35 MeV; a scintillator foil of 4 mg/cm^2 areal density was used with a thin glue coupling to the CsI(Tl) crystal. (a) Matrix of raw data. (b) Linearized matrix. An intensity threshold of 2 counts per channel has been set.

in the previous section. Part (a) of Figure 3.17 shows a two-dimensional plot of the "fast" versus the "slow" charge integration parameters for a phoswich consisting of a 4 mg/cm^2 scintillator foil glued to the CsI(Tl) crystal. Elemental identification up to Z=18 is achieved over a considerable dynamical range of particle energies. Part (b) of the figure shows a linearized presentation of these data which is more suitable to display the resolution of the device. From such a linearized presentation, projections on the particle identification axis can be generated which show the particle identification resolution in a more quantitative form.

Spectra projected on the particle identification axis are shown in Figure 3.18. Part (a) of the figure shows the projection of the data displayed in Figure 3.17; part (b) show the result for a phoswich using a 4 mg/cm^2 scintillator foil without glue bond. Better resolution is obtained by using a glue bond between the scintillator foil and the CsI(Tl) crystal. Additional improvements in particle identification resolution can be achieved by increasing the thickness of the scintillator foil. For a specific experiment, the benefits of improved particle identification resolution due to an increase in scintillator foil thickness must be weighed against the ensuing higher energy threshold. We have also explored the use of thinner foils and found that the resolution deteriorates rapidly for scintillator foils thinner than 3 mg/cm^2. For most purposes, particle identification provided by foils of 4 mg/cm^2 thickness is satisfactory.

The use of thin scintillator foils in phoswich detectors for particle identification is complicated by the fact that the fast plastic scintillator signal is superimposed on the rising signal from the CsI(Tl) scintillator. Good particle identification via direct charge integration depends critically on well defined integration times. Electronic walk introduced by leading edge discriminators changes the detailed shape of a particle identification line in the "fast" versus

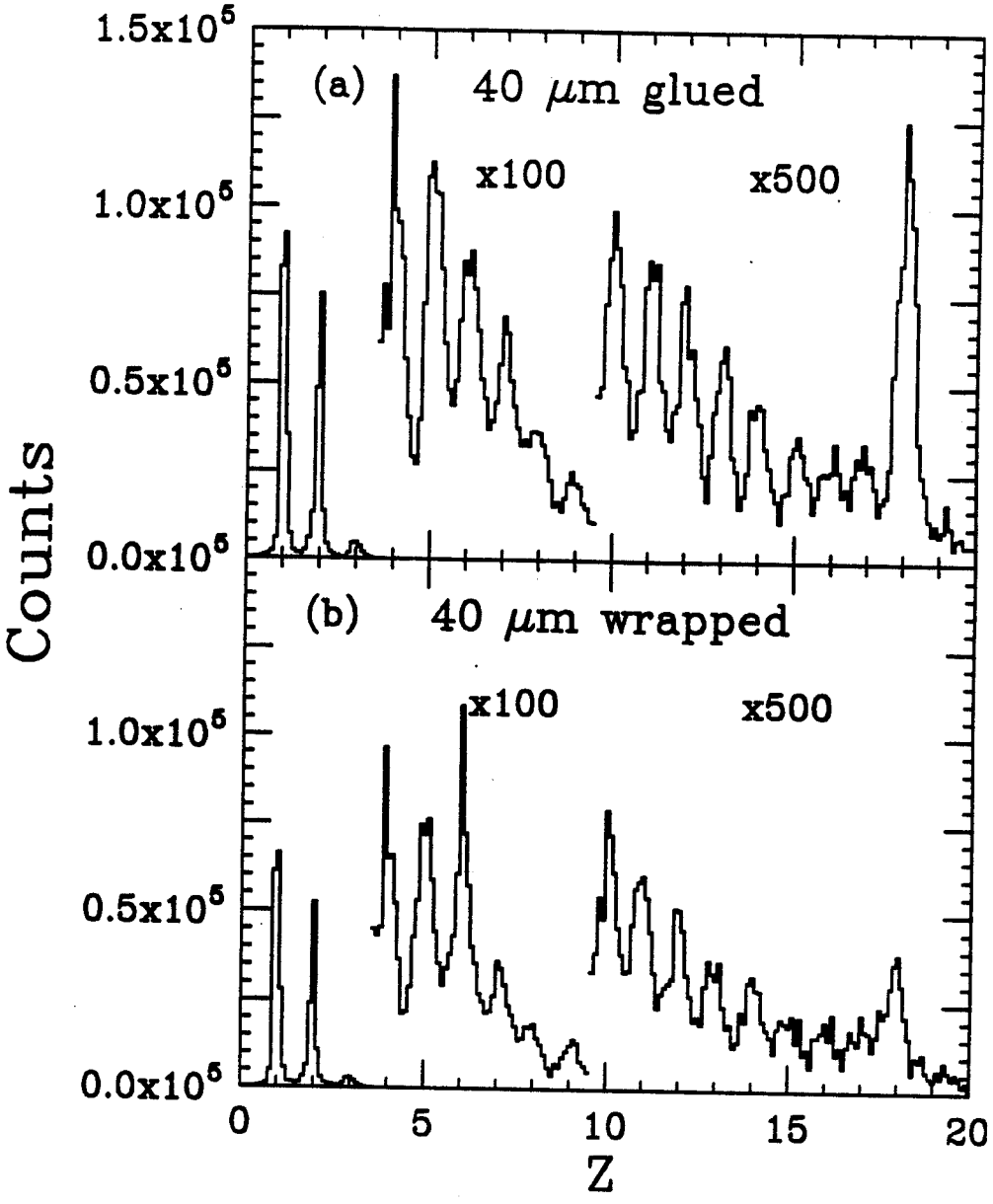

Figure 3.18 Projections of linearized particle identification spectra for reaction products emitted in the $^{40}Ar+^{197}Au$ reaction at $\theta_{lab} \approx 35°$ using phoswich detectors using scintillator foils of 4 mg/cm^2 thickness, (a) with and (b) without glue coupling between the scintillator foil and the CsI(Tl) crystal.

"slow" matrix, but it has only minor effects on the separation between adjacent particle identification lines. Time jitter in the integration gate, however, does have an adverse effect on the particle identification resolution, since it produces fluctuations in the amount of CsI(Tl) scintillation integrated by the fast time gate. If the fast component is integrated by ADCs with a common gate mode, loss in resolution will occur whenever there is a time jitter between gates provided by different channels. Loss in resolution will be inevitable when more than two detected particles with different flight times are converted in separate channels of a common gate ADC. For example, the difference of flight times between 70MeV proton and 70MeV carbon detected in ring 2 is approximately 2ns. The problem can be avoided by introducing linear gates into the "fast" channel which are individually opened (see Figure 3.15).

Figure 3.19 illustrates the sensitivity of the particle identification to time jitter in the integration gate for the "fast" channel. The solid curves correspond to the centers of selected particle identification lines in the "fast" versus "slow" matrix (see, e.g. Figure 3.17). The dashed curves show how these particle identification lines are shifted when the gate of the "fast" ADC arrives two 2 ns later in time. (In these two measurements, the gate width was kept constant.) Even a 2 ns time jitter in the "fast" gate is sufficient to mix the particle identification lines of neighboring elements in the "fast" versus "slow" matrix.

3.8 Light Pulsing System

Gain drifts of the photomultiplier tubes are monitored by a simple and compact light pulser system which operates in vacuum. In order to preserve the modularity of the device and avoid unnecessary removal of optical fibers during transport, each detector ring is provided with its own light pulser system. Figure

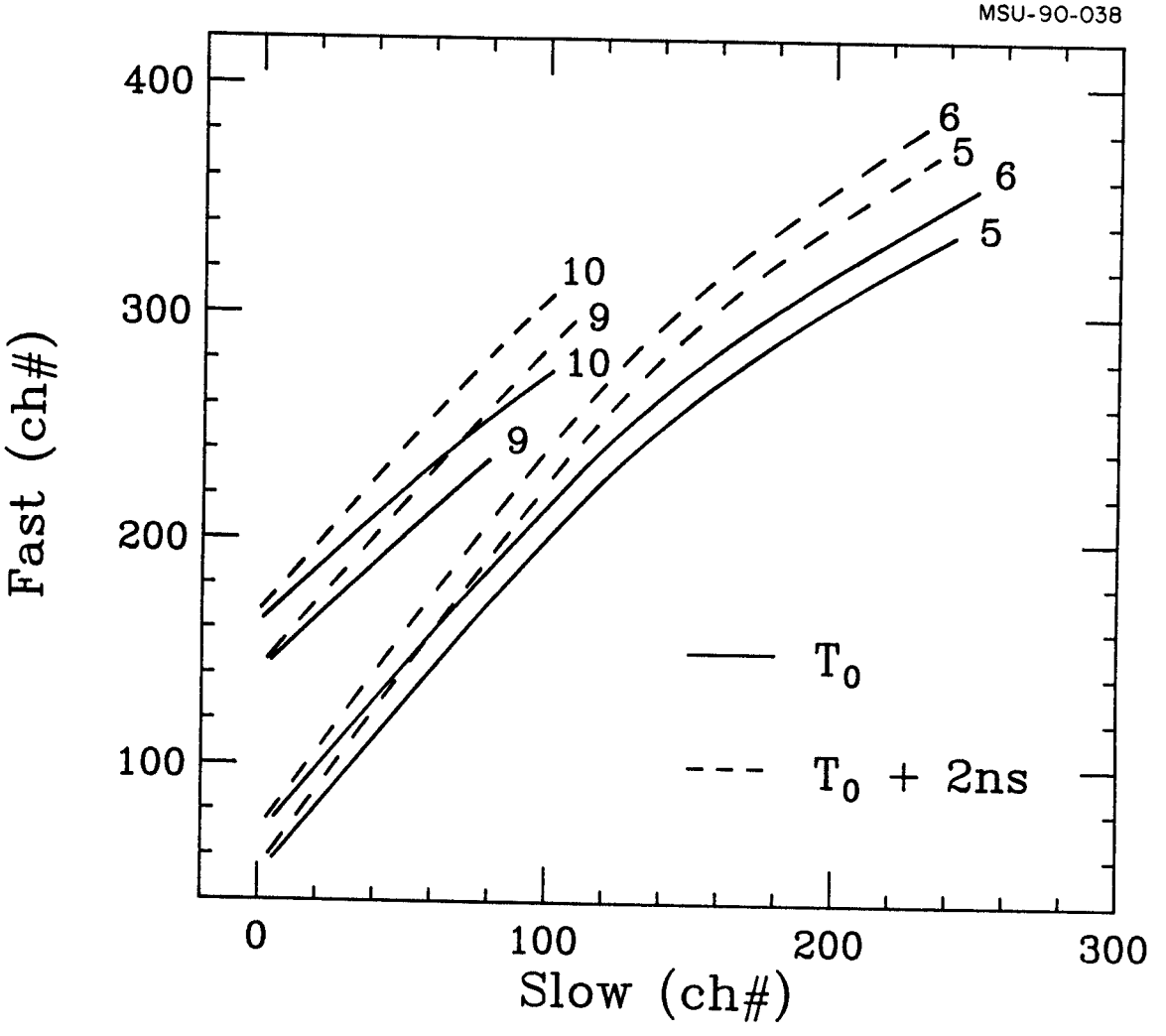

Figure 3.19 Sensitivity of particle identification to time shift of the "fast" charge integration gate. The solid and dashed lines show the loci of representative particle identification lines in the "fast" vs. "slow" identification matrix obtained for gates displaced by 2 ns with respect to each other.

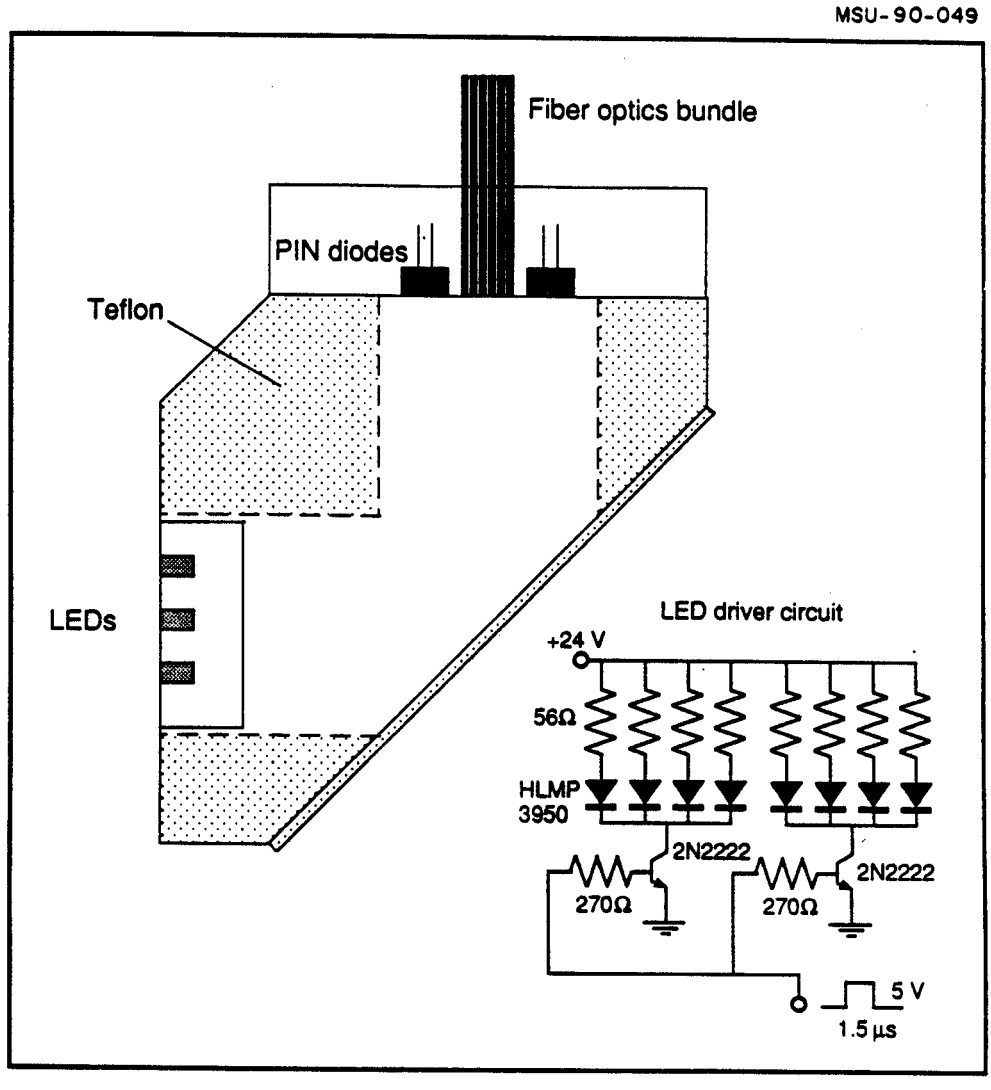

Figure 3.20 Schematics of light pulser assembly and LED trigger circuit.

3.20 shows schematics of the mechanical assembly of the light pulser system and of the driving circuit for the light emitting diodes (LEDs) which is triggered by an external NIM logic signal. During experiments, the light pulser is triggered at a rate of about 1 Hz. Light is generated by simultaneously pulsing an array of eight LEDs (Hewlett Packard HLMP-3950) which generate light at wavelengths around 565 nm. The emitted light is diffused by reflection from an inclined teflon surface. Light fibers which only view scattered light transport the light to the individual photomultipliers.

Because of temperature fluctuations and aging effects, operation of light emitting diodes may not be stable over long periods of time. Therefore, the intensity of each light pulse is monitored by two PIN diodes (Hamamatsu S1223) read out by standard solid state detector electronics. The ratio of the signals of the two PIN diodes can be used to monitor their stability. The ratio of pin diode and photomultiplier signals can then be used to monitor the gain of the individual photomultiplier tubes according to the relation:

$$Ch' = Ch \times (Pin1+Pin2)/2Pmt\,. \qquad (3.2)$$

Here, Ch denotes the ADC conversion measured for a given event, Ch' is the conversion corrected for gain shifts, and Pmt, Pin1, and Pin2, are the channel numbers for LED generated light pulses detected by the individual photomultiplier tube and the two PIN diodes, respectively. Better than 1% gain stabilization is achieved if the temperature of the CsI(Tl) crystals is kept constant. (Variations of the scintillation efficiency of CsI(Tl) caused by temperature fluctuations cannot be detected with the light pulser.) It was verified, however, that active cooling of the base plate ensures rapid achievement of a stable operating temperature for the Miniball.

Figure 3.21 illustrates the gain stabilization achieved with the light pulser system. The gain variations of a photomultiplier (enhanced by variations of the supply voltage) were directly measured by irradiating a CsI(Tl) crystal with α-particles emitted from a collimated ^{228}Th source and monitoring the peak location of the 8.785 MeV α-line; they are shown by the open points in the figure. The solid points in the figure show the peak positions obtained in the off-line analysis after correcting the gain variations according to information from obtained by the light pulser system. Gain stability to better than 1% was achieved.

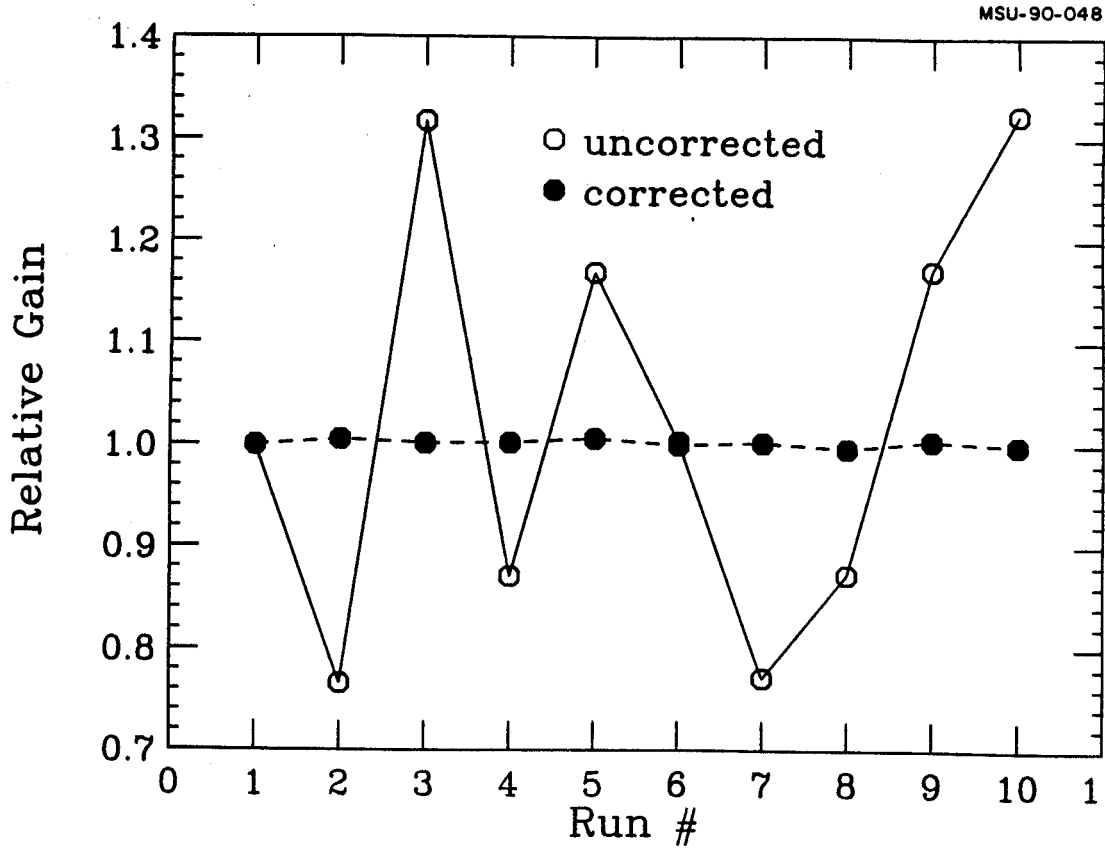

Figure 3.21 Open points: gain variations of a CsI(Tl) photomultiplier assembly determined by measuring the detector response to 8.785 MeV α-particles; solid points: same data corrected for gain shifts in the off-line analysis by using information from the light pulser system.

Chapter 4 $^{36}Ar + ^{197}Au$ reaction at E/A = 35 MeV with Miniball

4.1 Experimental setup

The experiment was performed using the MSU Miniball in the 92" diameter scattering chamber of the National Superconducting Cyclotron Laboratory at Michigan State University. An ^{36}Ar beam of energy E/A=35 MeV and intensity $I \approx 10^8$ particles per second (~0.3nA) was extracted from the K500 cyclotron. Typical beam spot diameters were of the order of 2-3 mm. The target foil consisted of 1 mg/cm^2 ^{197}Au. During the experiment, a vacuum of better than 10^{-5} torr was maintained in the scattering chamber. Water and hydrocarbon vapor components in the residual gas were strongly reduced by a large cold trap filled with liquid nitrogen. By this means, carbon deposits on the target were reduced to a negligible level eliminating contamination from auxiliary reactions.

Light particles and complex fragments were detected using rings 2-11 of the Miniball covering scattering angles of Θ_{lab}=16°-160° and subtending a solid angle corresponding to 85% of 4π. As a precaution against secondary electrons, rings 2 and 3 were covered by aluminum foils of 0.81 mg/cm^2 areal density. All the detectors were checked with a Th^{228} α source located at the target position looking at "fast" and "slow" 2-dimensional spectra to see the resolution of the 8.785 MeV α signals. The high voltage supplied to each detectors was adjusted to compensate the variations in the gain and give similar dynamic ranges (Z=1-20) in the "fast" and "slow" 2-dimensional spectra obtained with the beam on target during the early stage of the experiment. Moderately suitable adjustments in the

gain of the photomultipliers could be made by using the approximate relation,

$$\frac{G}{G_0} = \left(\frac{V}{V_0}\right)^{6.8}. \qquad (4.1)$$

This empirical relation was obtained from tests with an α source in which the relation between photomultiplier tube gain and cathode voltage was explored. The temperature was monitored with temperature sensors located at various positions, and the reservoir of the cooling system has been kept at constant temperature of about 15 °C over the duration of the experiment.

The discriminator thresholds are common for sets of 16 channels. They were set slightly above the signal level by electrons emitted in large numbers from the target. Most data were taken with a hardware trigger of $N_{hit} \geq 2$, where N_{hit} denotes the number of detectors firing; a run with reduced statistics was taken with $N_{hit} \geq 1$. Due to the low beam intensity, random coincidences were negligible.

4.2 Data reduction and Analysis

4.2.A. Particle Identification

For each detector three gated charge signals were recorded : "fast", "slow", and "tail". Hence, one can generate three combinations of 2-dimensional spectra for particle identifications. This information is combined to establish the logic to get optimal particle identification. As explained in Section 3.3, elemental resolution for intermediate mass fragments has been achieved from a 2-dimensional "fast" versus "slow" map. To get better channel resolution we transformed the "fast" signal to ;

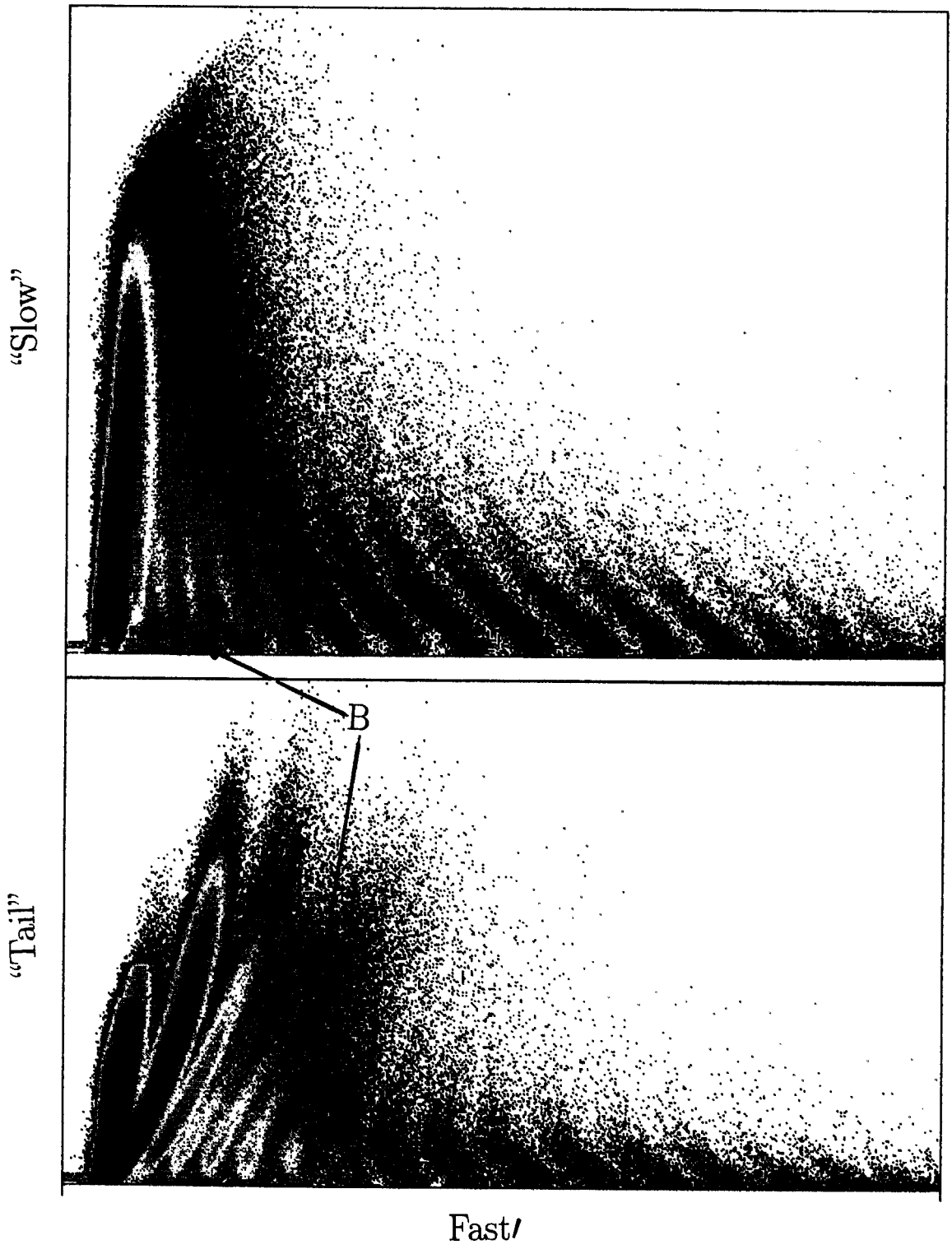

Figure 4.1 "slow"(upper) and "tail"(bottom) versus fast' spectra of a Bicron detector(det # 2-8)

$$fast' = \text{"fast"} - c\text{"slow"}, \qquad (4.2)$$

where c is a constant less than 1. However a number of detectors supplied by one company (Bicron) had better elemental resolution for IMFs ($3 \le Z \le 6$) on the "fast" versus "tail" spectra, possibly due to different thallium doping. Figure 4.1 shows "slow" vs fast' (upper section) and "tail" vs fast' 2-dimensional spectra for a detector using a Bicron crystal (compare this with Figure 4.2 which shows a spectrum from a Hilger crystal). Especially Li, Be, and B have better separations in "tail" vs. fast' spectrum than "slow" vs. fast'. Overall Hilger crystals had better particle identifications than Bicron crystals. We have made individual particle identification gates for each detector to keep the best resolution. At first one line was drawn to separate light charged particles ($Z \le 2$) and intermediate mass fragments ($Z \ge 3$) on the fast' versus "slow" or "tail" spectra (Figure 4.2), and the particles identified as light charged particles were identified on the "slow" versus "tail" spectra by mass.

Figure 4.3 (upper section) shows this "slow" vs. "tail" spectrum, and H and He isotopes are cleary separated on this plot except in the very low energy region where all particles merge together. To get better resolution in the low energy region we transformed the 2D-matrix putting upper and lower bounds as shown in the upper section of Figure 4.3 and expanding the useful dynamic region with full channel resolution. So

$$tail' = C \frac{tail(upper\ bound) - \text{"tail"}}{\Delta(tail)}, \qquad (4.3)$$

where C is constant and Δ(tail) is the difference between upper and lower bounds for given "slow" channel. The transformed 2-dimensional spectrum "slow" versus tail' is shown in the Figure 4.3 at bottom section. Hydrogen

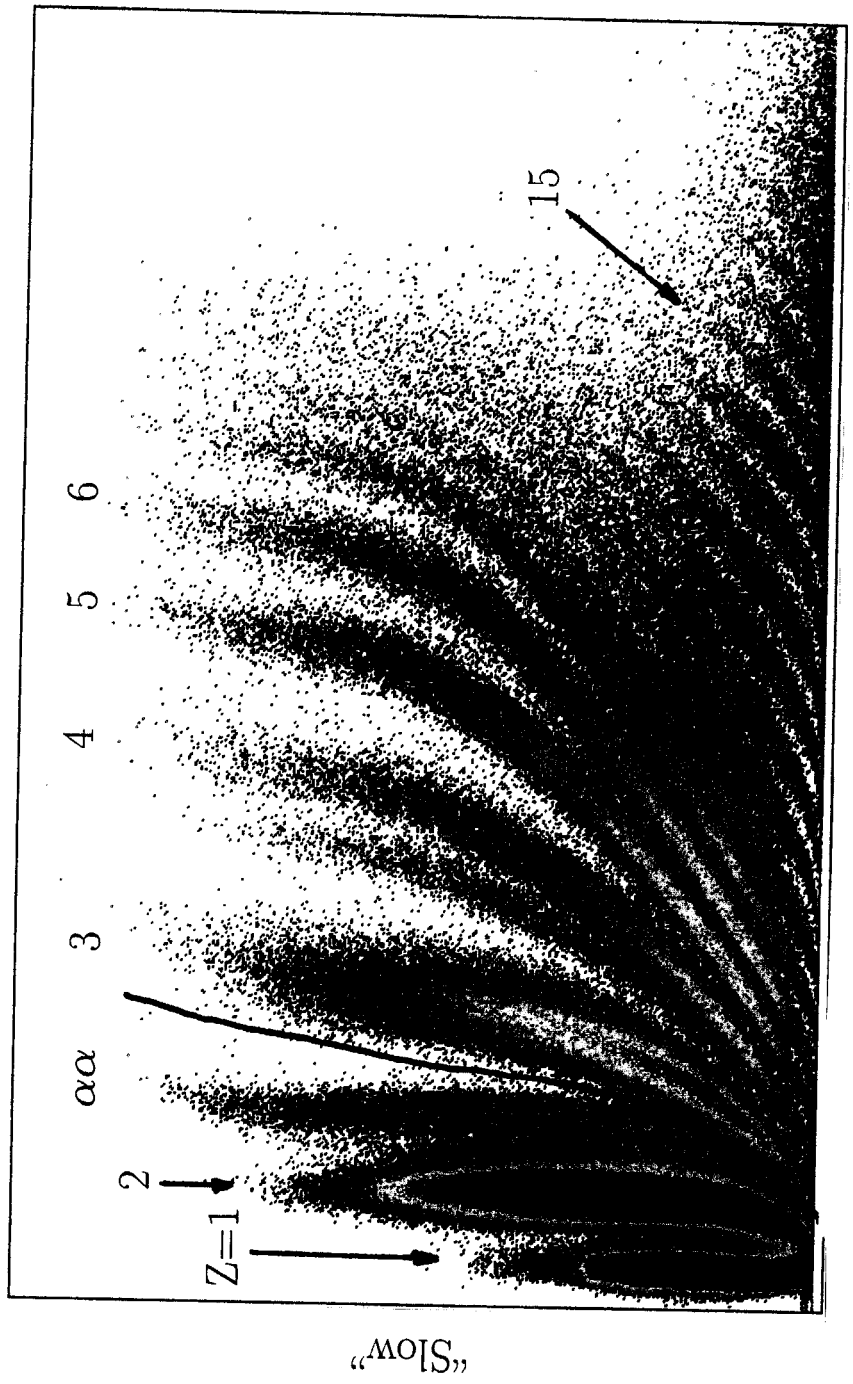

Figure 4.2 "slow" versus fast' spectrum of a Hilger detector(det # 2-9). The solid line is drawn to separate the light charged particles and IMFs for each detector.

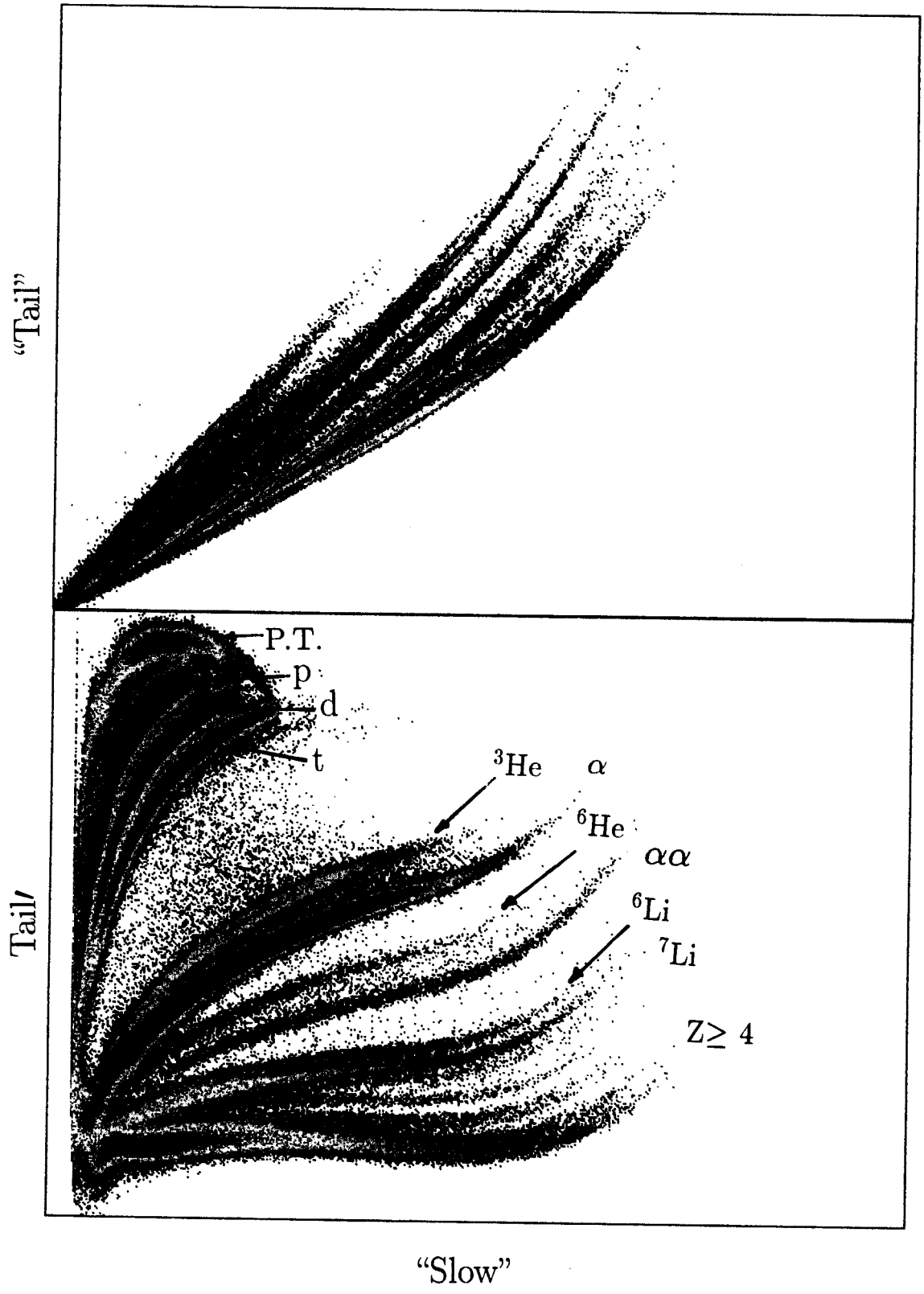

Figure 4.3 "tail"(upper) and tail' (bottom) versus "slow" spectra. The transformation is explained in the text.

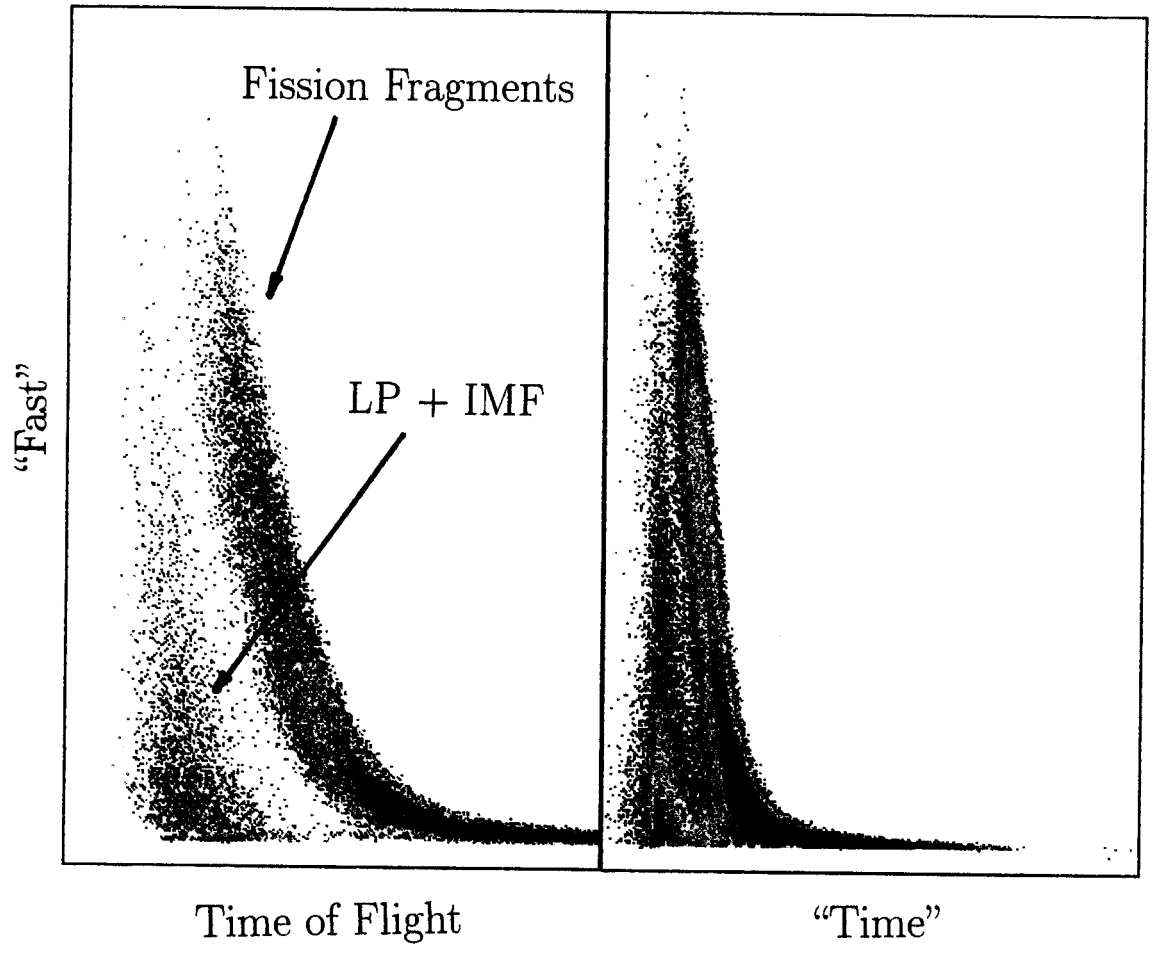

Figure 4.4 "fast" versus time of flight (left) and "time" (right) spectra. Time of flight has been achieved "time"(ns) - "RF"(ns).

isotopes are well separated over the entire energy region up to the punch-through points, and ^{3}He and ^{4}He are well separated except at low energy. The double α lines are well separated from Li, and not included as the intermediate mass fragments. Also there is some separation in the Li and Be isotopes, but as discussed in reference [Ben89] particle identification by pulse shape discrimination using CsI(Tl) at these energies seems to be limited to about $Z \leq 4$.

Low energy particles and fission fragments are stopped in the 4mg/cm^2 thick fast plastic and could not be identified by charge because of the lack of a "slow" signal. However fission fragments which have distinctly slower velocities could be identified in the "fast" versus "time" spectra. The right section in Figure 4.4 shows such "fast" versus "time" spectra for one detector in ring 2. Improved resolution has been achieved using RF timing information. The left section shows the separation of fission fragments from intermediate mass fragments and light charged particles, where x axis is the absolute time of flight in arbitrary units reconstructed from RF time and "time" signal of a detector. Unfortunately RF information was not recorded for all events. Therefore raw detector timing had to be used for identification of fission fragments with slightly worse resolution.

4.2.B Gain drift correction

As discussed in Section 3.8, each ring had a light pulsing system to monitor the gain drifts of the photomultiplier tubes. Unfortunately, for the current experiment, most of the information of the light pulsing system had been lost (except for two runs) because of an error in the data acquisition software. Thererefore we had to monitor gain drifts of the photomultiplier tubes in an alternative way. For this purpose we determined the channel variations of punch-through points which are well defined by the detector geometry. Figure 4.5

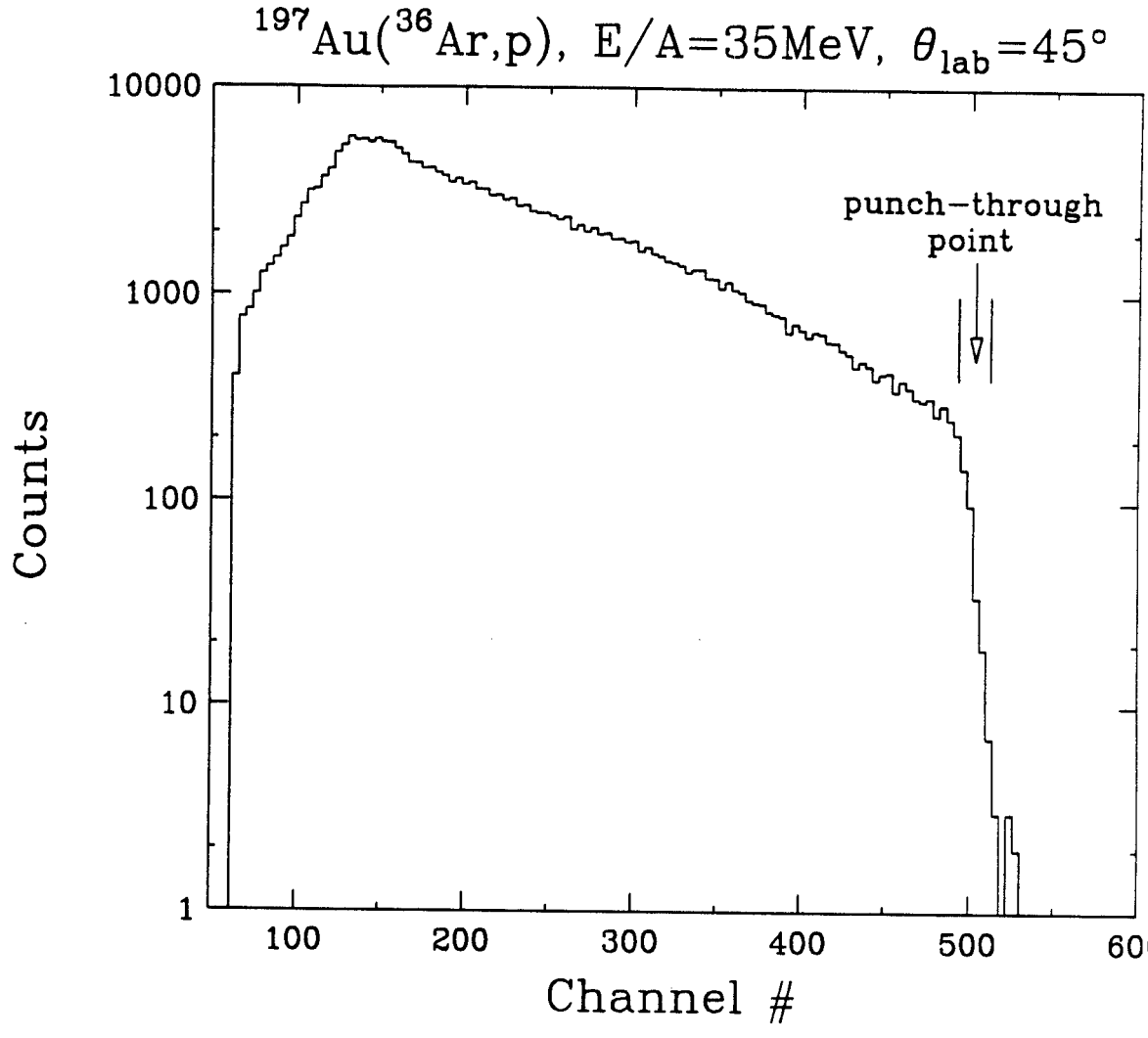

Figure 4.5 Proton punch-through point of one detector in ring 5. Two vertical bars indicate the systematic uncertainty to decide the punch-through points

shows a typical punch-through point of proton spectra. The two vertical bars represent the systematic uncertainty in deciding this point, i.e. start and end points of the rapid fall-off of the cross sectioin. Figure 4.6 shows the correlation of gain drifts determined from both light pulser and punch-through points obtained with the data of two runs for which the light pulser information had been recorded. Both methods of extracting gain drifts agree within 1-2% indicating the validity of the more cumbersome gain drift correction via the punch-through points.

For backward detectors, punch-through points could not be determined. Here we assummed that drifts were linear with time and used light pulser data at the beginning and at the end of the experiment to determine the rate of change. The maximum gain drift of all detectors over whole run was of the order of 4%. Therefore the gain correction was not very significant. This constancy was probably achieved because we allowed for a "warm-up" time before taking data, and because we stabilized the temperature of the apparatus during the experiment.

4.2.C Energy Calibration

(1) method

Energy calibrations were obtained by measuring the elastic scattering of ^{4}He, ^{6}Li, ^{10}B, ^{12}C, ^{16}O and ^{35}Cl beams from a ^{197}Au target at incident energies of E(^{4}He)/A = 4.5, 9.4, 12.9, 16, and 20 MeV; E(^{6}Li)/A = 8.9 MeV; E(^{10}B)/A = 15 MeV; E(^{12}C)/A = 6, 8, 13, and 20 MeV; E(^{16}O)/A = 6, 8, 16, and 20 MeV; and E(^{35}Cl)/A = 8.8, 12.3, and 15 MeV. The limitation of this method is that elastic scattering cross section decreases dramatically for scattering angles larger than the grazing angle of the reaction. Therefore backward detectors did not have significant statistics to allow the extraction of the elastic scattering peaks. To

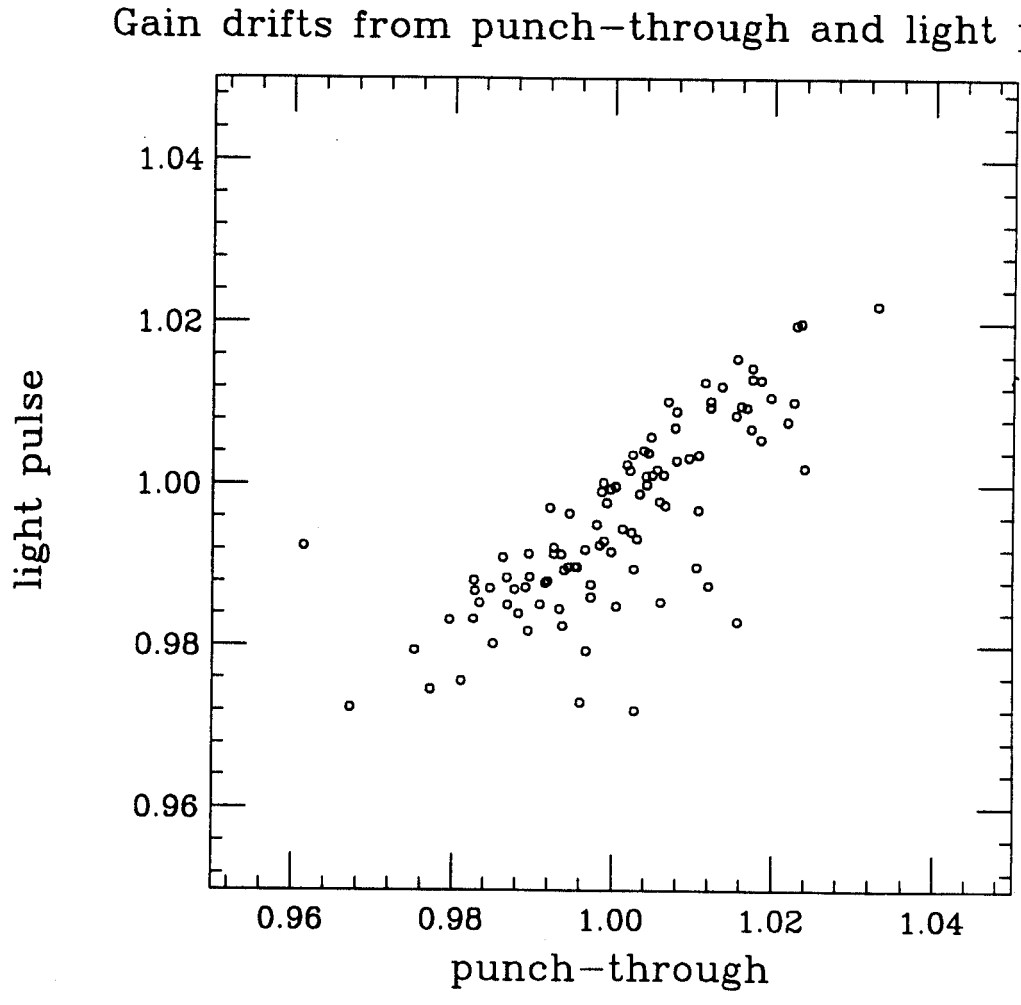

Figure 4.6 The correlation between correction from light pulse information and the correction from punch-through points determined for different detectors.

compensate this limitation we rotated the whole miniball by 180° to expose backward detectors to elastically scattered ^{4}He.

For each elastic scattering peak, we calculated the net energy loss inside the CsI(Tl) crystal by subtracting the energy losses in the absorbers and fast scintillator foils. Then we compared this energy loss with the "slow" ADC conversion which is not contaminated by fast plastic light output and was a measure of the energy loss inside of CsI(Tl) crystal.

(2) Energy response of CsI(Tl)

The light response of CsI(Tl) crystals to various impinging particles has been investigated by several experiments for light charged particles, and heavy ions [Qui59,Gon88,Sto58,Ala86]. The nonlinearity of the light output of CsI(Tl) crystal seems prominent for particles of lower energy and increasing atomic number. At energies above 5-6 MeV/A, the light output seems to be quite linear. As an example, Figure 4.7 shows a calibration achieved by a typical Miniball detector. The x-axis is the net energy loss inside the CsI(Tl) crystal and y-axis is the channel number of "slow" signal. The pedestal had been subtracted. The curves in the Figure 4.7 are fits to the data points with the function,

$$L(E) = aE + b(e^{-cE}-1), \qquad (4.4)$$

where a,b, and c are adjustible parameters, and E is the energy loss in the CsI(Tl) crystal. This functional form is consistent with previous measurements [Qui59,Val90]. It reproduces the nonlinear behavior of the CsI(Tl) light putput in the low energy region and the linear behavior at higher energies.

For the forward rings, ring# 2 and 3, we had enough data points to determine the fit parameters for the individual detectors. We constructed a

reference calibration representing the average calibration points of the detectors in ring 2,3, and 4, and used this average calibration for the more backward detectors. Figure 4.8 shows these reference lines and data points of the detectors in ring 2,3, and 4 normalized at the 80 MeV Carbon point. The variations in the channel numbers for the same energy are largely attributed to the slightly different response functions between detectors due to different thallium dopping. For detectors of ring 4-7, we used these reference lines and one normalization factor to match 1 or 2 data points for each Z line. The spread of the data points in Figure 4.8 would be the main source of uncertainty in the energy calibration of detectors back of ring 4. For the calibration of Z=4,7,9 we interpolated from adjacent low and high Z lines to obtain the calibrations shown in Figure 4.8 as dashed lines. The overall accuracy of this energy calibration of intermediate mass fragments was estimated about 5%. For hydrogen isotopes we used the punch-through energies calculated with the program of refence [Zie85] assuming a linear relation between light output and energy [Gon88].

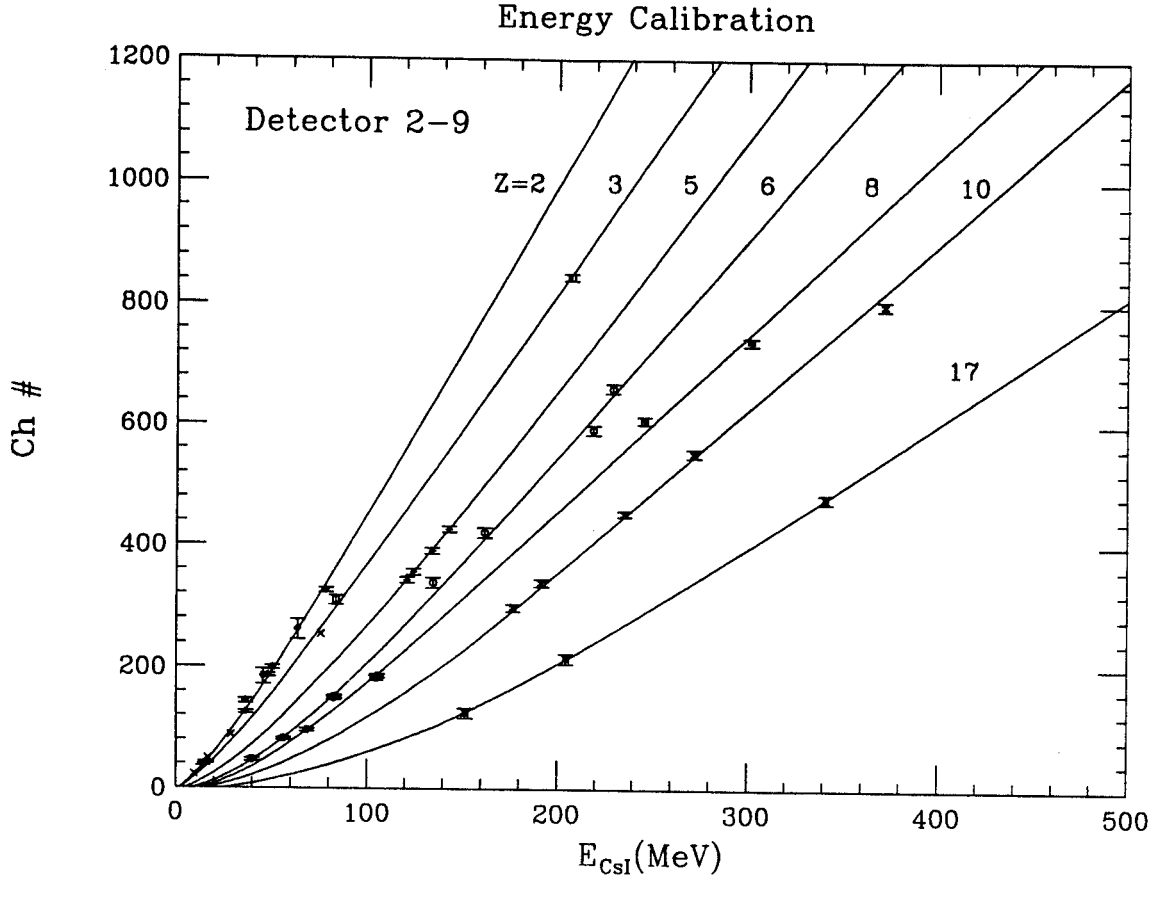

Figure 4.7 Energy calibration of det 2-9 as an example. The points are elasticlly scattered points and the curves are fits with equation 4.4.

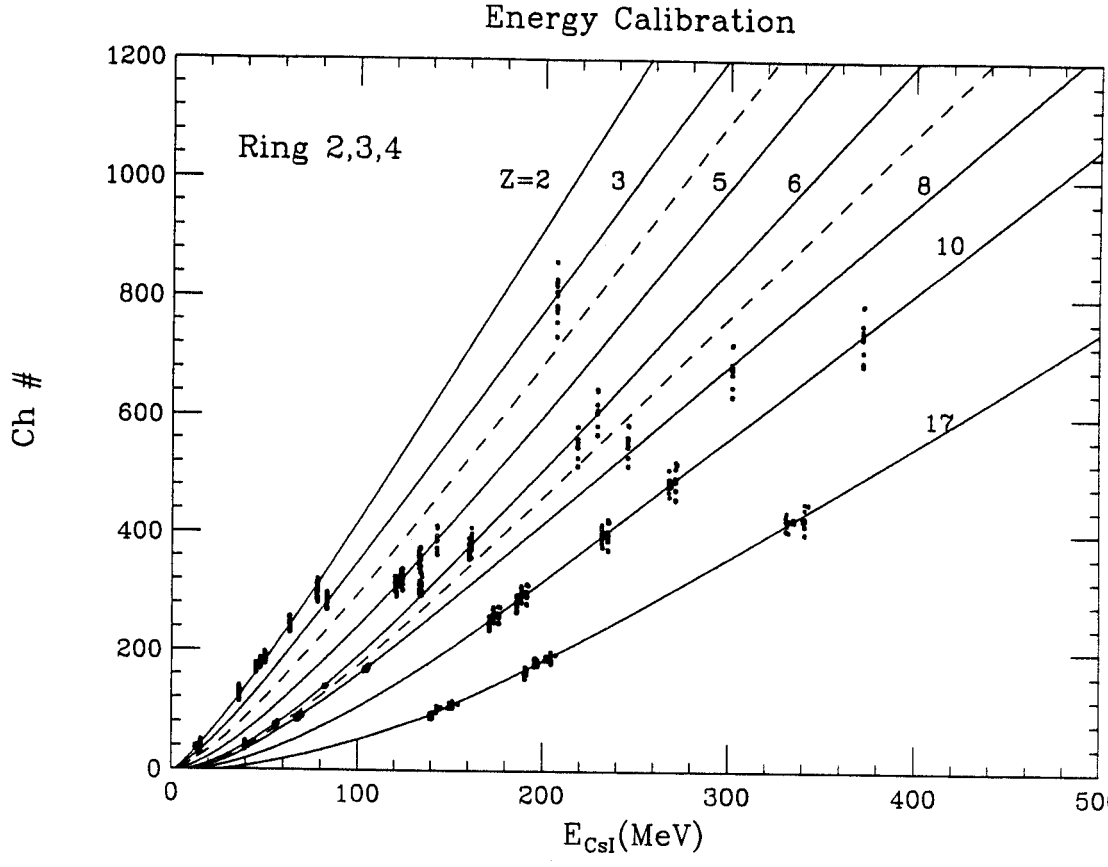

Figure 4.8 Energy calibration of all detectors in ring 2, 3, and 4 to get reference curve. The data points are normalized to detector 2-3 at the 80MeV carbon point.

Chapter 5 General reaction characteristics

5.1 Multiplicity distributions : impact parameter selection

A qualitative perspective of the reaction is depicted by the multiplicity distribution of identified charged particles in Figure 5.1. The threshold at $N_C = 2$ is due to the hardware trigger employed during most of the experiment. To a rough approximation, the charged particle multiplicity is determined by the deposition of energy from relative motion into internal degrees of freedom. Within a simple geometric picture of the collision, this energy deposition depends on the impact parameter of the collision - more central collisions being associated with greater energy deposition and hence larger charged particle multiplicities. At higher bombarding energies [Cav90], cuts on the charged-particle multiplicity are commonly used for the selection of different impact parameter ranges. While a purely geometric interpretation of the measured charged-particle multiplicities may not be strictly applicable at this low energy, it can nevertheless be utilized to generate a rough impact parameter scale. In the bottom part of Figure 5.1, such a scale is constructed by using the geometric prescription of reference [Cav90] in which a monotonic relation between charged-particle multiplicity and impact parameter is assumed:

$$(b/b_{max})^2 = \int_{N_C}^{\infty} (dP(N'_C)/dN'_C)\, dN'_C , \qquad (5.1)$$

here $dP(N_C)/dN_C$ is the normalized probability distribution for the measured charged-particle multiplicity and b_{max} is the maximum impact parameter for

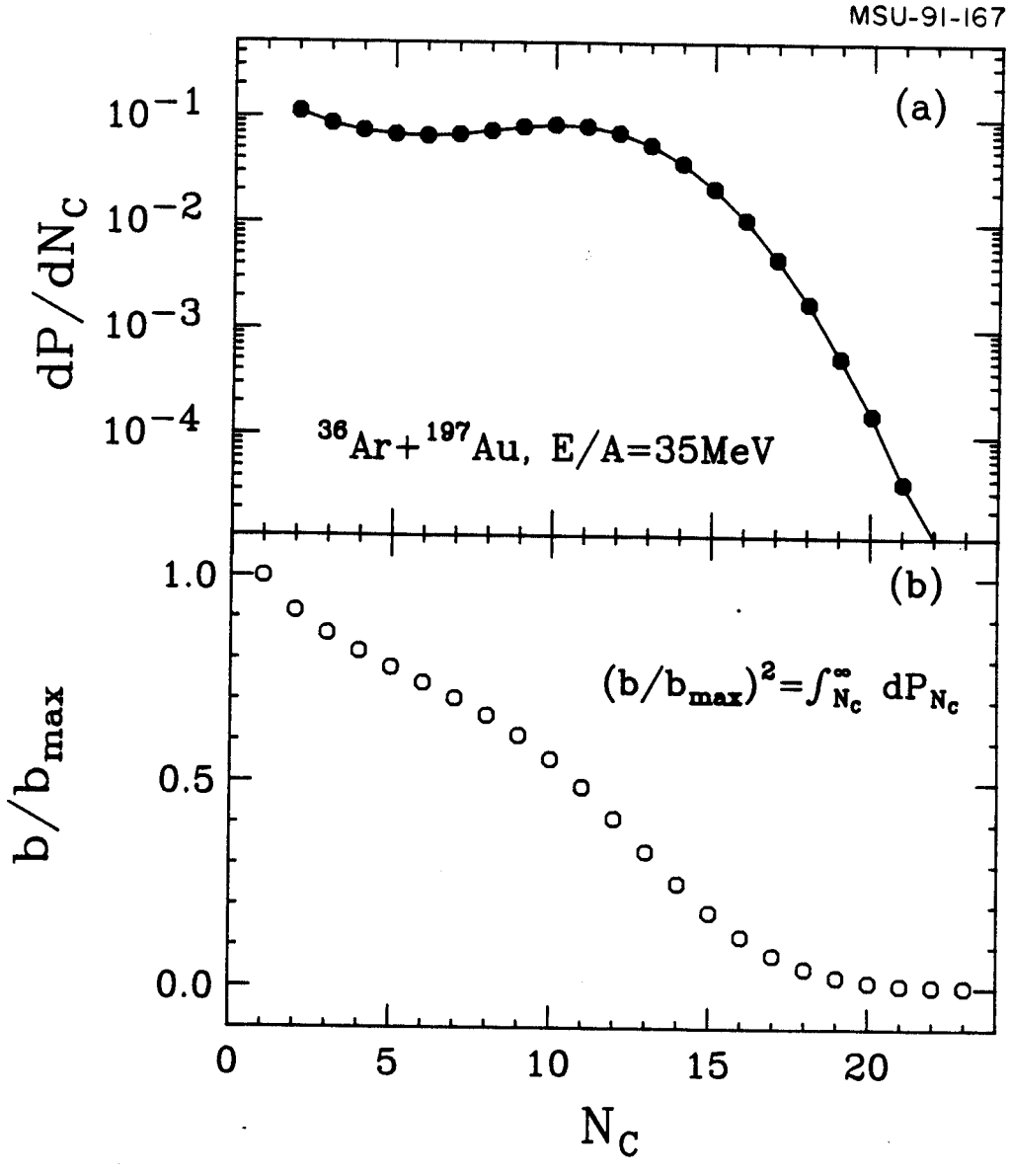

Figure 5.1 Part a: multiplicity distribution of identified charged-particles detected in this experiment; consistent with the hardware trigger of $N_{hit} \geq 2$, a software cut of $N_C \geq 2$ was applied. Part b : relation between charged-particle multiplicity and impact parameter obtained from the geometrical prescription of reference [Cav90].

which particles were detected in the Miniball ($N_C \geq 1$). This relative scale between impact parameter and charged-particle multiplicity must not be over-interpreted since considerable fluctuations of the charged-particle multiplicity must be expected even for collisions of well defined impact parameter. Nevertheless, it appears reasonable to distinguish between "central", "mid-central", and "peripheral" collisions by applying multiplicity cuts corresponding to $N_C \geq 12$, $8 \leq N_C \leq 11$, and $2 \leq N_C \leq 7$, respectively. Events with $N_C=1$ were not included in this definition of peripheral collisions.

Experimental multiplicity distributions for intermediate mass fragments detected in peripheral, mid-central, and central collisions are shown in Figure 5.2. The Poisson-like shape of the IMF distribution is consistent with our previous measurement described in Chapter 2. The "raw" IMF multiplicity is larger in the current measurement with Miniball than the previous measurement by factor of about three, due to lower energy threshold, larger solid angle coverage, and no fission requirement. For peripheral collisions, the IMF multiplicity distribution is peaked at $N_{IMF}=0$ indicating that IMF emission is an improbable outcome. For mid-central collisions, the peak of the IMF multiplicity distribution is at $N_{IMF}= 1$. For these collisions, IMF emission is a common process and multiple IMF emission occurs fairly frequently. For central collisions, the IMF multiplicity distribution does not change dramatically from the mid-central distribution. The IMF distribution is still peaked at $N_{IMF}=1$, but the probabilities for multiple IMF emission ($N_{IMF}= 3\text{-}7$) increase in probability by factors of 2-10.

The dependence of the mean IMF multiplicity $\langle N_{IMF} \rangle$ on the charged-particle multiplicity N_C is depicted in Figure 5.3. Over a broad range of charged-particle multiplicities N_C, the mean IMF multiplicity $\langle N_{IMF} \rangle$ exhibits an approximately linear rise as a function of N_C. For very high multiplicities, $N_C \gtrsim 12$, the mean IMF multiplicity levels off as a function of N_C and reaches an

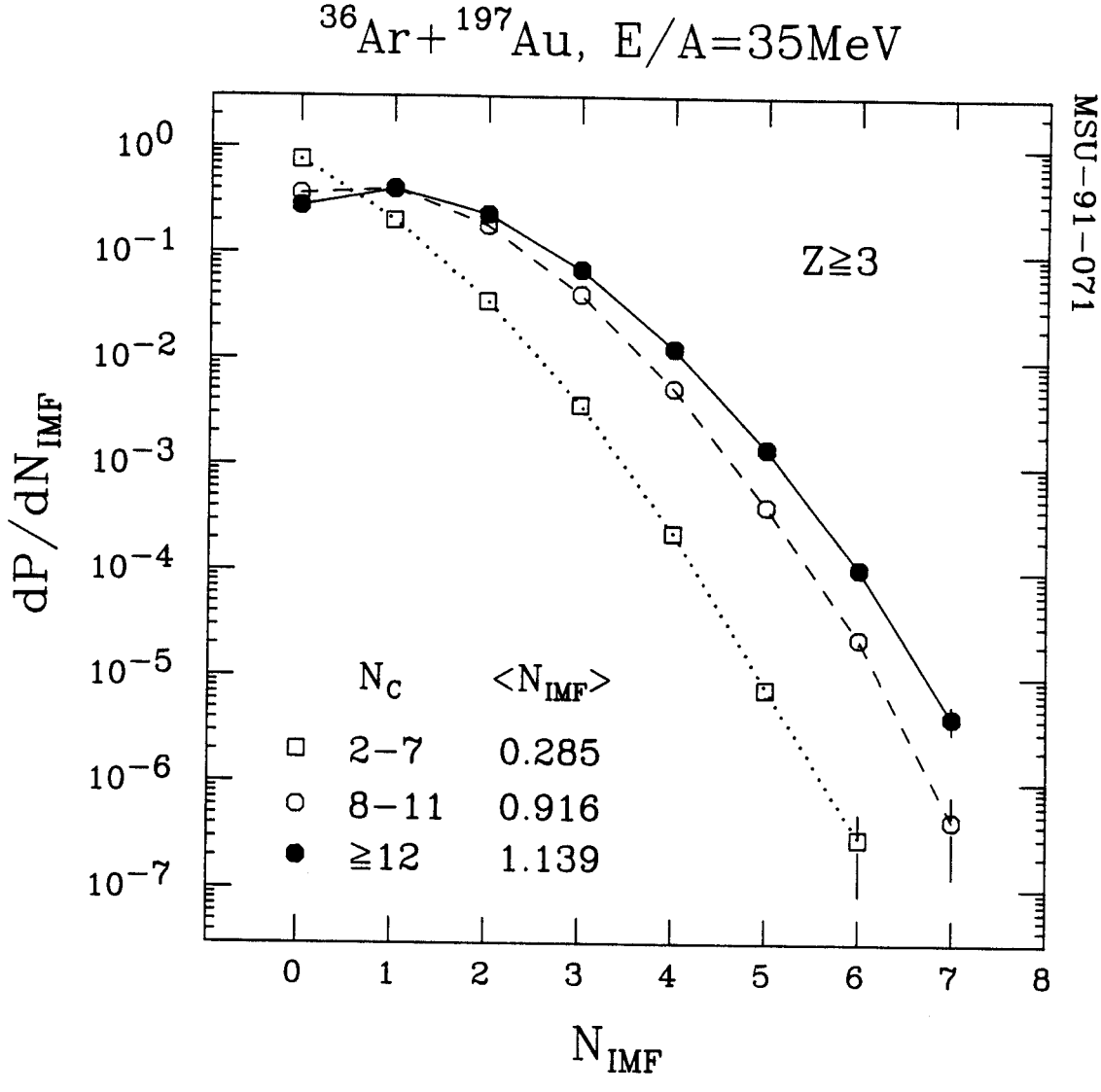

Figure 5.2 Normalized conditional probability distributions dP/dN_{IMF} of detecting N_{IMF} intermediate mass fragments in collisions preselected by the indicated gates on charged-particle multiplicity N_C. Mean values $\langle N_{IMF} \rangle$ are given in the figure.

asymptotic value of $\langle N_{IMF} \rangle \approx 1.2$. To determine whether this behavior is dominated by the inclusion of Li fragments in our definition of IMFs, we have explored the dependence of the mean IMF multiplicity $\langle N_{IMF} \rangle$ on the charged-particle multiplicity N_C when an IMF is redefined to exclude Li fragments ($4 \leq Z \leq 20$). Qualitatively, the dependence of mean IMF multiplicity on charged particle multiplicity exhibits a similar trend, irrespective of the inclusion of Li fragments in the definition of IMF.

The relationship between the IMF and total charged particle multiplicities can be qualitatively understood by assuming that the charged particle multiplicity is strongly correlated with energy deposition and that the production of intermediate mass fragments depends primarily upon this energy deposition. The observed rise of $\langle N_{IMF} \rangle$ as a function of N_C can thus be viewed as due to the selection of interactions involving progressively larger amounts of internal energy deposition. In the extreme tails of the N_C distributions, however, the correlation between internal energy and N_C becomes dominated by fluctuations of the charged particle multiplicity. Hence, very large values of N_C become ineffective in selecting nuclei of increasing internal energy, thus causing the observed saturation of $\langle N_{IMF} \rangle$ at large values of N_C. This loss of selectivity for $N_C \gtrsim 12$ is also expected from the impact parameter scale provided in Figure 5.1b.

In order to explore whether the detection of intermediate mass fragments can provide impact parameter selectivity, we investigated the dependence of the charged particle multiplicity distribution on the IMF multiplicity and on the detection angle of the IMF. The left panel of Figure 5.4 shows the correlation between IMF multiplicity and associated charged particle multiplicity. Such a relationship is qualitatively similar to the data discussed in Chapter 2 for reactions contributing to the fission channel. Events without an IMF are dominated by peripheral (low charged particle multiplicity) reactions.

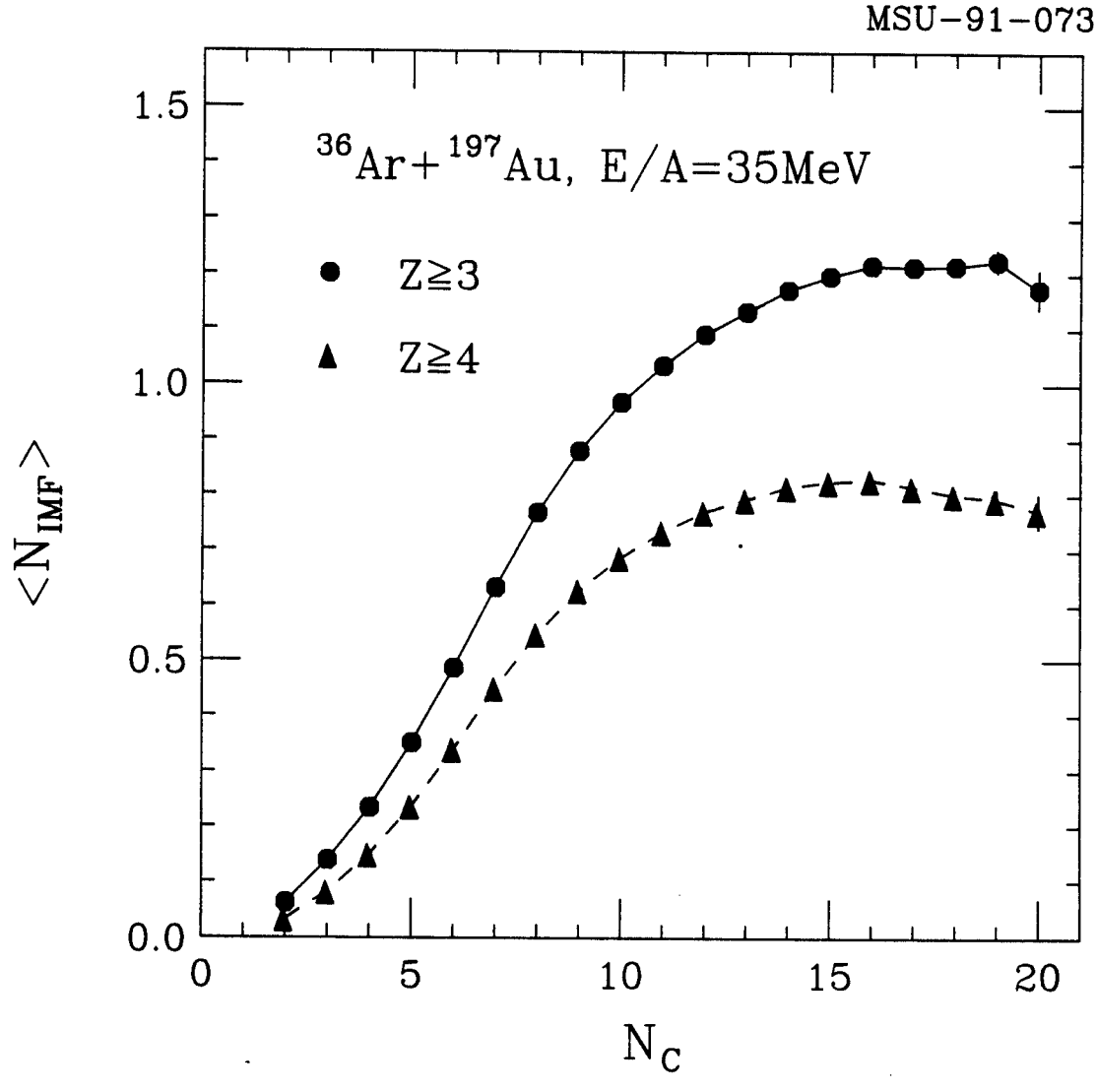

Figure 5.3 Mean IMF multiplicity $\langle N_{IMF} \rangle$ (circular points) as a function of the charged-particle multiplicity N_C. Triangular points show mean multiplicities when lithium nuclei are excluded from the definition of IMFs.

Requirement of one intermediate mass fragment substantially suppresses contributions from peripheral processes. The dependence of the charged particle multiplicity on the detection angle of the IMF is shown in the right hand panel of Figure 5.4. In all cases, IMF emission selects violent collisions characterized by large charged-particle multiplicities. While a slight shift in the charged-particle multiplicity distribution to lower multiplicities is observed when fragments are detected at $16^\circ \leq \theta_{lab} \leq 23^\circ$, the angular sensitivity of the charged-particle multiplicity distributions to the fragment detection angle is insignificant at larger angles.

5.2 IMF elemental distributions

Examples of elemental distributions, integrated over the angular range of $16^\circ \leq \theta_{lab} \leq 120^\circ$, are shown in Figure 5.5. Solid points show the inclusive ($N_C \geq 2$) distributions; open squares and open circles show distributions measured for the peripheral ($2 \leq N_C \leq 7$) and central ($N_C \geq 12$) gates on charged-particle multiplicity, respectively. (To facilitate the comparison of relative shapes, the distributions were renormalized). All three elemental distributions exhibit near exponential shapes. Examples of fits with exponential functions, $e^{-\alpha Z}$, are shown by the solid and dashed curves for the parameters given in the figure; the indicated errors are estimates of the systematic uncertainties arising from the fact that the elemental distributions do not strictly follow exponential shapes.

The elemental distribution measured for the peripheral gate exhibits a slightly steeper slope than that measured for the central gate. However, the inclusive distribution is very similar in shape to that observed in central collisions. This similarity is related to the fact that IMF emission is strongly suppressed for peripheral collisions which, hence, make only minor

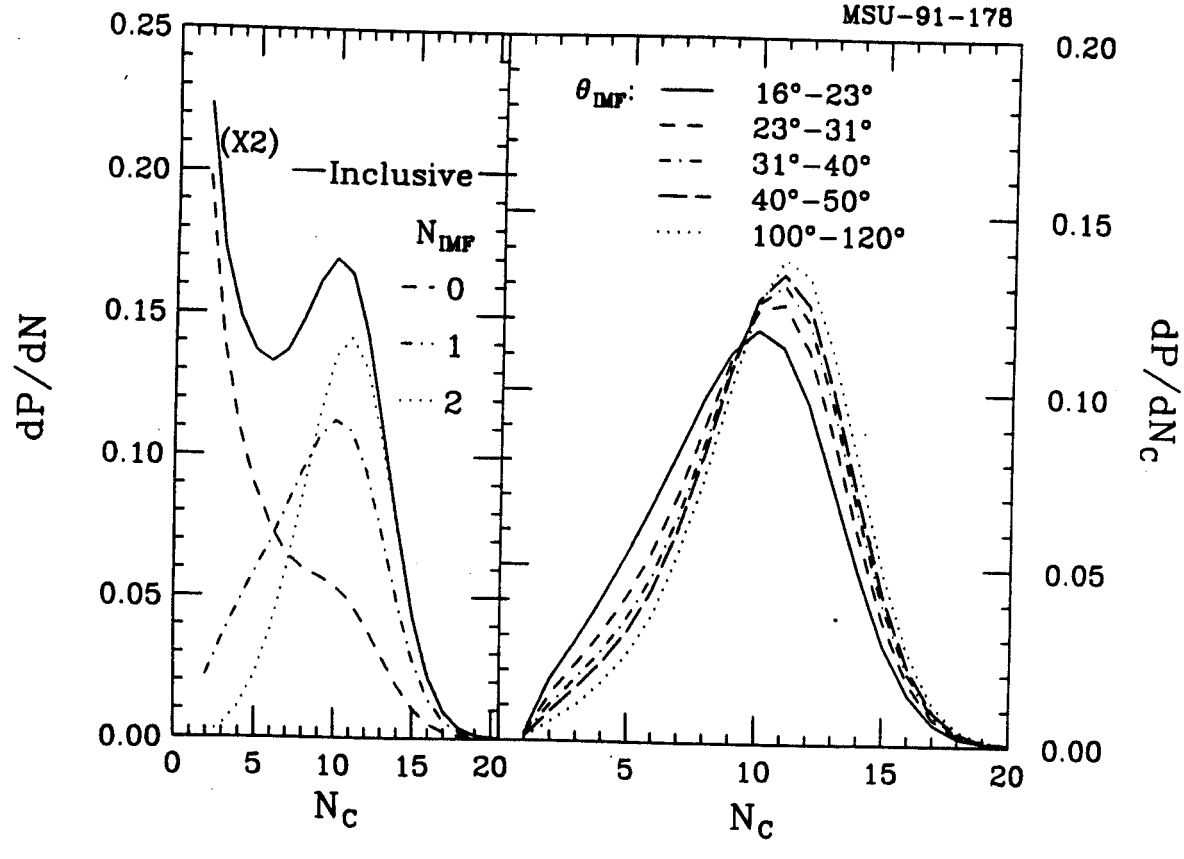

Figure 5.4 Charged-particle multiplicity distributions dP/dN_C measured for collisions preselected by the detection of N_{IMF}=0, 1, and 2 intermediate mass fragments at any angle (left hand panel) and by the detection of a fragment at a given angle (right hand panel).

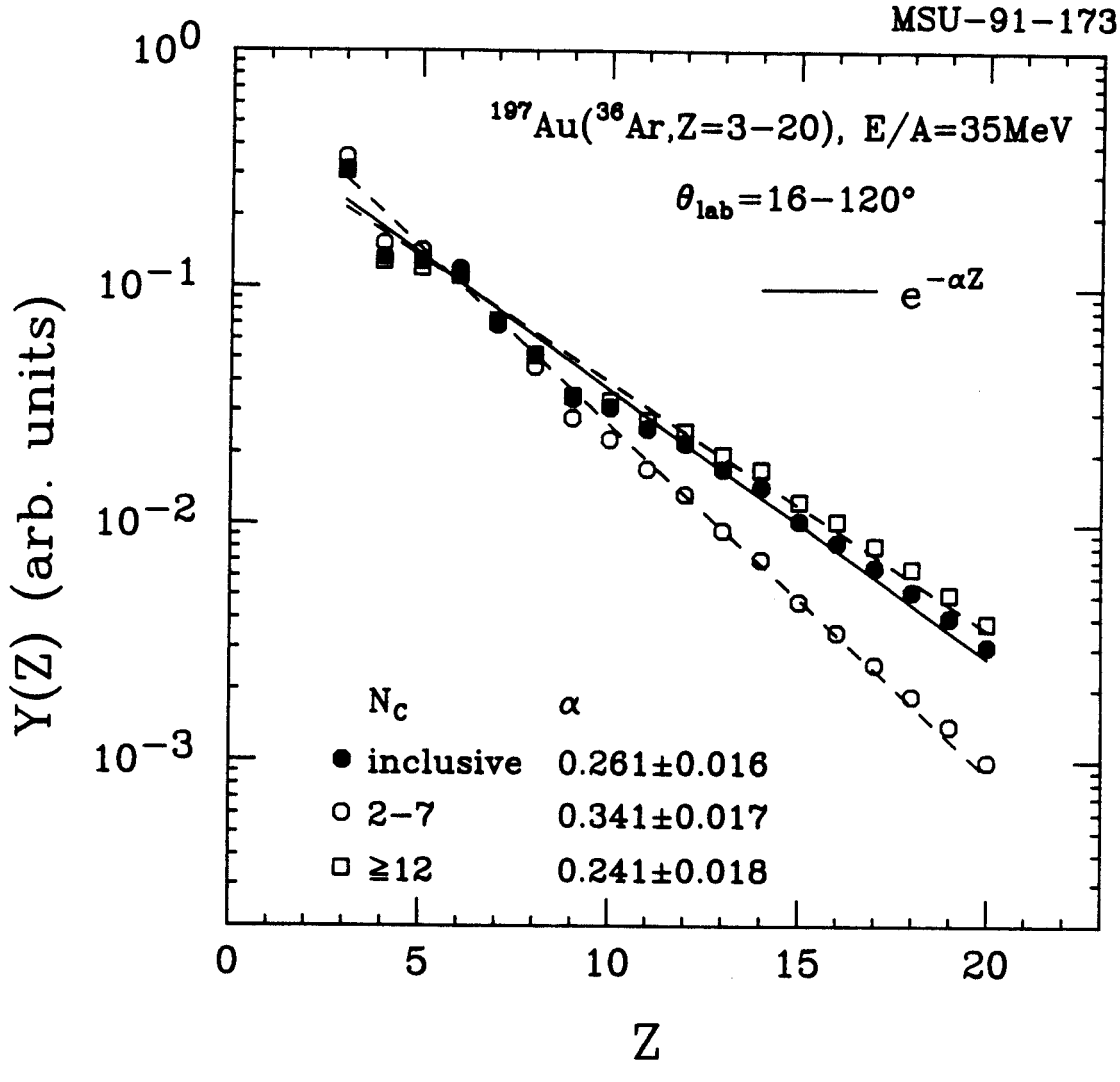

Figure 5.5 Comparison of angle integrated element distributions measured inclusively (solid points), in central collisions ($N_C \geq 12$: open squares), and in peripheral collisions ($2 \leq N_C \leq 7$: open circles). The lines represent parametrizations with exponential functions; ranges of parameters consistent with charge distributions are indicated.

contributions to the inclusive cross section. Inclusive mass or charge distributions may not always be quite as meaningless as suggested previously [Aic88a,Aic88b,Pei89].

The parameters α describing elemental distributions gated by different IMF multiplicities are shown in the left hand panel of Figure 5.6. While the shapes of the elemental distributions are not very sensitive to the IMF multiplicity, there is a discernible trend for the elemental distributions to become slightly steeper as more fragments are emitted.

We cannot offer a quantitative explanation of the dependence of α on N_C. However some of the qualitative trends are consistent with statistical considerations. Within a statistical picture of fragment emission, the slope of the charge distribution is expected to become less steep when the temperature of the emitting system is raised and Coulomb barrier effects are reduced. As increasing values of N_C are related to higher internal energies of the emitting system, the qualitative trend of reduced slopes in the elemental distributions is expected. However, the increase at very large values of N_C is not, and its origin remains less clear. It could be related to self-correlations imposed by energy conservation. Gates on the extreme tails of the charged-particle multiplicity distributions select events in which statistical fluctuations have lead to the emission of more charged particles than average. If intermediate mass fragments are emitted at the later stages of the reaction, the fragment emitting system will then have a slightly reduced excitation energy, and the slope of the resulting fragment distribution should be slightly steeper.

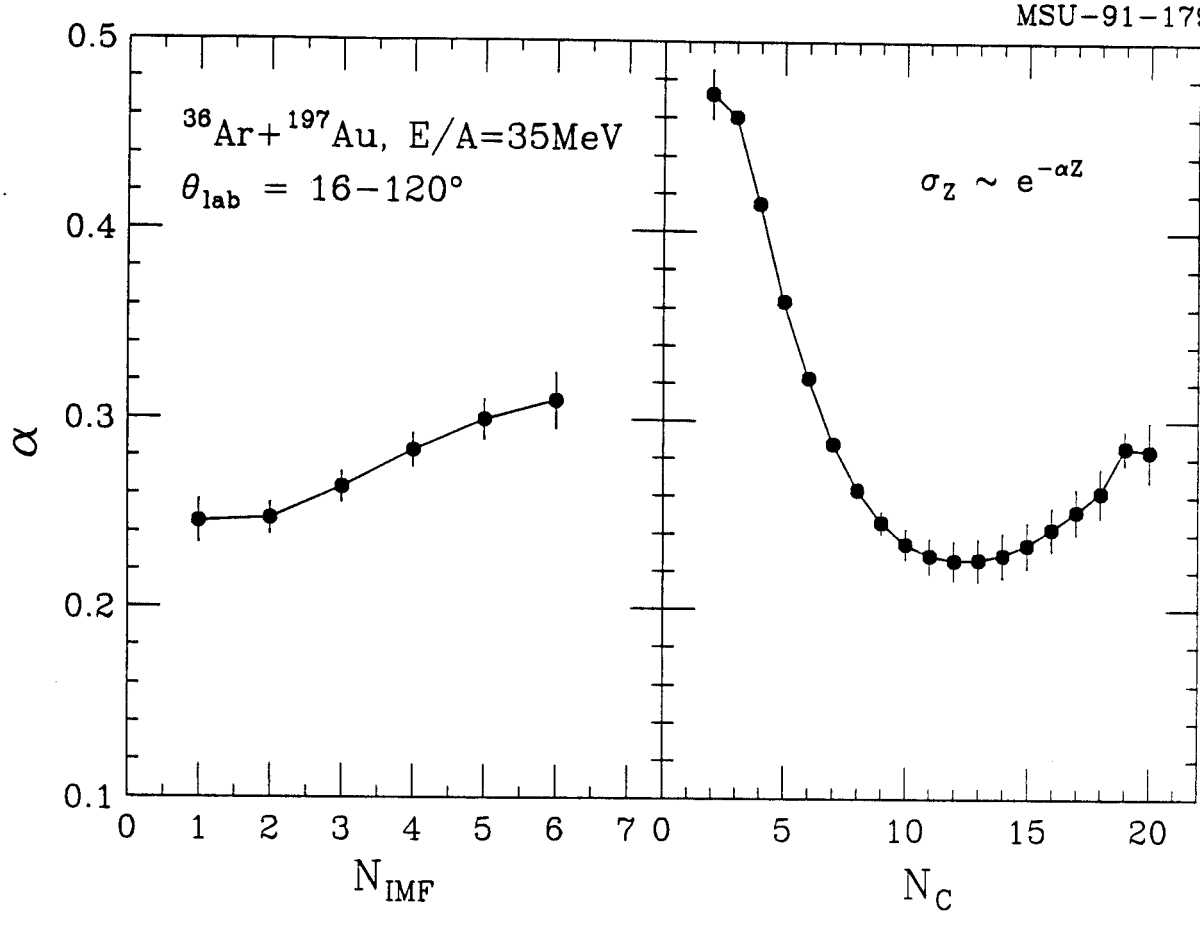

Figure 5.6 Parameters of exponential ($e^{-\alpha Z}$) fits to element distributions selected by cuts on N_{IMF} (left panel) and N_C (right panel).

5.3 Angular distributions

Angular distributions of representative intermediate mass fragments, gated by peripheral ($2 \leq N_C \leq 7$: open circular points) and central ($N_C \geq 12$: open square shaped points) collisions, are shown in Figure 5.7. For comparison, inclusive angular distributions are depicted by solid points. The angular distributions shown in the figure are normalized as conditional probability distributions, i.e. as the probability per unit solid angle to detect a given fragment in collisions preselected by the indicated gate on charged-particle multiplicity. In general, the angular distributions become more forward peaked for increasing fragment charge. The slopes of the angular distributions are steeper for peripheral collisions than for central collisions which could indicate increasing degrees of equilibration and possibly diminishing contributions from projectile-like sources for collisions with larger charged-particle multiplicities.

5.4 Energy spectra

Examples of inclusive energy spectra are presented in Figure 5.8 for intermediate mass fragments of charge Z=4-9. The energy spectra exhibit qualitative characteristics already observed in other heavy-ion induced reactions at comparable energies [Lyn87,FieJ86,FieE89]. In order to provide a reasonable analytic parametrization of these cross sections we have fitted them with a simple parametrization allowing for contributions from three sources of different velocities. Each source was assumed to emit particles with a $1/\sin\theta$ angular distribution in its respective rest frame. The explicit form of the adopted parametrization is taken from reference [Chi86]:

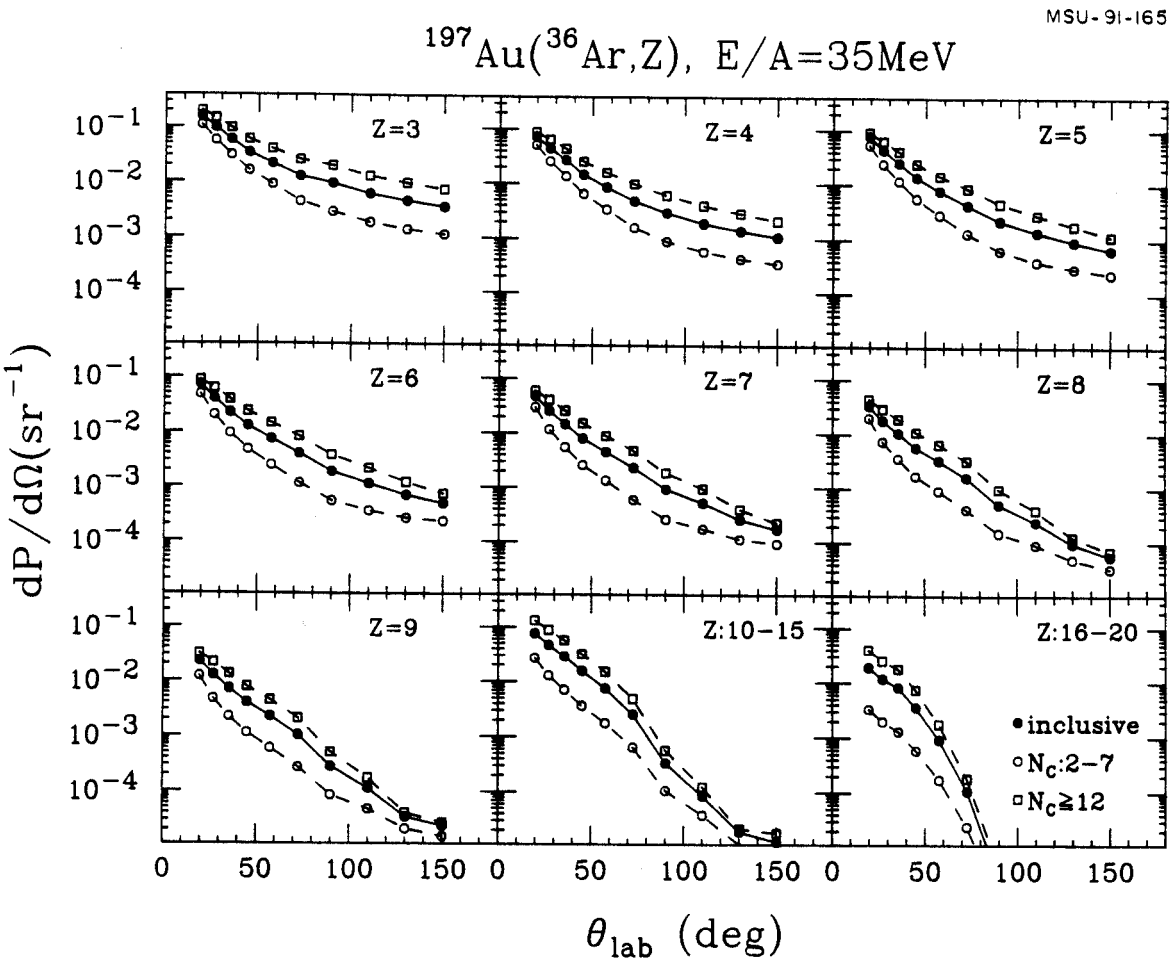

Figure 5.7 Comparison of IMF angular distributions measured inclusively (solid points), in central collisions ($N_C \geq 12$: open squares), and in peripheral collisions ($2 \leq N_C \leq 7$: open circles). Different panels show distributions for the indicated fragment Z. The distributions represent normalized conditional probability distributions for collisions preselected by the indicated gates on N_C.

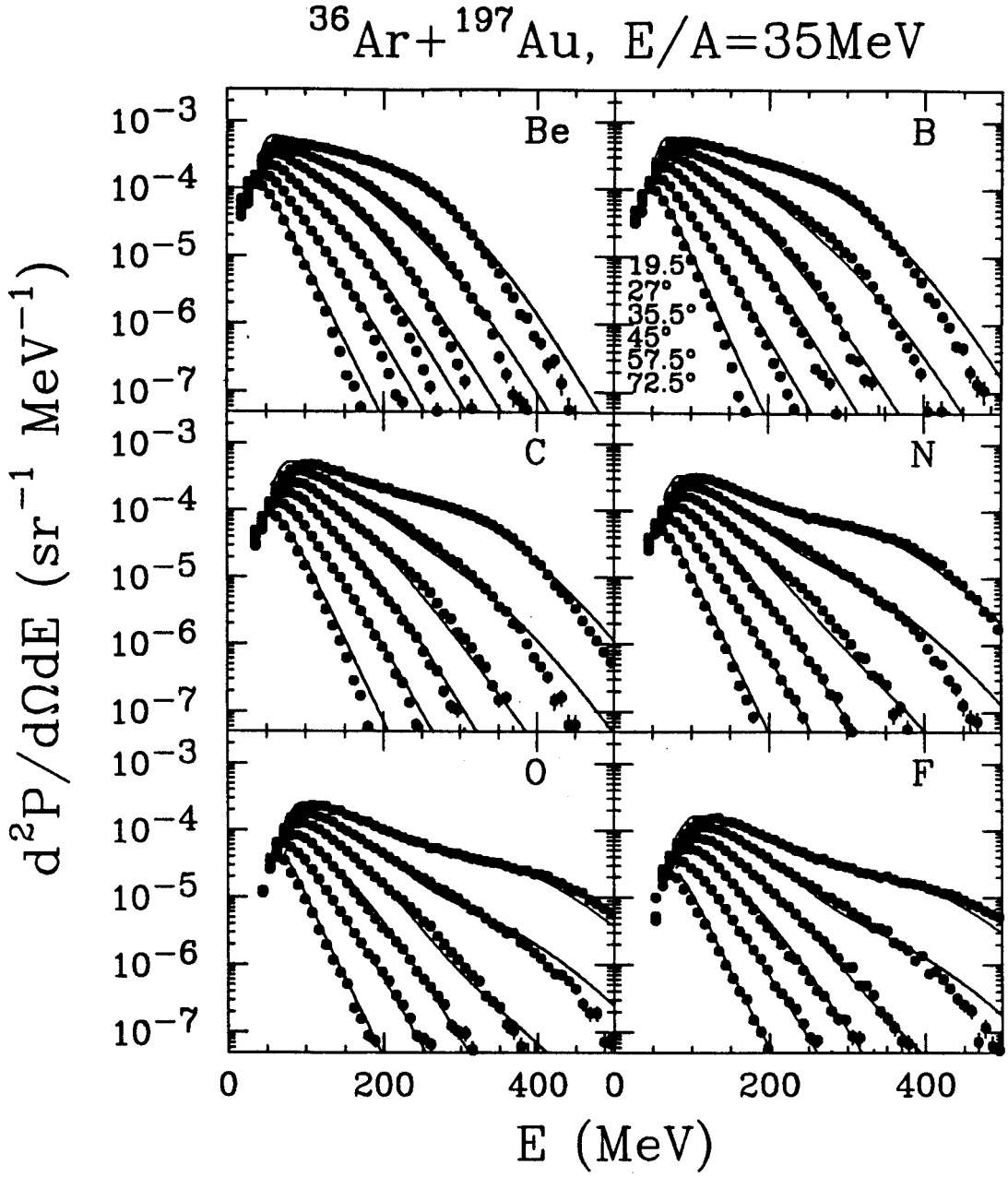

Figure 5.8 Inclusive energy spectra for intermediate mass fragment of charge Z=4-9. The curves represent moving source fits, Eqs. 5.2-4, with the parameters given in Table 5.1.

$$\frac{d^2P}{dEd\Omega} = \sum_{i=1}^{n} N_i(\sqrt{E_{si}}/\sin\theta)\exp(-E_{si}/T_i) \ , \qquad (5.2)$$

where

$$E_{si} = E - V_C + E_i - 2\sqrt{E_i(E-V_C)}\cos\theta \qquad (5.3)$$

and

$$E_i = \frac{1}{2}mv_i^2 \ . \qquad (5.4)$$

Here, T_i is a kinetic temperature parameter characterizing the slope of the energy spectrum for the i-th source, and v_i is the source velocity. The parameter V_C is introduced to account for Coulomb repulsion from a heavy charge assumed, for simplicity, at rest in the laboratory system. To simulate the kinematics of fragment emission from equilibrated residues formed in an incomplete fusion reaction, the velocity of one source was fixed at v_2=0.035c. This value corresponds to a linear momentum transfer of 80%, consistent with the systematics of references [Fat85,Cas89]. The fits are shown by the solid curves in Figure 5.8, and the parameters are listed in Table 5.1. The fitted parameters may not be unique, since they depend on the specific parametrization adopted and, in addition, on the energy and angular range included in the fit [Wil91]. Nevertheless, the fits strongly suggest contributions from fusion-like and projectile-like sources (i=2 and 3, respectively) as well as from an intermediate velocity source (i=1) representing nonequilibrium processes.

Rather large differences are observed in the shapes of energy spectra gated by different ranges of impact parameters. For illustration, Figure 5.9 presents the energy distributions measured for carbon fragments produced in peripheral ($2 \le N_C \le 7$: solid circular points), mid-central ($8 \le N_C \le 11$: open points), and central ($N_C \ge 12$: solid triangular points) collisions. As before, the distributions represent

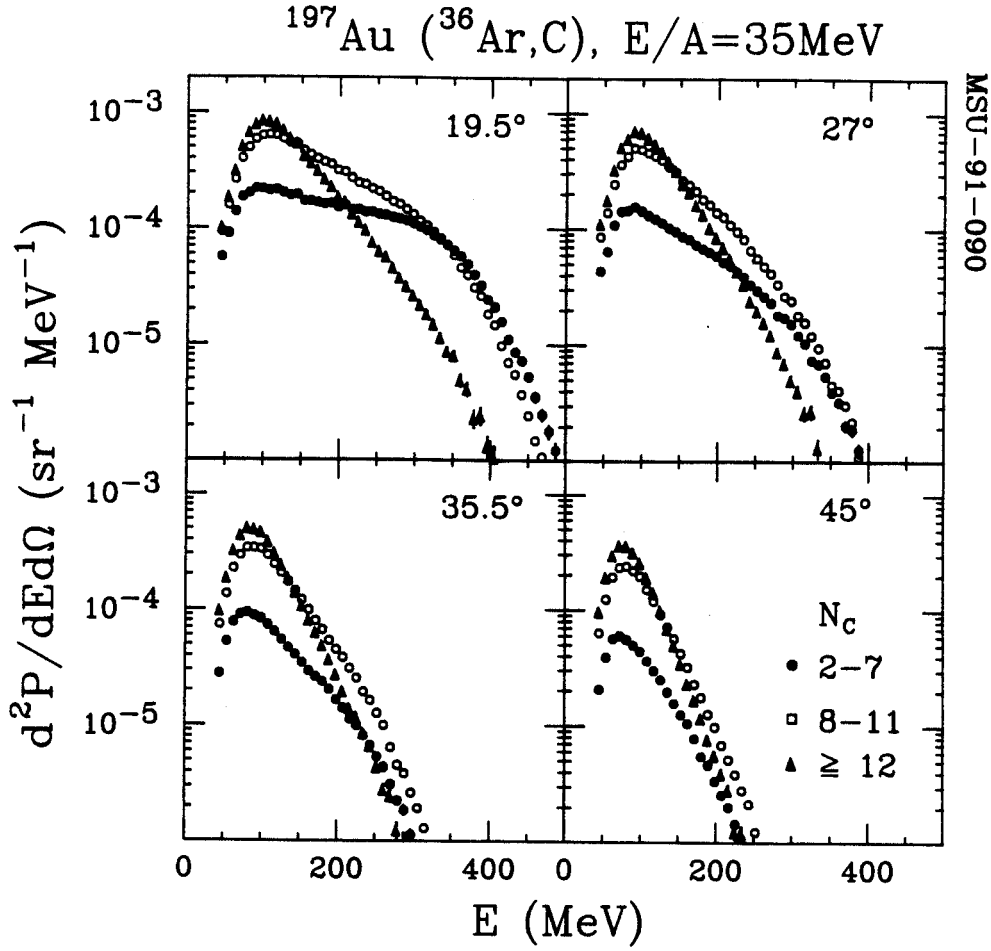

Figure 5.9 Energy distributions of carbon fragments produced in peripheral ($2 \le N_C \le 7$: solid circular points), mid-central ($8 \le N_C \le 11$: open points), and central ($N_C \ge 12$: solid triangular points) collisions. The fragment detection angles are indicated in the individual panels. The distributions represent conditional probability distributions per unit energy and solid angle for detecting a given fragment in collisions preselected by the indicated gate on N_C.

Table 5.1 Parameters of three-source fits (Eqs. 5.2-4, using n=3) to inclusive fragment spectra. The normalization constants N_i are given in units of $10^{-4}/(sr \cdot MeV^{3/2})$.

Z	N_1	v_1/c	T_1(MeV)	N_2	v_2/c	T_2(MeV)	N_3	v_3/c	T_3(MeV)
4	0.748	0.107	15.3	0.516	0.035	11.4	0.734	0.196	9.2
5	0.793	0.108	14.8	0.526	0.035	11.4	0.896	0.200	9.4
6	0.712	0.096	14.9	0.378	0.035	12.6	0.739	0.194	10.4
7	0.521	0.085	14.1	0.223	0.035	9.9	0.375	0.183	11.8
8	0.349	0.078	14.1	0.231	0.035	8.8	0.223	0.170	12.6
9	0.231	0.078	14.8	0.123	0.035	10.6	0.148	0.170	12.3

Table 5.2 Parameters of two-source fits (Eqs. 5.2-4, using n=2) to fragment spectra observed in central collisions ($N_C \geq 12$). The normalization constants N_i are given in units of $10^{-4}/(sr \cdot MeV^{3/2})$.

Z	N_1	v_1/c	T_1(MeV)	N_2	v_2/c	T_2(MeV)
4	1.195	0.111	13.8	1.333	0.035	11.4
5	1.306	0.109	13.3	1.226	0.035	11.4
6	1.207	0.096	13.6	0.923	0.035	12.6
7	0.900	0.085	13.3	0.591	0.035	10.1
8	0.620	0.077	13.2	0.533	0.035	9.1
9	0.437	0.077	13.6	0.276	0.035	10.7

conditional probability distributions per unit energy and solid angle for detecting a given fragment in collisions preselected by the indicated gate on N_C. Consistent with Figure 5.2, the fragment emission probabilities are smaller in magnitude for peripheral than for central collisions. For central collisions, the energy spectra exhibit rather featureless exponential slopes which become steeper at larger emission angles. For peripheral collisions, the energy spectrum at Θ_{lab}=19.5° exhibits a large high-energy shoulder, indicating possible contributions from the decay of projectile-like residues or from strongly damped collisions. Mid-central collisions exhibit an intermediate behavior. At larger angles, this shoulder vanishes, and the energy spectra attain structureless exponential shapes. However, the slopes of the energy spectra observed in peripheral collisions are less steep than the slopes of the energy spectra measured for central collisions.

The exponential shapes of the energy spectra observed in central collisions suggest emission from a system characterized by a relatively high degree of equilibration. In order to explore whether fragment production in central collisions is consistent with emission from fully equilibrated reaction residues formed in fusion-like processes, we have fitted the differential emission probabilities with a two-source parametrization allowing for contributions from a fusion-like source and an intermediate velocity source, each parameterized according to Equations 5.2-5.4 (using n=2). Figure 5.10 shows energy spectra and two-source fits for fragments with $4 \le Z \le 9$ observed in central collisions ($N_C \ge 12$); parameters are listed in Table 5.3. The fits indicate significant contributions from nonequilibrium emission processes.

To give an overall qualitative perspective of the ratio of equilibrium to non-equilibrium emission in central collisions, we show in Figure 5.11 the equilibrium fraction, $\sigma_{slow}/\sigma_{total}$, indicated by the fits in Figure 5.10. Here,

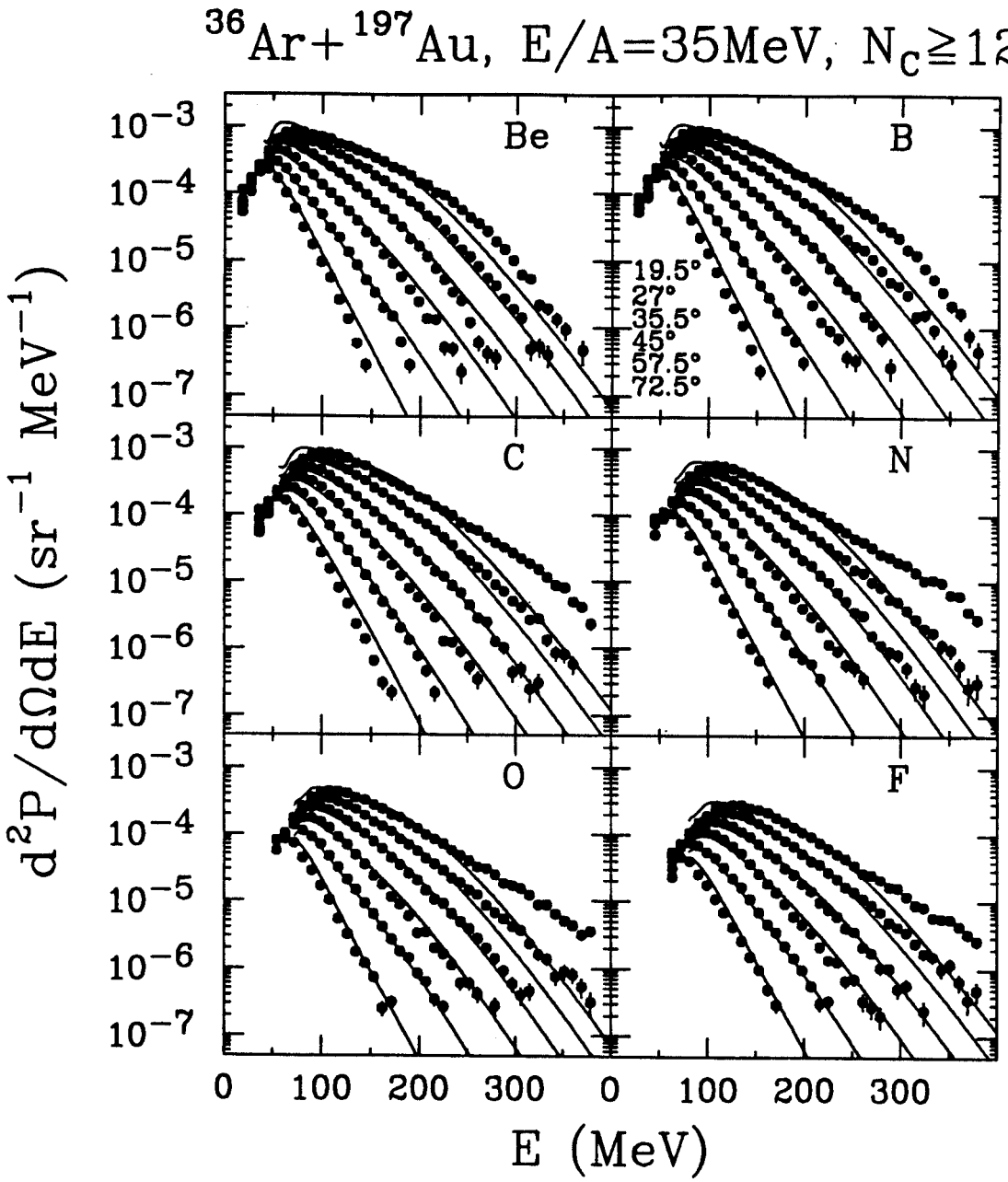

Figure 5.10 Energy spectra for intermediate mass fragments of charge Z=4-9 detected in central collisions ($N_C \geq 12$). The curves represent moving source fits, Eqs. 5.2-4, with the parameters given in Table 5.2. The distributions represent conditional probability distributions per unit energy and solid angle.

σ_{slow} represents the cross section represented by the slow fusion-like source (i=2) and σ_{total} represents the summed cross section from the two sources (i=1+2). The top panel depicts the equilibrium fraction as a function of laboratory angle with the individual source contributions integrated over the energy spectrum above the detection threshold. The bottom panel shows this fraction as a function of fragment momentum per nucleon with the individual source contributions integrated over the angular range of $16^\circ \leq \theta_{lab} \leq 31^\circ$. While the decomposition into equilibrium and nonequilibrium processes may not be unique, the extracted ratios should, nevertheless, provide a qualitative estimate of the fraction which may be emitted by an equilibrated heavy residue. Nonequilibrium contributions are most important at forward angles and for fragments emitted with high kinetic energy. At larger angles, the fragment cross sections are increasingly consistent with emission from equilibrium decays.

Because of the finite energy threshold, the true IMF multiplicity should be higher than the observed multiplicity. In order to estimate the order of magnitude of this differences we have proceeded as follows. Figure 5.12 shows the extrapolations made on the energy spectra for central collisions at three different angles in the laboratory coordinate. As shown in the figure we extrapolated the energy spectra to zero energy by fitting the lower part of the Coulomb bump when the energy spectra show explicit Coulomb bumps or by assuming flat energy distributions when the energy spectra do not show explicit Coulomb bumps. This way we get the approximate uncertainties in cross section below the detection threshold. This rough estimate shows about 10% increase in mean IMF multiplicity for peripheral collision, 15% increase for mid-central collision, and 19% increase for central collision. The uncertainty caused by the finite angle coverage is estimated by extrapolating the angular distribution $\frac{d\sigma}{d\theta}$ to

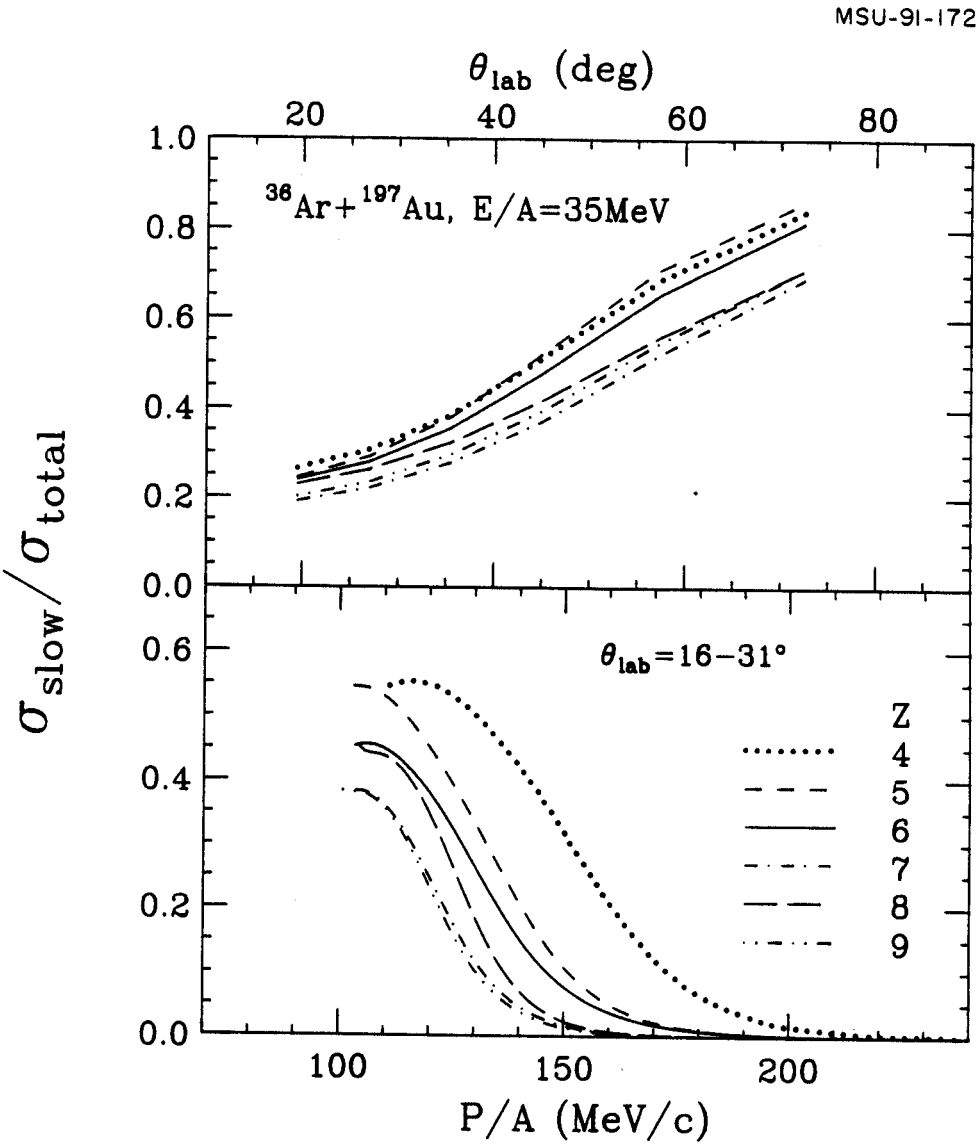

Figure 5.11 Equilibrium fraction, $\sigma_{slow}/\sigma_{total}$, extracted from the fit the data in Fig. 9. Top panel: dependence of energy integrated yield on laboratory angle; bottom panel: dependence on P/A, the momentum per nucleon, of fragments detected at $16° \leq \theta_{lab} \leq 31°$.

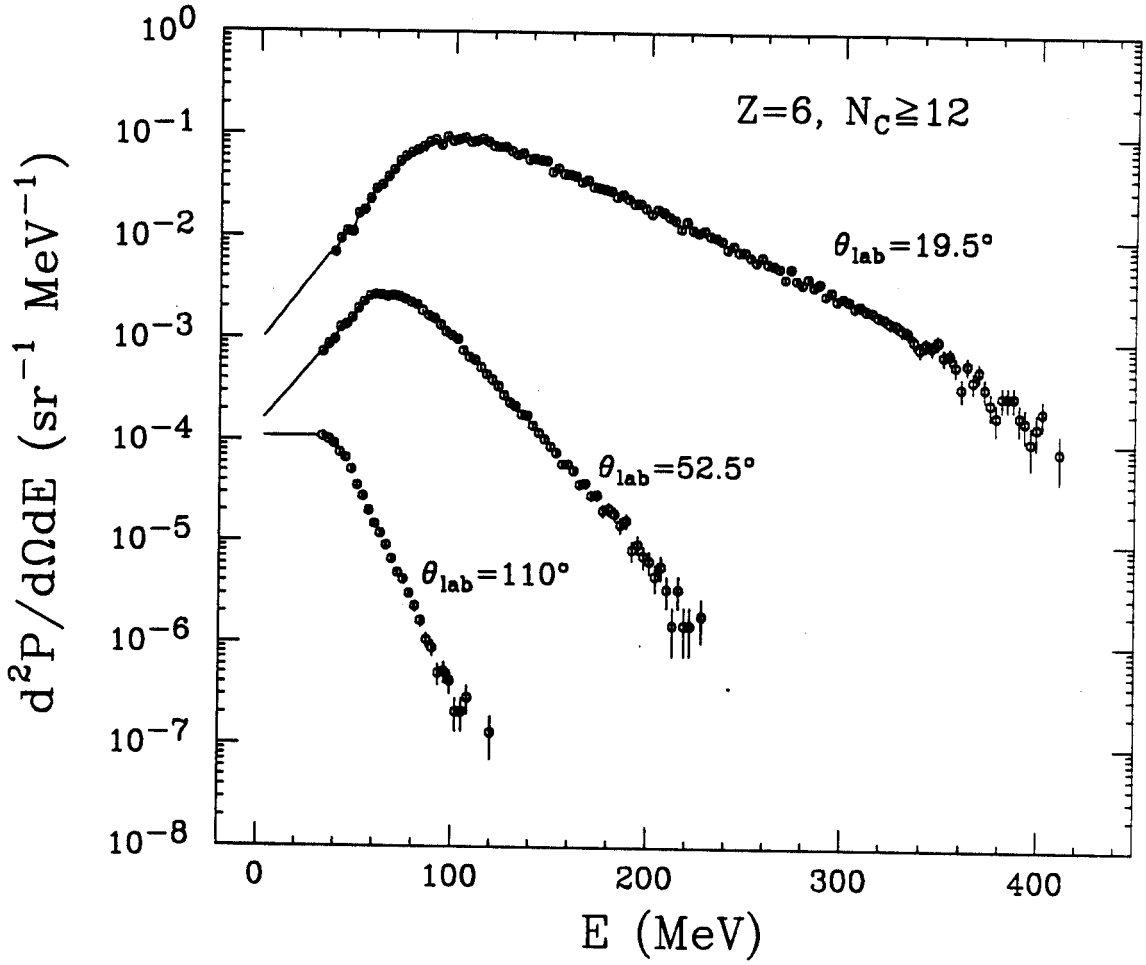

Figure 5.12 Extrapolations of the energy spectra to below the threshold for Z=6 and central collisions. The solid lines show estimates of the cross section below the detection threshold.

0° and 180° as shown in the Figure 5.13 for Z=6 and 10 cases. The solid and open points are the probabilities with and without the extrapolations in the energy spectra which are used as higher and lower bounds respectively. $\frac{d\sigma}{d\theta}$ at less than 15° has been estimated by extrapolating as exponential(solid line) and flat(dashes line) distributions for higher and lower bounds respectively. The estimated true multiplicities(upper bounds) are 0.62 for peripheral collisions(114% increase), 1.68 for mid-central collisions(87% increase), and 1.96 for central collisions(76% increase). To get more accurate true IMF multiplicities measurements with low-threshold gas detector are necessary.

Multiplicity gated energy spectra and angular distributions provide clear evidence for significant non-equilibrium IMF emission even in central collisions selected by large charged particle multiplicities. To better characterize the multifragment final state and distinguish between different theoretical scenarios, knowledge of the IMF emission time scale is necessary. This issue will be taken up in Chapters 6 and 7.

5.5 Charge correlation function

To test the assumption of statistically independent emission of intermediate mass fragments, with a reduced sensitivity to the detection inefficiency, we have examined the "charge-correlation function" as suggested in reference [Boa88],

$$C(Z_1,Z_2) = N_0 \{ \sum_{i\neq k} Y_{ik}(Z_1,Z_2) \} / \{ \sum_{i\neq k} Y_i(Z_1)\bullet Y_k(Z_2) \} . \qquad (5.5)$$

Here, $Y_{ik}(Z_1,Z_2)$ denotes the coincidence yield for particles of charge number Z_1 and Z_2 detected in detectors i and k, respectively, and $Y_i(Z)$ denotes the singles

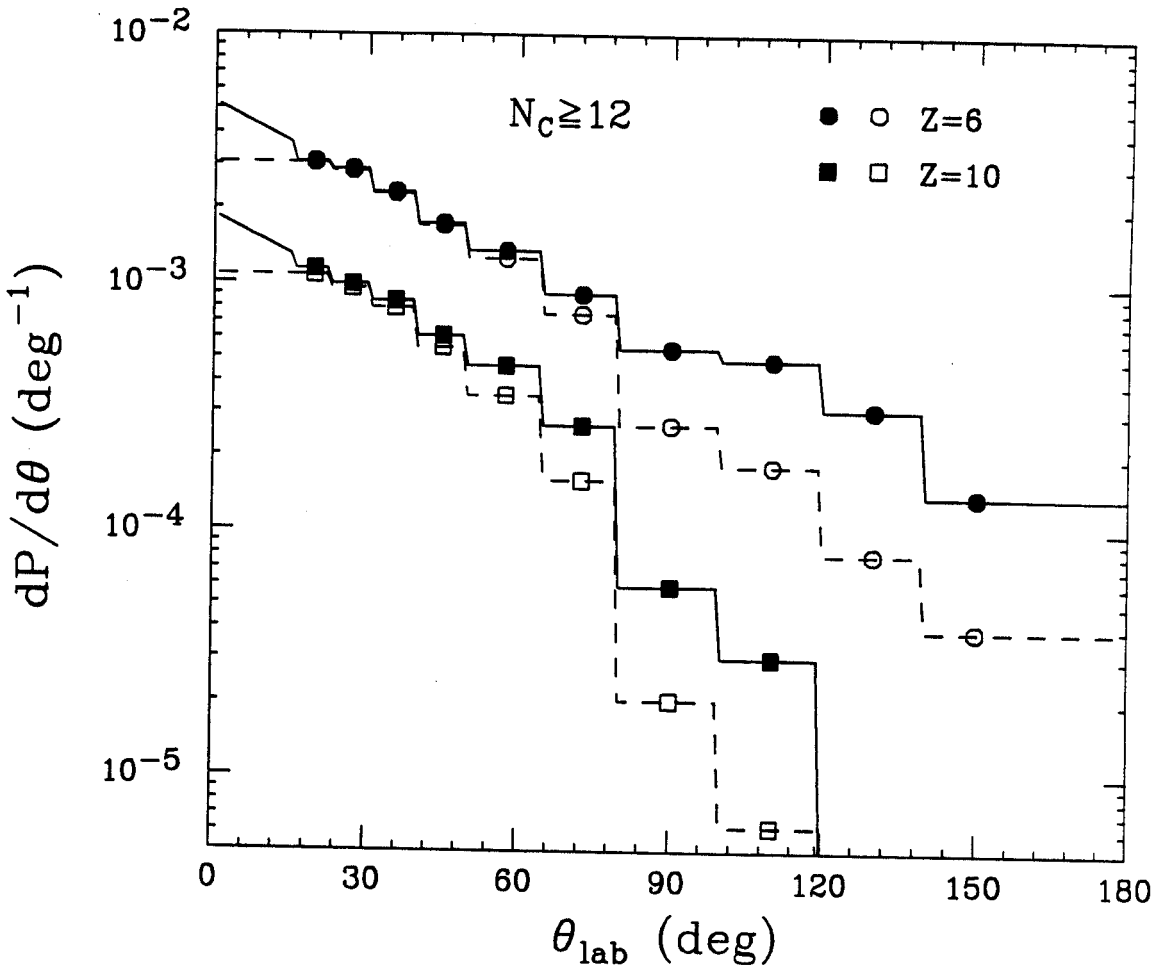

Figure 5.13 Angular probabilities of Z=6 and Z=10 for central collisions. Solid points and open points are the data points with and without the extrapolation in the energy spectra. Solid and dashed curves are the extrapolations up to 0° in $\frac{dP}{d\theta}$ assuming exponential and flat distribution respectively.

yield for particles of charge number Z in detector i. The charge correlation functions obtained from the data of $^{36}Ar + ^{238}U$, at E/A = 35 MeV with Dwarf Wall/Ball were constant within about ±10% for $3 \leq Z_1, Z_2 \leq 6$ [Kim89]. Figure 5.14 shows charge correlation functions for $^{36}Ar + ^{197}Au$ at E/A=35MeV with a broad range of $3 \leq Z_1, Z_2 \leq 20$ as a function of total charge Z_1+Z_2. Except for the case that one IMF is Li, the correlation functions are again constant within about ± 10% when $Z_1+Z_2 \leq 20$, supporting the assumption of statistically independent emission. For $Z_1+Z_2>20$ correlation functions decrease monotonically as a function of Z_1+Z_2 reaching about 0.6 for heaviest combinations. This effect may be due to finite size of the emitting composite system.

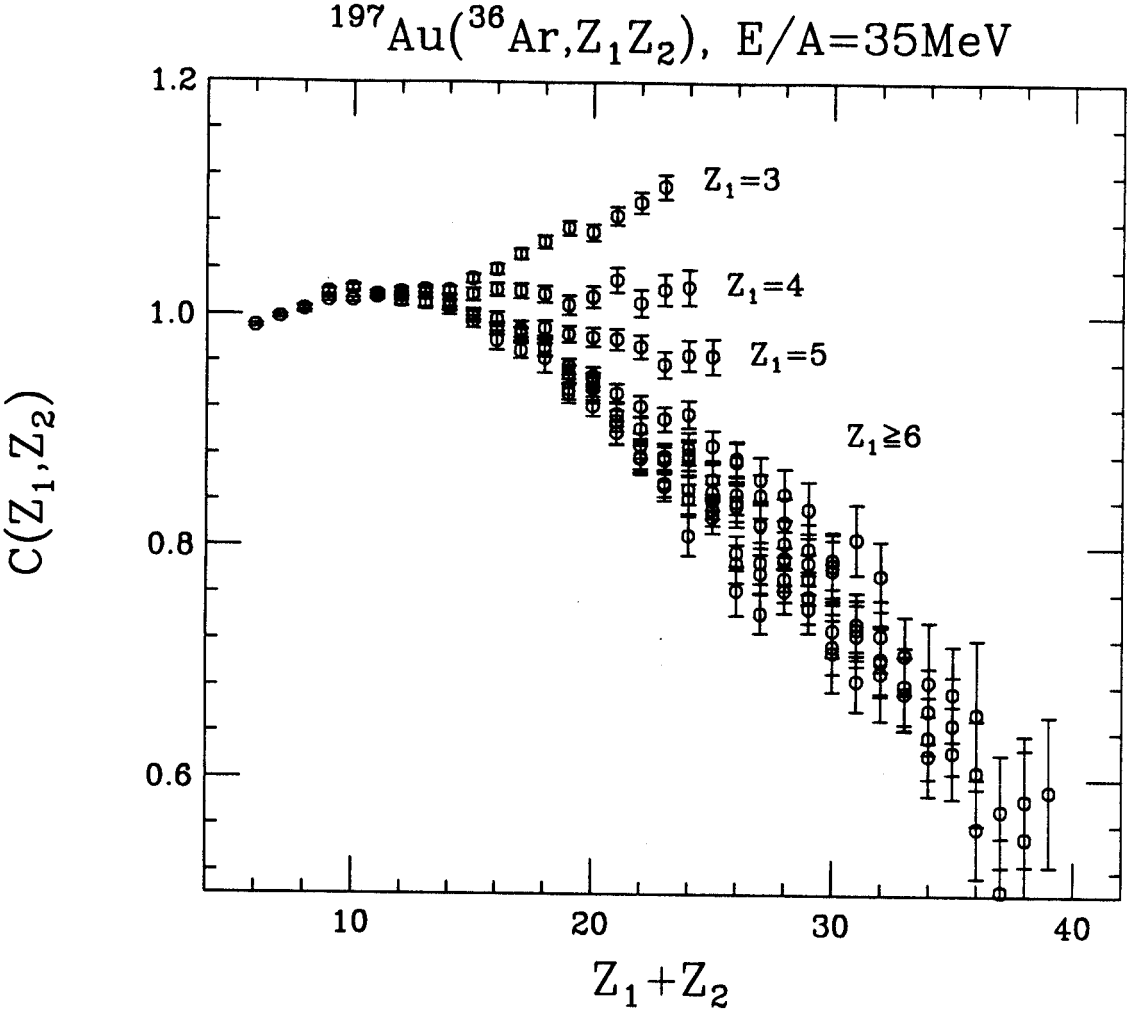

Figure 5.14 Charge correlation functions as a function of Z_1+Z_2 constructed according to equation 5.5.

Chapter 6 Intensity interferometry : A tool to study time scales of multi-fragment emission

6.1 Overview

When two particles are emitted in close proximity and with small relative momenta, their relative wave-function is affected by final state interactions and, for identical particles, by quantum statistics. Therefore, two-particle correlation functions at small relative momenta are sensitive to the space-time evolution of the emitting system [Boa90b,Koo77,Gon91a]. When interactions with the residual system can be neglected, the two-particle correlation functions depend essentially on the single-particle phase-space density of the emitted particles [Pra87,Gon91a].

Up to now, quantitative comparisons of experimental correlation functions with predictions from specific reaction models have largely been performed for the case of two-proton correlation functions. Rather gratifying agreement between theory and experiment was found for emission processes occurring on rather different time scales. Two-proton correlation functions measured for evaporative emission from equilibrated reaction residues could be understood in terms of slow emission time scales predicted by compound nucleus decay models [DeY89,Qui89,Ard89,Gon90a,Gon91b]. Two-proton correlation functions measured for non-compound emission processes were found to be in good agreement with the space-time evolution of the reaction zone as predicted by the Boltzmann-Uehling-Uhlenbeck equation [Gon91b,Gon90b].

While the time scales of nucleon emission processes appear to be reasonably well understood, those governing the emission of intermediate mass fragments in energetic nucleus-nucleus collisions are much less certain and subject to controversial interpretations. In this chapter, we explore the sensitivity of correlations between two intermediate mass fragments to the emission time scales. For this purpose, we apply the formalism of refs. [Koo77,Pra87,Gon91a] to the calculation of two-fragment correlation functions resulting from the final-state Coulomb interaction between the two detected fragments. To a high degree of accuracy, such correlations can be treated classically. In many cases of practical interest, the fragments are emitted in the vicinity of a heavy reaction residue. In such cases, the neglect of Coulomb interactions with the residual system may not be justified. In order to assess the effects of distortions in the Coulomb field of the residual system, we will also present correlation functions calculated by means of three-body trajectory calculations.

This chapter is organized as follows. In Section 6.2, we summarize the Koonin-Pratt formalism of reference [Gon91a], and give a brief derivation of the classical approximation to this formalism treating only the Coulomb interaction between the two detected fragments in Section 6.3. In Section 6.4, we compare longitudinal, transverse, and angle-averaged correlation functions, calculated with the generalized Koonin-Pratt formula by treating the Coulomb interaction between the two detected particles classically and quantum mechanically. Results of three-body trajectory calculations are presented in Section 6.5.

6.2 Koonin-Pratt formalism

In intensity interferometry the two fragment correlation function $1+R(\vec{P},\vec{q})$ is defined by the expression :

$$\Pi(\vec{p}_1,\vec{p}_2) = (1+R(\vec{P},\vec{q}))\Pi(\vec{p}_1)\Pi(\vec{p}_2)\,, \qquad (6.1)$$

where $\vec{P}=\vec{p}_1+\vec{p}_2$, $\vec{q}=\mu(\vec{p}_1/m_1-\vec{p}_2/m_2)=\mu\vec{v}_{rel}$ and μ are the total momentum, relative momentum and reduced mass, respectively, which are quantities constructed from the individual momenta $\vec{p}_1$ and $\vec{p}_2$ and individual masses m_1 and m_2 of fragments 1 and 2, respectively, and $\Pi(\vec{p}_1,\vec{p}_2)$ and $\Pi(p)$ denote the two-particle and single-particle emission probabilities.

The experimental correlation function, 1+R, is constructed from the measured coincidence and single-particle yields, $Y_{12}(\vec{p}_1,\vec{p}_2)$ and $Y_i(\vec{p}_i)$, respectively, according to the expression

$$\Sigma Y_{12}(\vec{p}_1,\vec{p}_2) = C(1+R(\zeta))\,\Sigma Y_1(\vec{p}_1)Y_2(\vec{p}_2)\,, \qquad (6.2)$$

where ζ is relative momentum q or "reduced" relative velocity v_{red} (see eq. 6.19 below). The normalization constant C is determined by the requirement that $<R(\zeta)>=0$ for values of ζ sufficiently large that the final state interaction between the emitted fragments can be neglected. For each gating condition (on P and/or other quantities), the correlation function is evaluated by summing both sides of Eq. 6.2 over all momentum combinations corresponding to given values of ζ. Since the yields differ from the emission probabilities only by overall normalization constants, Eq. 6.2 is equivalent to Eq. 6.1

The usual treatment of two-proton correlations at higher energies is based upon the Koonin-Pratt formula. The derivation of this formula is based upon the assumptions 1) that the final-state interaction between the two detected protons dominates, 2) that final-state interactions with all remaining particles can be neglected, 3) that single particle phase space distribution varies slowly over characteristic momenta, and 4) that the correlation functions are determined by

the two-body density of states as corrected by the interactions between the two particles. The density of states for two particles separated by the relative coordinate $\vec{r}$ and emitted in the asymptotic state characterized by the relative momentum $\vec{q}$ is the square of the relative wave function. If the two fragments are emitted simultaneously with thermal distributions or if the momentum distributions are very broad, as is the case at high energy, this approach provides a near-exact answer provided interactions with third bodies may be neglected. For emission from long-lived compound nuclei, the emission is thermal but far from simultaneous. Furthermore, distortions in the long-range Coulomb field of the residual nucleus might not be negligible, especially for particles emitted with energies close to the exit channel Coulomb barrier. While the Koonin-Pratt formula is expected to be reliable for higher energy collisions which are characterized by rapid disintegrations, its range of validity is less clear when it is applied to less energetic regimes.

The Koonin-Pratt formula allows the calculation of the two-particle correlation function in terms of the single particle phase space distribution and the relative wave function of the emitted particle pair [Gon91a]:

$$1+R(\vec{P},\vec{q}) = \int d^3r F_{\vec{P}}(\vec{r}) \, |\phi(\vec{q},\vec{r})|^2 . \qquad (6.3)$$

Here, $\vec{P}=\vec{p}_1+\vec{p}_2$ is the total momentum of the proton pair and $\phi(\vec{q},\vec{r})$ is the relative two-particle wave function. Here $\vec{q}=\mu d\vec{r}/dt$ is the relative momentum between the two particles, $\vec{r}$ is the relative coordinate, and $\mu=m_1m_2/(m_1+m_2)$ is the reduced mass. The relative Wigner function $F_{\vec{P}}(\vec{r})$ is defined by:

$$F_{\vec{P}}(\vec{r}) = \frac{\int d^3X f_1(\vec{P}\mu/m_2,\ \vec{X}+\vec{r}\mu/m_1, t_>)\, f_2(\vec{P}\mu/m_1,\ \vec{X}-\vec{r}\mu/m_2, t_>)}{\left|\int d^3X_1 f_1(\vec{P}\mu/m_2, \vec{X}_1, t_>)\cdot\int d^3X_2 f_2(\vec{P}\mu/m_1, \vec{X}_2, t_>)\right|} . \qquad (6.4)$$

Here, $\vec{X}$ is the coordinate of the center-of-mass of the fragment pair, $f_i(\vec{p}_i,\vec{r}_i,t_>)$ is the phase-space distribution of particles of type i with momentum $\vec{p}_i$ at position $\vec{r}_i$ at some time $t_>$ after the emission process. If the particles cease to interact at a time earlier than $t_>$, then the relative Wigner function is independent of the particular choice of $t_>$ and the function $f_i(\vec{p}_i,\vec{r}_i,t_>)$ can be expressed in terms of the emission function, $g_i(\vec{p}_i,\vec{r}_i,t)$, i.e. the probability of emitting a particle of type i with momentum $\vec{p}_i$ at location $\vec{r}_i$ and time t [Gon91a]:

$$f_i(\vec{p}_i,\vec{r}_i,t_>) = \int_{-\infty}^{t_>} dt\, g_i[\vec{p}_i,\vec{r}_i-\vec{p}_i(t_>-t)/m_i,t] \,. \qquad (6.5)$$

The relative wave function $\phi(\vec{q},\vec{r})$ is influenced by three different effects : identical particle interference, short range nuclear interaction, and the long range Coulomb interaction. It has been shown that all these three effects are important for proton-proton correlation function. For the calculation of the correlation functions between two IMF's, we neglect the identical particle interference and nuclear interaction because average separations between two fragments are expected to be larger than the range of the nuclear force and Coulomb effects are expected to be predominant. Furthermore, only phase space points are integrated over for which the relative separation between the two fragments is larger than the sum of their radii, $r>1.2(A_1^{1/3}+A_2^{1/3})$ fm.

6.3 Classical treatment of two-fragment Coulomb interaction

Calculations based upon Eq. 6.2 using Coulomb wave function are rather tedious and time consuming. It is, therefore, of interest to derive a classical expression. Again, we assume that the correlation function is the ratio of available states with and without interactions. If $\vec{q}_0$ and $\vec{q}$ denote the initial and final relative momentum vectors, we have:

$$C(\vec{q},\vec{r}_0) \approx \left| \frac{q_0^2 dq_0 \ \sin\theta_0 d\theta_0 \ d\phi_0}{q^2 dq \ \sin\theta d\theta \ d\phi} \right| . \qquad (6.6)$$

Here, θ_0 and θ denote the angles between the initial relative position vector $\vec{r}_0$ and the initial and final momentum vectors, respectively: $\cos\theta_0 = \hat{r}_0 \cdot \hat{q}_0$ and $\cos\theta = \hat{r}_0 \cdot \hat{q}$. From angular momentum conservation, we have for azimuthal rotations about the axis parallel to $\hat{r}_0$:

$$d\phi = d\phi_0 . \qquad (6.7)$$

Energy conservation gives the relation

$$q_0^2 = q^2 - 2\mu\kappa/r_0 , \qquad (6.8)$$

where $\kappa = Z_1 Z_2 e^2$ is the product of the charges of the two emitted fragments. From Eq. 6.8 one immediately obtains

$$q_0^2 dq_0 = (1 - 2\mu\kappa/q^2 r_0)^{1/2} q^2 dq . \qquad (6.9)$$

By using the fact that the eccentricity vector[Gol80],

$$\vec{\varepsilon} = \vec{q}\times\vec{L}/\mu\kappa + \hat{r} = \vec{q}\times(\vec{r}\times\vec{q})/\mu\kappa + \hat{r} \ , \tag{6.10}$$

is a constant of motion and equating its two components in the scattering plane at the time of emission and at very large times, one obtains the following relations:

$$\mu\kappa + r_0 q_0^2 \sin^2\theta_0 = \mu\kappa\cos\theta + r_0 q q_0 \sin\theta\sin\theta_0 \ , \tag{6.11}$$

$$r_0 q_0^2 \cos\theta_0 \sin\theta_0 = r_0 q q_0 \cos\theta\sin\theta_0 - \mu\kappa\sin\theta \ . \tag{6.12}$$

Here, we made use of angular momentum conservation and of the fact that the two vectors $\vec{r}$ and $\vec{q}$ become parallel for $t\to\infty$. Equation 6.10 can be cast into the form:

$$\sin\theta_0 = (q/2q_0)\{\sin\theta \pm [\sin^2\theta - 4\mu\kappa(1-\cos\theta)/r_0 q^2]^{1/2}\} \ . \tag{6.13}$$

Equation 6.12 has two solutions: for given final relative momentum $\vec{q}$, there are two different trajectories which pass through the relative coordinate $\vec{r}_0$. Both trajectories must be considered when calculating the correlation function. Equation 6.11 can be written as:

$$\cos\theta_0 = (q/q_0)\cos\theta - (\mu\kappa/r_0 q_0^2)\sin\theta/\sin\theta_0 \ . \tag{6.14}$$

Differentiation of Eq. 6.13 yields:

$$d\theta_0/d\theta = \frac{q}{2q_0\cos\theta_0}\{\cos\theta \pm \frac{\cos\theta\sin\theta - 2\mu\kappa \sin\theta/r_0q^2}{[\sin^2\theta - 4\mu\kappa(1-\cos\theta)/r_0q^2]^{1/2}}\}. \qquad (6.15)$$

Using Eqs. 6.8, 6.13-6.15, one can express $\sin\theta_0 d\theta_0/\sin\theta d\theta$ in terms of the of the initial relative coordinate r_0 and the asymptotic values of θ and q. Hence, Eqs. 6.7-6.9, 6.13-6.15 allow the expression of Eq. 6.6 in terms of the final relative momentum and the initial relative position of the emitted particles. Integration over all relative positions of the emitted particles gives the final expression for the correlation function:

$$1+R(\vec{P},\vec{q}) = \int d^3r_0 F_{\vec{P}}(\vec{r}_0) C(\vec{q},\vec{r}_0). \qquad (6.16)$$

If all directions of $\vec{q}$ are integrated over, Eq. 6.16 reduces to a particularly simple expression,

$$1+R(\vec{P},\vec{q}) = \int d^3r_0 F_{\vec{P}}(\vec{r}_0)[1-2\mu\kappa/q^2r_0]^{1/2}. \qquad (6.17)$$

which can be used for calculating the angle integrated correlation function 1+R(P,q). Equation 6.17 indicates that two-fragment correlation functions measured for different particle pairs depend largely on the variable

$$\mu\kappa/q^2 = \mu e^2 Z_1 Z_2/(\mu v_{rel})^2 \propto (Z_1+Z_2)/v_{rel}^2. \qquad (6.18)$$

In the last step, we have made use of the fact that most intermediate mass fragments are produced close to the valley of stability, i.e. we have approximated $m_i \propto 2Z_i$. Within this approximation, one can generate two-fragment correlation

functions by combining the statistics from several fragment combinations and evaluating the dependence as a function of the "reduced" relative velocity,

$$v_{red} = v_{rel}/\sqrt{Z_1+Z_2} \quad . \tag{6.19}$$

We will use this variable to display the results of our numerical calculations. The use of the reduced velocity as an independent variable is different from the convention employed in reference [Tro87] where mixed-fragment correlations were evaluated as a function of relative velocity of the emitted fragments. Close inspection of Eqs. 6.6-6.9, 6.13-6.15 shows that most of these relations also scale as $\mu\kappa/q^2$, the only exception being Eq. 6.14 which contains a term which scales as $\mu\kappa/q_0^2$. If dependences on the angle θ are important, scaling of mixed-fragment correlations with $\mu\kappa/q^2$ is not exact, but it may still be a reasonable approximation.

6.4 Validity of classical approximation

In this section we assess the validity of the classical approximation, Eqs. 6.5-6.8, 6.12-6.15. Calculations with these equations are compared to calculations with Eq. 6.2 in which the full Coulomb scattering wave function is used for the relative wave function. In the calculations, we will use a simple parametrization for the emission functions $g(\vec{p},\vec{r},t)$, corresponding to surface emission from a spherical source of radius R_S with a fixed lifetime τ and a Maxwellian energy distribution characterized by a temperature parameter T:

$$g(\vec{p},\vec{r},t) \propto (\hat{r}\bullet\hat{p})\Theta(\hat{r}\bullet\hat{p})\delta(r-R_S)\Theta(E-V_C)\sqrt{E-V_C}\, e^{-(E-V_C)/T}\, e^{-t/\tau} \tag{6.20}$$

Here, $\Theta(x)$ is the unit step function which vanishes for $x<0$, $\delta(x)$ is the delta function, $\hat{r}$ and $\hat{p}$ are unit vectors parallel to $\vec{r}$ and $\vec{p}$, and $E=p^2/2m$. The parameter V_C is introduced to account for Coulomb repulsion when emission occurs from the surface of a heavy reaction residue assumed to be at rest at the origin of our coordinate system. The relative wave function can be calculated by using a partial wave expansion of the Coulomb scattering amplitude [Mes61] :

$$\phi_c = \frac{1}{kr}\sum_{\ell=0}^{\infty}(2\ell+1)i^{\ell}e^{i\sigma_{\ell}}F_{\ell}(\eta;qr)P_{\ell}(\cos\theta) \qquad (6.21)$$

Here, σ_{ℓ} is Coulomb phase shift and, $\eta=Z_1Z_2\alpha\mu c/q$ is the Sommerfeld parameter and $\alpha=2\pi e^2/hc\approx 1/137$ is the fine structure constant. In our quantum mechanical treatment of the two-fragment Coulomb interaction, the number, ℓ_{max}, of partial waves included in the calculations was scaled according to the classical relation $\ell_{max}=20(h/2\pi)+(q^2r^2-2\eta qr)^{1/2}$. We used computer code "COULFG" published by A.R. Barnett [Bar81] for numerical calculation of Coulomb function $F_{\ell}(\eta;qr)$.

As a specific example, we calculated correlation functions for the emission of two distinguishable carbon nuclei with the parameters T=15 MeV, R_S=12 fm, V_C= 63 MeV and various mean lifetimes τ. Figure 6.1 gives a comparison of correlation functions integrated over all relative orientations between the total and relative momenta of the two emitted fragments. The points show calculations with Eq. 6.3 and the curves show results obtained with the classical expression, Eq. 6.17. The two calculations produce virtually identical results indicating that the classical approximation is very well justified. (Some small differences exist at large relative velocities for the calculations with τ=500 fm/c; these are due to the limitation in the number of partial waves (<1000) used in our calculations with Eq. 6.3.)

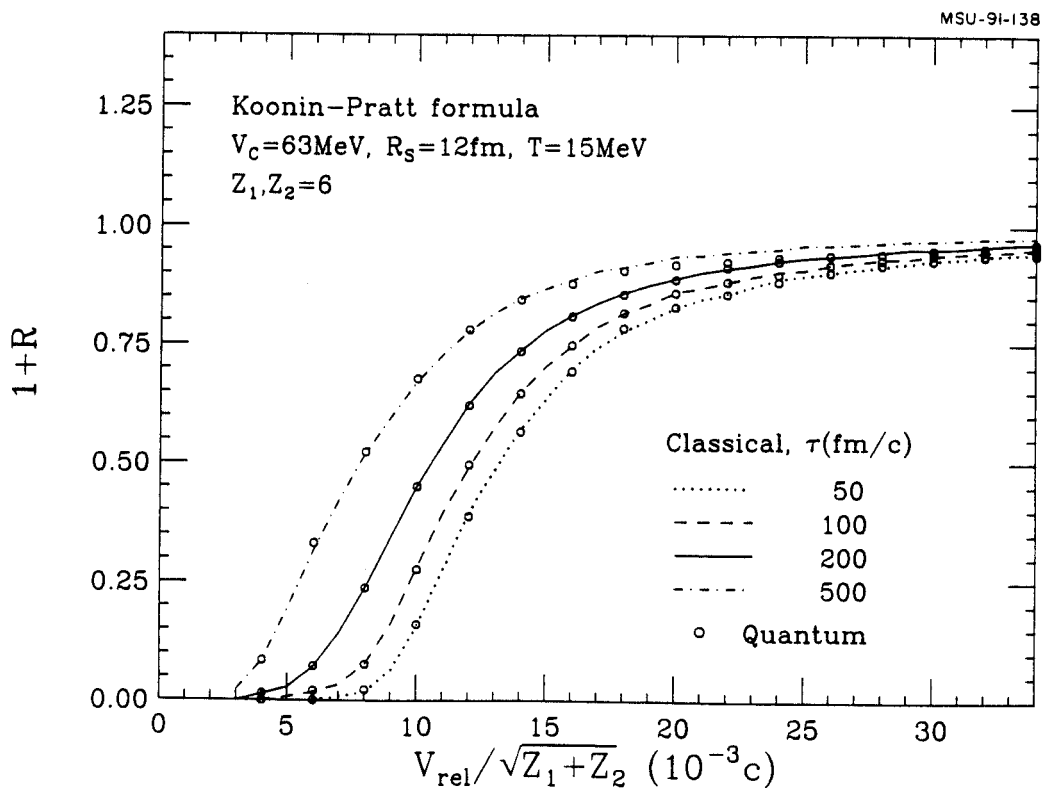

Figure 6.1 Comparison of angle-integrated carbon-carbon correlation functions. Calculations with Eq. 6.3 are shown by points; calculations with the classical approximation, Eq. 6.17, are shown by the curves. The emission times are indicated in the figure.

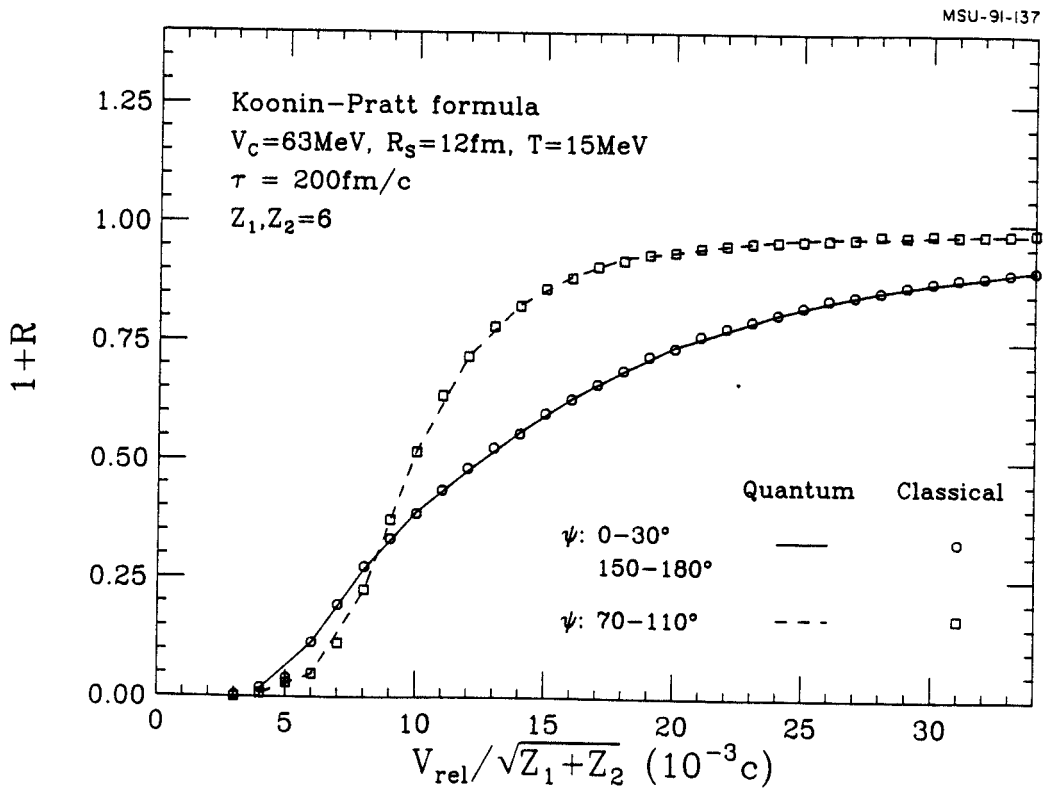

Figure 6.2 Longitudinal and transverse correlation functions for τ=200 fm/c. Longitudinal correlation functions (ψ=0°-30° or ψ=150°-180°) are shown by the solid curve and circular points; transverse correlation functions (ψ=70°-110°) are shown by the dashed curve and square points. Curves show calculations with Eq. 6.3; points show calculations with Eqs. 6.6-9, 6.13-16.

In Figure 6.2, calculations for longitudinal and transverse correlation functions are compared for τ=200 fm/c. These correlation functions are defined in terms of the angle ψ between $\vec{P}$ and $\vec{q}$, $\psi=\cos^{-1}(\vec{P}\bullet\vec{q}/Pq)$. Longitudinal correlation functions correspond to the angular interval ψ=0°-30° or ψ=150°-180°; transverse correlation functions correspond to the angular interval ψ=80°-100°. The curves show the results obtained with Eq. 6.3 and the points show the results obtained with the classical relations, Eqs. 6.6-6.9, 6.13-6.16. Again, the two calculations produce virtually identical results. We conclude that classical treatments of correlation functions between intermediate mass fragments provide an excellent approximation. The validity of the classical approximation is, of course, expected for emission from sources with dimensions comparable to or larger than the Bohr radius. For the two-carbon system the Bohr radius is 0.13 fm which is, indeed, much smaller than the size of the emitting system.

For emission from long-lived systems, longitudinal correlation functions are predicted to exhibit a wider minimum at q≈0 than transverse correlation functions. This directional dependence is due to the fact that the Coulomb force is parallel to the relative displacement of the particles. Therefore, the Coulomb hole in the correlation function will be strongest when the relative momentum is parallel to the longest dimension of the pair's separation. For long-lived sources this is the longitudinal direction [Pra87,Gon91a].

6.5 Trajectory calculation

The derivation of Eq. 6.3 is based upon the assumptions that the phase space distribution does not vary significantly over the range ½P±q and, furthermore, that dynamical correlations and distortions in the Coulomb field of other reaction residues can be neglected. In this section we assess the validity of

these assumptions by means of trajectory calculations. The use of trajectory calculations is justified by the validity of the classical approximation.

In our trajectory calculations we consider the sequential emission of two carbon nuclei from the surface of a source of radius R_S which is initially at rest and which has a total charge of $Q_S=Z_S e=93e$ and a total mass of $M_S=A_S$ u. In order to isolate the effect of three body Coulomb distortions from dynamic distortions resulting from the recoil of the emitting system, we use an artificially large mass number for the emitting source, $A_S=10000$. Further below, we evaluate recoil effects for a more realistic heavy source of mass number $A_S=226$. To be consistent with the calculations presented in Section 6.4, we assumed an emission function of the form:

$$g(\vec{p},\vec{r},t) \propto (\hat{r}\bullet\hat{p})\Theta(\hat{r}\bullet\hat{p})\delta(r-R_S)\Theta(E)\sqrt{E}\,e^{-E/T}\,e^{-t/\tau}\,. \qquad (6.22)$$

This emission function was sampled by Monte-Carlo techniques. Upon emission, the particle trajectories were calculated by integrating Newton's equations, and the asymptotic particle momenta were stored as coincidence events and as single-particle spectra. Correlation functions, 1+R, were constructed in the same way as experimental data using Eq. 6.2.

First, we explore the validity of using the approximate form of the phase space distribution, Eq. 6.4. For this purpose we have performed trajectory calculations in which the Coulomb interaction with the emitting source was turned off. In this case, the relation between initial and final two-fragment phase space points can be calculated analytically. In Figure 6.3, the results of these calculations are compared to calculations based upon Eq. 6.17 (these latter calculations are identical with results obtained from Eq. 6.3). The open points

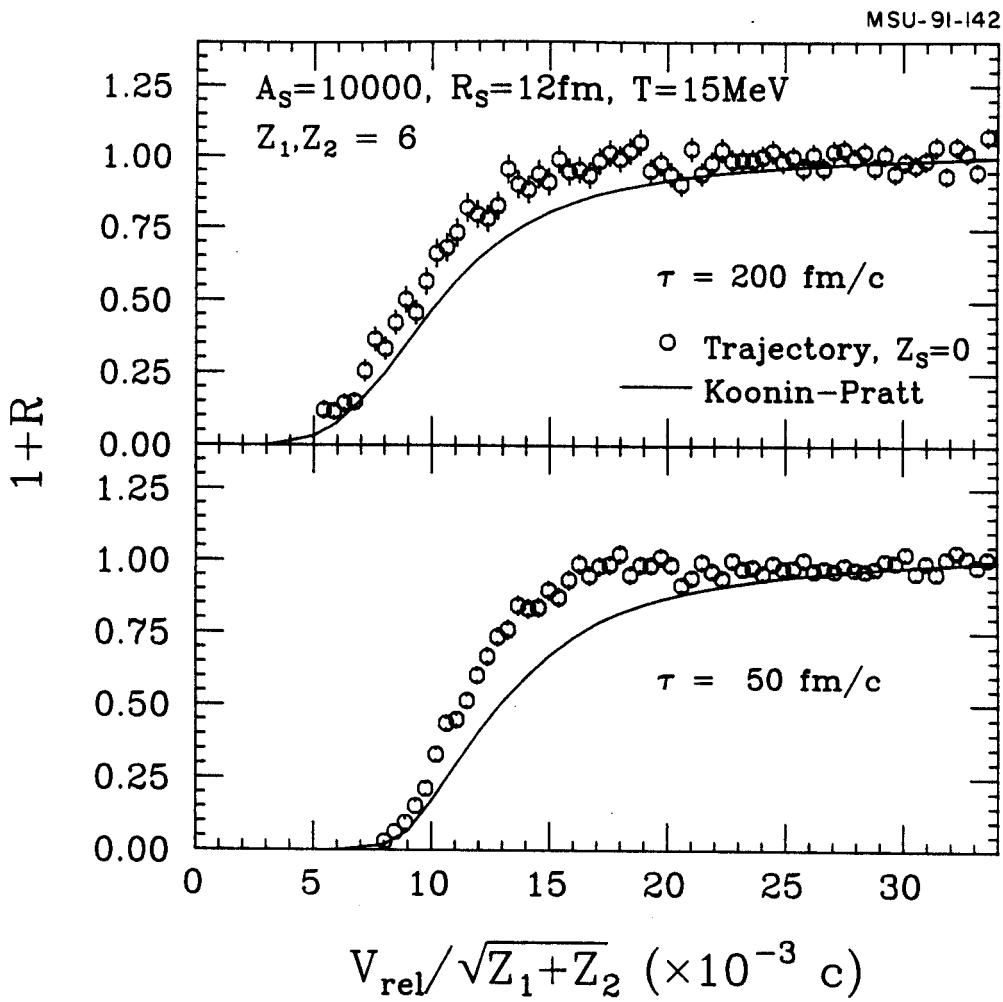

Figure 6.3 The points represent correlation functions obtained via trajectory calculations assuming emission from an uncharged source; the curves show the results obtained from Eq. 6.17. The parameters used in these calculations are indicated in the figure.

represent the results obtained from these trajectory calculations and the curves show the results obtained from Eqs. 6.17. The difference between the two calculations is significant, but not necessarily surprising. The emission function varies over characteristic momenta of the order of $\Delta p \approx \sqrt{2mT} \approx 0.6$ GeV/c. The Coulomb minimum of the two-fragment correlation function has a width of the order of $\Delta q \approx 0.2\text{-}0.3$ GeV/c. Hence, the condition $\Delta q << \Delta p$ is only poorly satisfied. It is somewhat better satisfied for large values of τ than for small values of τ. Therefore, the agreement between the two calculations becomes better for larger lifetimes. According to the above arguments, the discrepancy between trajectory calculations and calculations based upon Eq. 6.3 or 6.17 should become less for larger slope parameters T used to characterize the energy spectra. This expectation is borne out in the calculations shown by the solid points in Figure 6.4, which were performed for the extreme limit of flat energy spectra, $T=\infty$, for two ranges of the total momentum P of the particle pair. For the emission of energetic fragments, $P/A \geq 150$ MeV/c, reasonable agreement exists with results from the Koonin-Pratt formula (upper panel of Figure 6.4). However, for low-energy fragments, $P \leq 140$ MeV/c, the discrepancies are still considerable (lower panel of Figure 6.4).

In Figure 6.5 we compare two-carbon correlation functions calculated by means of trajectory calculations (points) with correlation function calculated with Eqs. 6.17 (curves). The upper and lower panels show the results for carbon pairs emitted with total momenta per nucleon, $P/A \leq 110$ MeV/c and $P/A \geq 110$ MeV/c, respectively. For the low momentum gate, the fragments are emitted with very small initial velocities and distortions in the Coulomb field of the emitting source should be maximal. Indeed, significant distortions already exist for $\tau = 200$ fm/c. For longer emission times, calculations with Eq. 17 can still provide useful guidance, as is illustrated by the good agreement with the trajectory calculations

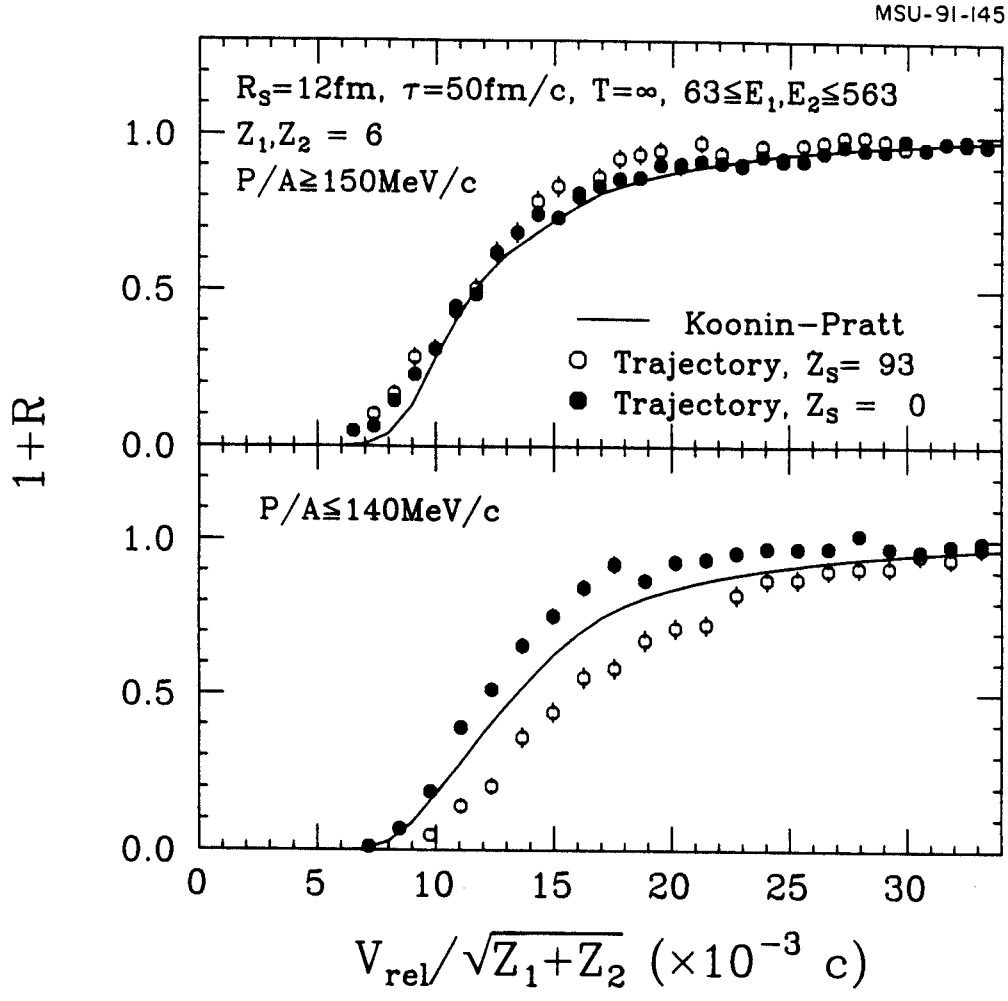

Figure 6.4 Calculations for flat fragment spectra, T=∞, integrated over the indicated momentum intervals. The solid points represent correlation functions obtained via trajectory calculations assuming emission from an uncharged source; the curves show the results obtained from Eq. 6.17; the open points represent three-body Coulomb calculations neglecting recoil effects. The parameters used in these calculations are indicated in the figure.

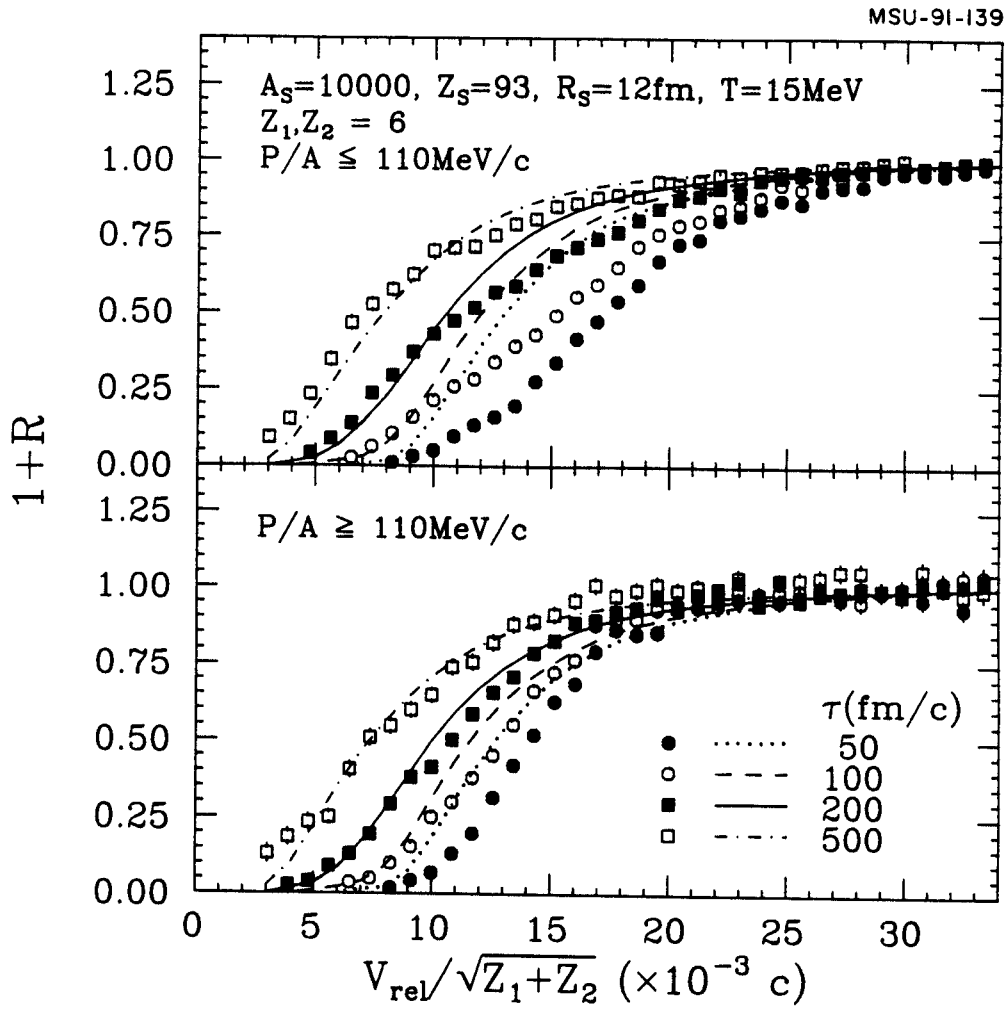

Figure 6.5 Comparison of two-carbon correlation functions calculated by means of three-body trajectory calculations (points) with correlation functions calculated with Eq. 6.17 (curves). Upper and lower panels show results for total momenta per nucleon of P/A≤110 MeV/c and P/A≥110 MeV/c, respectively. The parameters used in these calculations are indicated in the figure.

for τ=500 fm/c. However, for shorter lifetimes ($\tau \lesssim$200 fm/c) distortions in the Coulomb field of the emitting source become so large that Eqs. 6.17 become virtually useless. As may be expected, distortions by the Coulomb field of the emitting system are less important for fragment pairs emitted with larger initial velocities. This qualitative expectation is borne out by the calculations for more energetic fragment pairs with P/A$\geq$110 MeV/c. For this momentum gate, Eq. 6.17 provide reasonable approximations for emission times $\tau \gtrsim$200 fm/c. However, for shorter emission times, the disagreement is still substantial, though much smaller than for the low-momentum gate.

For the emission of rather energetic particles, three-body Coulomb distortions of the angle averaged correlation functions become small, even for rather short emission times. As an example, the open points in Figure 6.4 show the results of three-body Coulomb trajectory calculations performed for flat energy spectra, T=∞, and for Z_S=93. For energies well above the Coulomb barrier, P/A$\geq$150 fm/c, the distortions in the field of the emitting source become small and trajectory calculations (for Z_S=0 as well as Z_S=93) agree nearly quantitatively with calculations performed with Eq. 6.17 even for emission time scales as small as τ=50 fm/c. However for low-energy emissions, P/A$\leq$140 MeV/c, the discrepancies are appreciable. It is interesting to note that three-body Coulomb distortions and inaccuracies of the Koonin-Pratt formula for Z_S=0 appear to become small at comparable energies.

Distortions in the Coulomb field of the emitting system can be particularly large for longitudinal and transverse correlation functions. As an example, Figure 6.6 shows longitudinal and transverse correlation functions for a relatively long lifetime, τ=200 fm/c. For this lifetime, the deviations from the angle integrated correlation functions calculated with Eq. 6.3 or 6.17 are still relatively modest (Figure 6.5). In order to increase statistics, we had to widen the

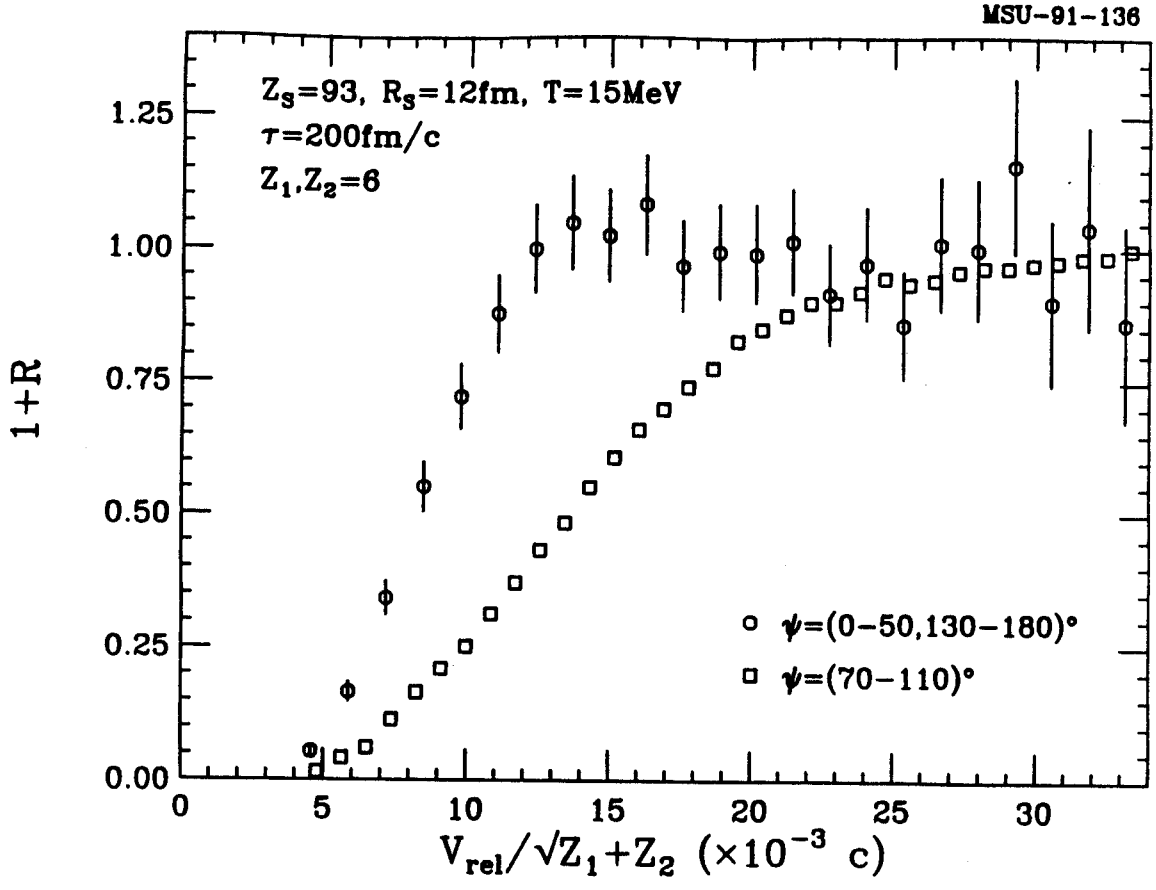

Figure 6.6 Longitudinal and transverse correlation functions between two carbon fragments calculated via trajectory calculations for τ=200 fm/c.

angular acceptance for the longitudinal correlation function, ψ=0°-50° or 130°-180°. (In the present simulation, the energy spectra are relatively strongly peaked at the Coulomb barrier. As a consequence, only relatively few events in the longitudinal gate fall into the region of relative velocities of interest here.) The longitudinal (circular points) and transverse (square shaped points) correlation functions deduced from the trajectory calculations were normalized with the same normalization constant determined from the asymptotic behavior of the angle integrated correlation function. Although the statistical errors for the longitudinal correlation function are large, it is clear that it exhibits a narrower minimum at $v_{red} \approx 0$ than the transverse correlation function, in complete disagreement with the qualitative trends predicted from Eqs. 6.3 or 6.17, see Figure 6.2. Hence, the detailed shape of longitudinal and transverse two-fragment correlation functions can be strongly affected by interactions with the Coulomb field of the residual system. It would be of interest to investigate whether such sensitivities to the charge distribution of the emitting system could be exploited to differentiate between various reaction models for multifragment disintegrations.

Since intermediate mass fragments are emitted with larger average momenta than light particles, one may expect that two-fragment correlation functions can also be affected by dynamical correlations due to momentum conservation effects. In Figure 6.7, we assess the magnitude of distortions resulting from the recoil of heavy reaction residues. The solid points in the figure show three-body trajectory calculations for emission from a realistic source of mass M_S=226 u and the open points show the results for emission from an artificially heavy source of mass M_S=10000 u for which recoil effects are negligible. The upper panel shows calculations for thermal energy spectra with T=15 MeV and the lower panel shows calculations for flat energy spectra, T=∞,

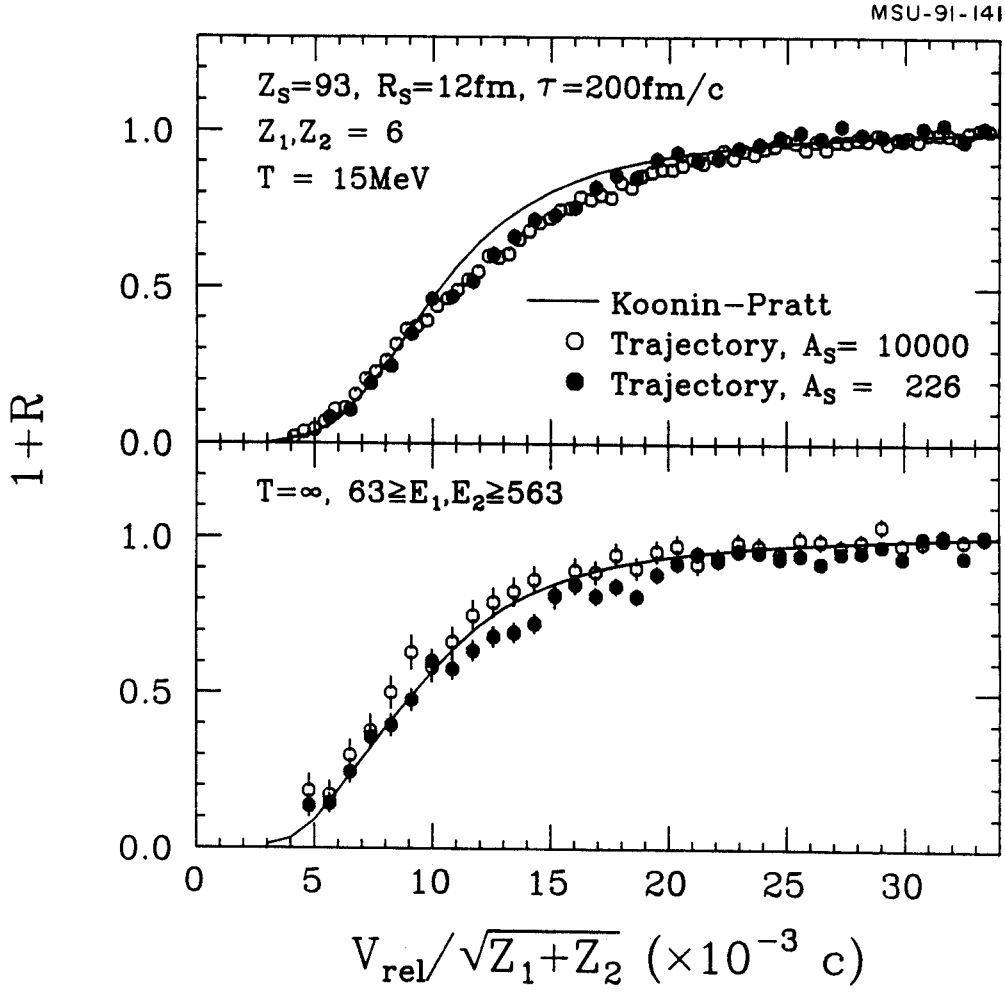

Figure 6.7 Two-carbon correlation functions calculated via three-body trajectory calculations for sources of different masses. Solid points: M_S=226 u, open points M_S=10000 u. The upper panel shows calculations for thermal energy spectra and the lower panel shows calculations for flat energy spectra, T=∞, integrated over the indicated energies. The parameters used in these calculations are indicated in the figure.

averaged over a broad range of energies E_1, E_2 = 63-563 MeV; other parameters of the calculation were kept fixed (R_S=12 fm, Z_S=93, τ=200 fm/c). For the calculations with T=15 MeV, recoil effects introduce only minor distortions, largely because most particles are emitted with energies close to the Coulomb barrier. For the emission of more energetic fragments, recoil effects become slightly more important as is illustrated by the calculations for T=∞, shown in the bottom panel of Figure 6.7. Our schematic investigation is aimed at emission from rather heavy nuclear systems. For lighter sources, of course, recoil effects become more important. One must stress, however, that reasonably unambiguous assessments of recoil effects can only be made within the framework of specific reaction models, particularly for fast noncompound emission processes expected to set in at higher energies. This is because the effects will depend on the details of size and time evolution of the source.

6.6 Conclusion

The schematic model calculations presented in this chapter indicate that two-fragment correlation functions are, indeed, sensitive to the space-time evolution of the emitting system. For large emission times ($\tau \gtrsim 200$ fm/c) and fragment kinetic energies well above the Coulomb barrier, calculations incorporating the mutual Coulomb interaction between the two emitted fragments allow the extraction of emission time scales with reasonable accuracy.

For emission from heavy and highly charged systems, distortions from interactions with the Coulomb field of the residual system can be significant thus rendering the analysis more model dependent. Such distortions are particularly important for fragment emission with low kinetic energies or on fast emission

time scales. Additional model dependences can arise from dynamical correlations resulting, for example, from momentum conservation.

Directional dependences of two-fragment correlation functions are particularly sensitive to final-state Coulomb interactions with the residual system. Indeed, the shapes of longitudinal and transverse correlation functions can be strongly altered by interactions with the Coulomb field of the emitting system, even when the angle-integrated correlation functions appear to suffer only minor distortions. Such enhanced sensitivities of two-fragment correlation functions to properties of the emitting system may contain useful additional information on the emission process and thus allow more stringent tests for various models for multifragment disintegrations. Thus it appears promising to pursue more detailed calculations of two-fragment correlation functions for specific reaction models capable of making predictions of the space-time evolution of nuclear disintegrations by multi-fragment emission.

Chapter 7 Time scales of multi-fragment emission : $^{36}Ar + ^{197}Au$ at E/A=35MeV

7.1 Equal-charge two fragment correlation functions

Experimental two-fragment correlation functions are constructed from fragments detected at forward angles $16° \leq \theta_{lab} \leq 31°$ corresponding to ring 2 and 3 of the Miniball, where the statistics of the experimental data and the granularity of the array are optimal for extracting good-quality correlation functions. First, for simplicity of the discussion, we study correlation functions of two equal-charge fragments.

Figure 7.1 shows experimental two-fragment correlation functions constructed according to Eq. 6.2. The top, center, and bottom panels show Be-Be, B-B, and C-C correlation functions respectively. (Double hits by α-particles resulting, for example, from ^{8}Be decays were identified by pulse shape discrimination and excluded from the data presented in this thesis, see Chapter 4.) The left panels present inclusive correlation functions and the right panels show correlation functions gated by the requirement $N \geq 9$ and $P/A > 150$ MeV/c, where N denotes the total number of charged particles detected in the Miniball and P/A is the total momentum per nucleon of the coincident fragment pair. All correlation functions exhibit pronounced minima at $q \approx 0$ MeV/c which can be attributed to the repulsive final state Coulomb interaction between the emitted fragments. The correlation functions gated by $N \geq 9$ and $P/A > 150$ MeV/c are similar in shape to the inclusive correlation functions, indicating that this gate does not select significantly different emission times.

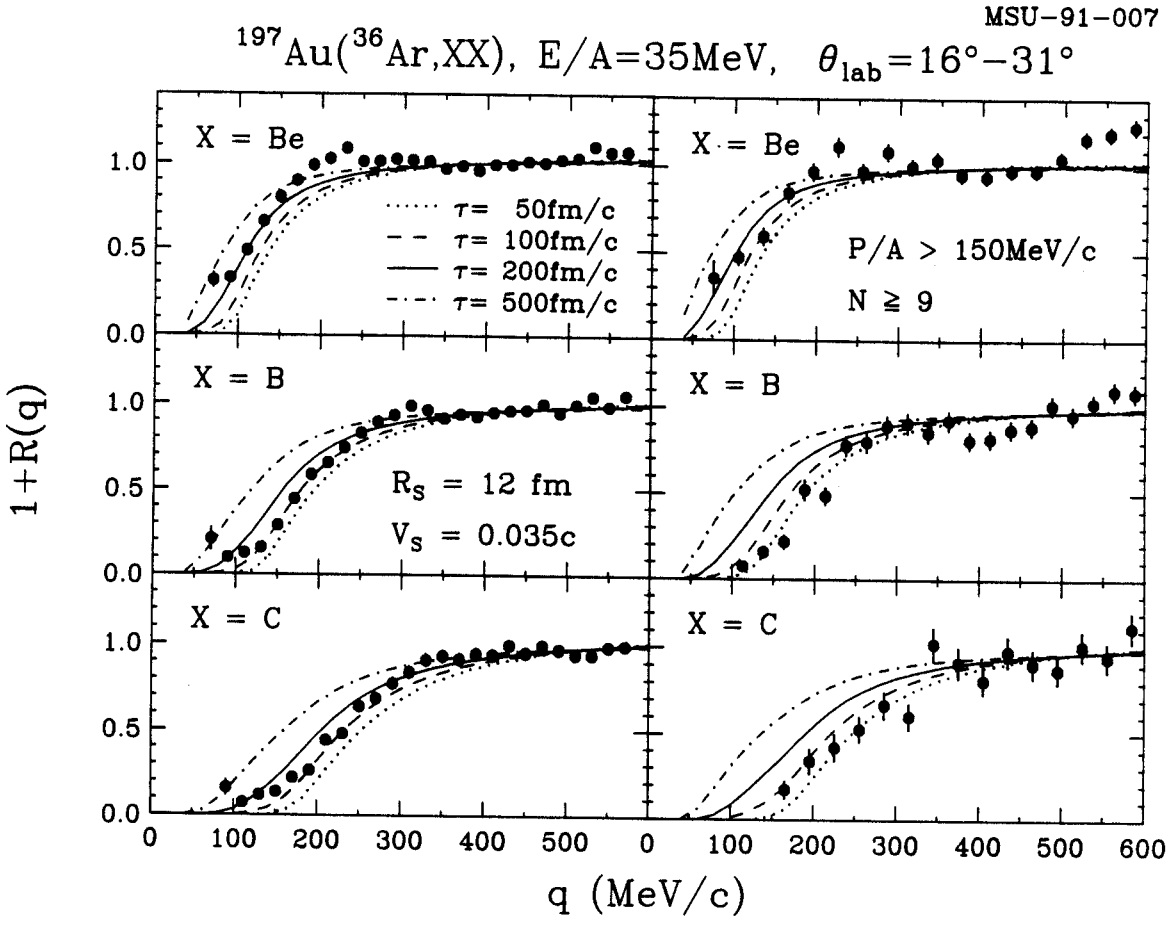

Figure 7.1 Inclusive (left hand panels) and gated (right hand panels) two-fragment correlation functions at small relative momenta. The calculations are explained in the text.

The curves shown in the figure represent calculations with the Koonin-Pratt formula, Eq. 6.17, for an emission function $g(\vec{p},\vec{r},t)$ similar to Eq. 6.20:

$$g(\vec{p},\vec{r},t) \propto (\hat{r}\bullet\hat{p})\Theta(\hat{r}\bullet\hat{p})\delta(r-R_S)\frac{dN}{dEd\Omega}e^{-t/\tau} \quad . \qquad (7.1)$$

The energy and angular distributions $dN/dEd\Omega$ were taken to be consistent with the experimental single fragment distributions. The emitting source was assumed to move with a velocity of v_S=0.035c consistent with emission from the surface of heavy reaction residues formed in incomplete fusion reactions in which 80% of the projectile momentum was transferred to the fusion-like residue (taken from the systematics of linear momentum transfer for reactions producing heavy reaction residues [Fat85]). For the emission of the second fragment, we required a minimum initial separation of $r_{min} = 1.2\,(A_1^{1/3}+A_2^{1/3})$ fm from the first fragment. In all calculations we assumed a fixed source radius of R_S=12 fm. Choosing a smaller source radius leads to more significant Coulomb final state interactions; this, to first order, has the same effect on the correlation function as reducing the emission time scale. Likewise, an increase in the source radius cannot be easily distinguished from an increase in the emission time scale. The comparison between measured and calculated correlation functions in Figure 7.1 indicates that the inclusive correlation functions are reasonably consistent with mean emission times of about $\tau \approx$100-200 fm/c. The correlation functions gated by N≥9 and P/A>150 MeV/c appear to indicate slightly shorter emission time scales.

In our calculations, we neglect the possibility that highly excited primary fragments could undergo sequential decays by particle emission. Such decays may be expected to attenuate the minimum at q≈0 MeV/c [Bar90]. It is, therefore, possible that our analysis yields mean emission times which are slightly larger

than those of the primary fragments. Our data seem to indicate slightly larger emission times for Be fragments than for B or C fragments. Furthermore, the calculations reproduce the Be-Be correlation function less well than the B-B or C-C correlation functions. It is interesting to speculate that these observations could be related to enhanced feeding of Be nuclei. Additional experimental information concerning the magnitude of sequential feeding would help resolve this issue.

Figure 7.2 illustrates systematic uncertainties introduced by our apparatus and data analysis. The curves in panels (a) and (b) show the theoretical B-B correlation functions already presented in the left center panel of Figure 7.1. The solid and open points in panel (a) show the correlation functions for τ=100 and 500 fm/c, respectively, filtered by the response of our apparatus. The resulting distortions are of minor importance. (The instrumental distortions at very small values of q are mainly due to the finite angular resolution of the apparatus; uncertainties in energy calibration ($\approx$5%) are small in comparison.) Panel (b) illustrates errors which could arise from the unknown mass of the detected fragments. The solid and open points show experimental B-B correlation functions constructed by assuming A=10 and A=11, respectively, for the mass of the detected boron fragments. The sensitivity of the calculation to uncertainties of the velocity and size of the emitting source is illustrated in panels (c) and (d). None of these uncertainties changes the extracted lifetimes by more than 50%.

For the present reaction, the charged particle multiplicities are sufficiently low to virtually guarantee the survival of a heavy reaction residue (which might subsequently fission). To assess the influence of the Coulomb field of the heavy reaction residue, we have performed three-body Coulomb trajectory calculations as described in Section 6.5, assuming a residual nucleus initially with charge number Z_S=93, mass number A_S=226, and velocity V_S=0.035c. The emission function was the same as in Eq. 7.1. The response of the experimental apparatus

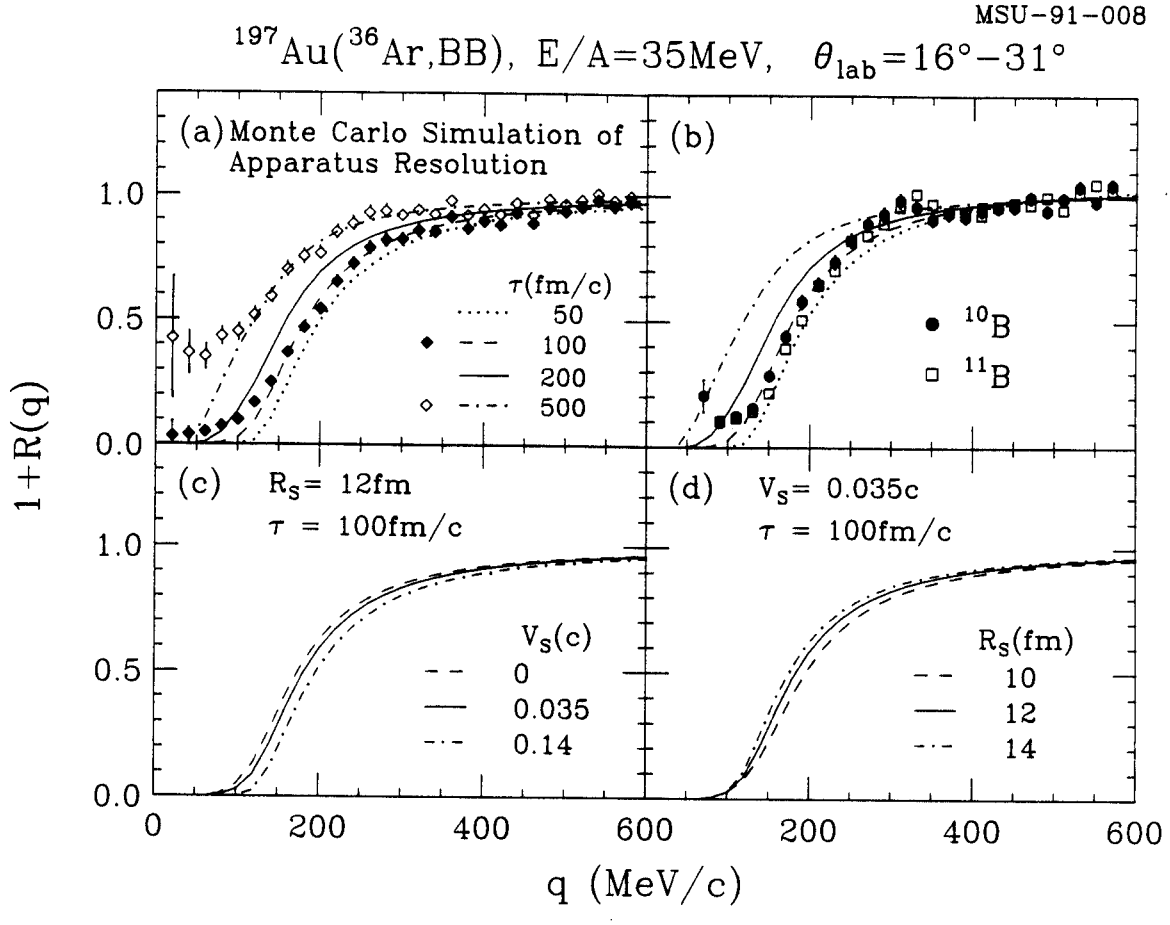

Figure 7.2 Estimates of experimental and theoretical uncertainties; a detailed discussion is given in the text.

was included. In Figure 7.3a, the results of these calculations (curves) are compared to the inclusive C-C correlation function (points). The three-body Coulomb trajectory calculations predict wider minima in the correlation functions than the calculations based upon Eq. 6.17, and the agreement with the data is slightly worse. Nevertheless, the calculations are in fair agreement with the experimental correlation functions for emission times of the order of 100-200 fm/c. In Figure 7.3b, we compare calculations for τ=200 fm/c. The curve shows the calculation with Eq. 6.17 and the solid points show the results of the three-body trajectory calculation. The discrepancy between the two model calculations is largely caused by dynamical correlations caused by the recoil of the heavy reaction residue which is included in the trajectory calculation, but not in Eq. 6.17. Indeed, the calculation with Eq. 6.17 is in rather good agreement with three-body calculations when the recoil of the heavy target residue is artificially reduced by increasing its mass to A_S=5000 while keeping its charge and radius constant (open points).

Shorter emission times appear to be indicated for the higher momentum cut (P/A> 150MeV/c). However, this observation is not conclusive due to poor statistics. By combining different fragment pairs of $4 \leq Z \leq 9$, we can gain an increase in statistical accuracy by a factor of about 20. This makes it possible to study the time scales in more detail by applying gates on the charged particle multiplicity and fragment energies.

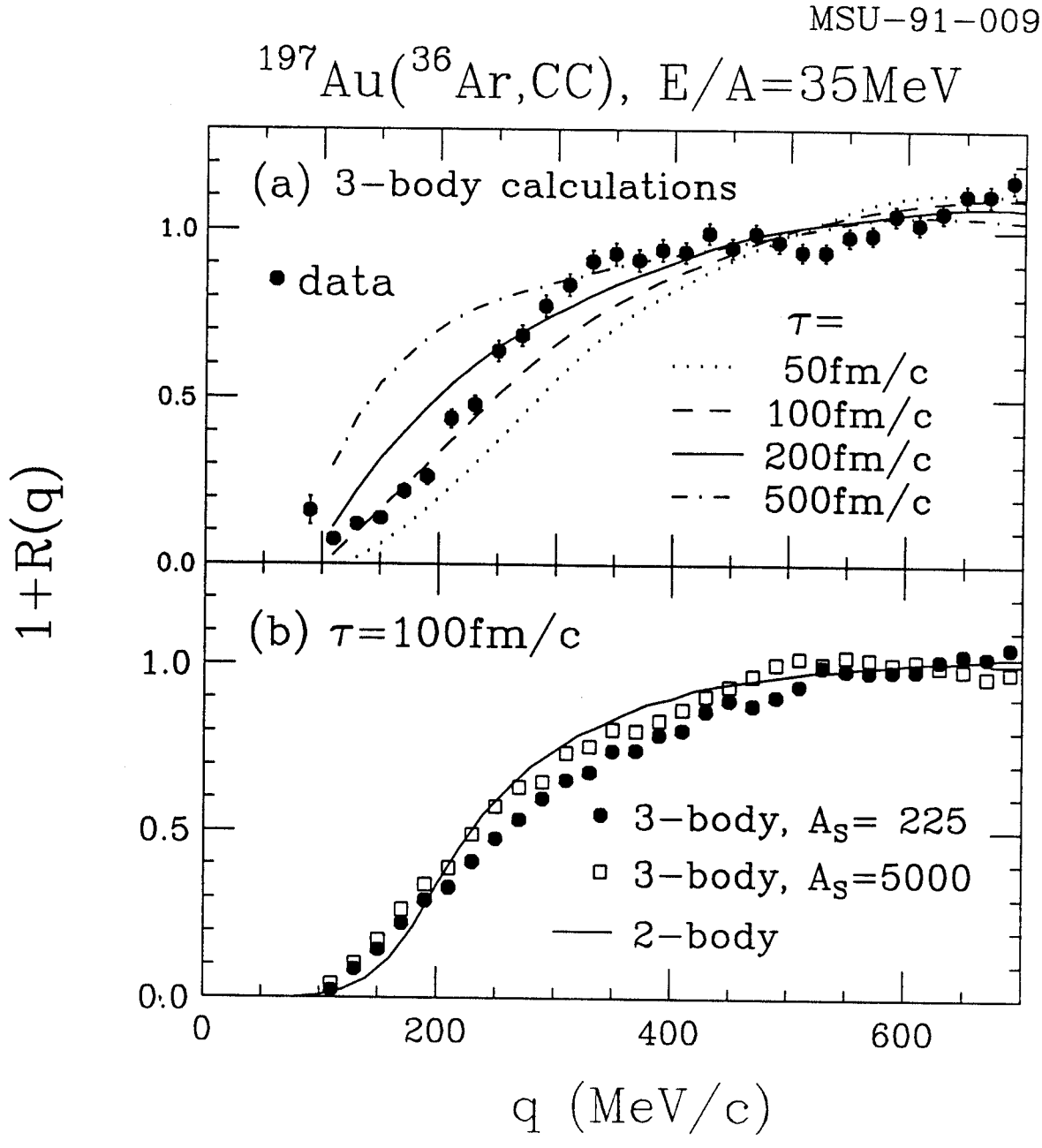

Figure 7.3 Panel (a): Comparison of inclusive C-C correlation functions to three-body Coulomb trajectory calculations. Panel (b): Correlation functions calculated from Eq. 2 (curve) and from three-body trajectory calculations (points).

7.2 Combinations of different fragment pairs

In Figure 7.4, we compare correlation functions for representative pairs of intermediate mass fragments alternatively as functions of relative momentum q (top panel) or as a functions of reduced relative velocity $v_{red} = v_{rel}/\sqrt{Z_1+Z_2}$ (bottom panel). Different symbols in the figure denote correlation functions evaluated for different fragment pairs (Z_1=6, and $4 \leq Z_2 \leq 9$). Since the Coulomb repulsion is greater between fragments of greater charge, the correlation functions, 1+R(q), exhibit wider minima at $q \approx 0$ for increased charge of the second fragment. When plotted as a function of v_{red}, however, the correlation functions $1+R(v_{red})$ are very similar. This suggests that correlation functions may be summed over different pair combinations and evaluated as a function of the reduced relative velocity with little loss in resolution. This "mixed-fragment" analysis permits the exploration of emission timescales with significantly improved statistical precision. In the following, we construct "mixed-fragment" correlation functions according to Eq. 6.2, where the sum is extended over all charge combinations with $4 \leq Z_1, Z_2 \leq 9$. Sufficient statistics is achieved via this summation to allow the exploration of emission timescales as functions of the charged-particle multiplicity and the velocity of the emitted fragments.

Our definition of the mixed-fragment correlation function differs slightly from that adopted in reference [Tro87] where two-fragment correlation functions were evaluated as a function of the relative fragment velocity. Figure 7.5 illustrates the difference between the two prescriptions. The top and bottom panels of the figure show correlation functions evaluated, for different fragment combinations with $4 \leq Z_1, Z_2 \leq 9$, as functions of relative and reduced relative velocities, v_{rel} and v_{red}, respectively. For this range of fragment charges, mixed-

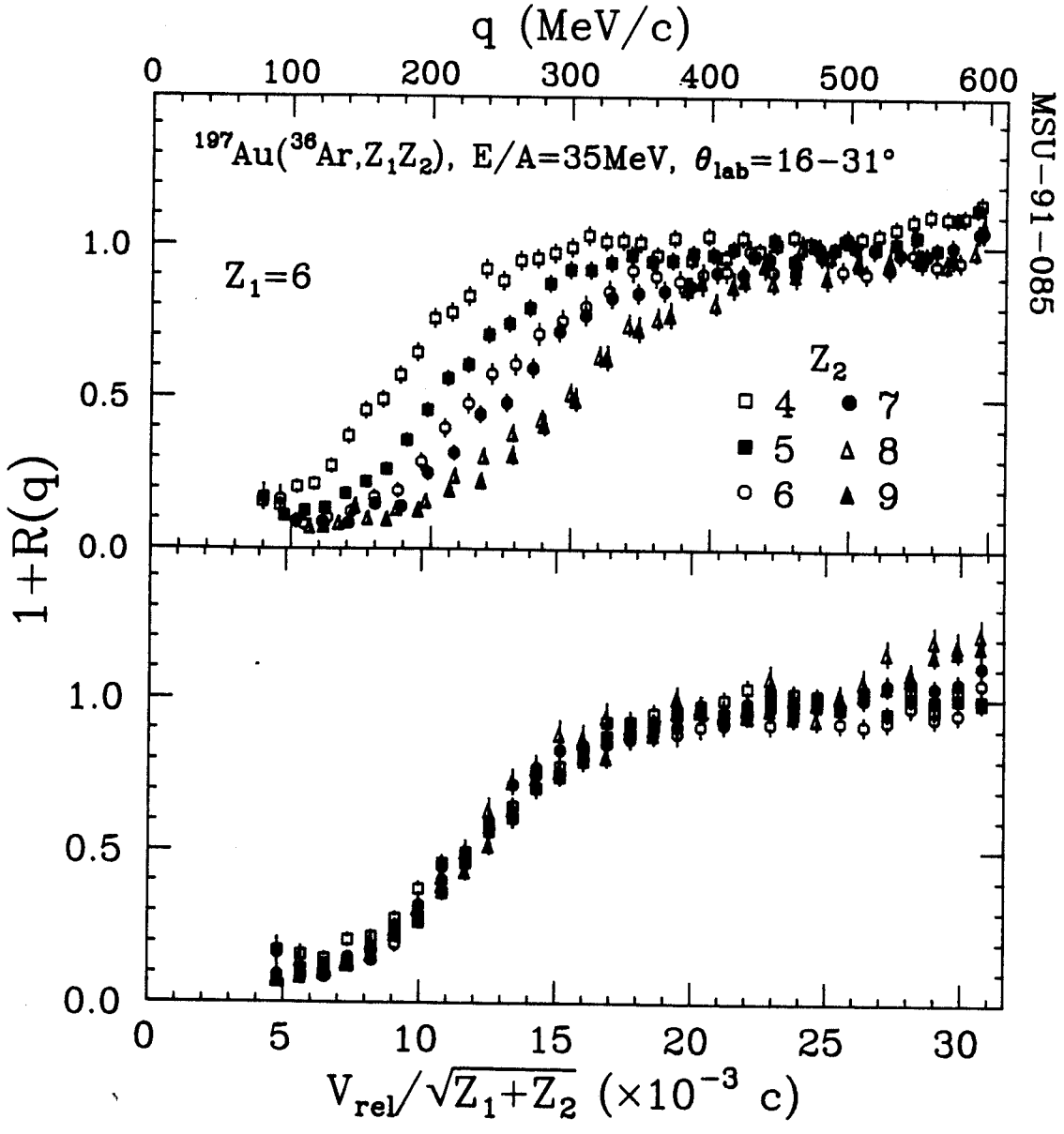

Figure 7.4 Dependence of inclusive, energy integrated two-fragment correlation functions on relative momentum q (top panel) and on reduced relative velocity $v_{rel}/\sqrt{Z_1+Z_2}$. One fragment was carbon (Z=6); the atomic number Z_2 of the other fragment is indicated.

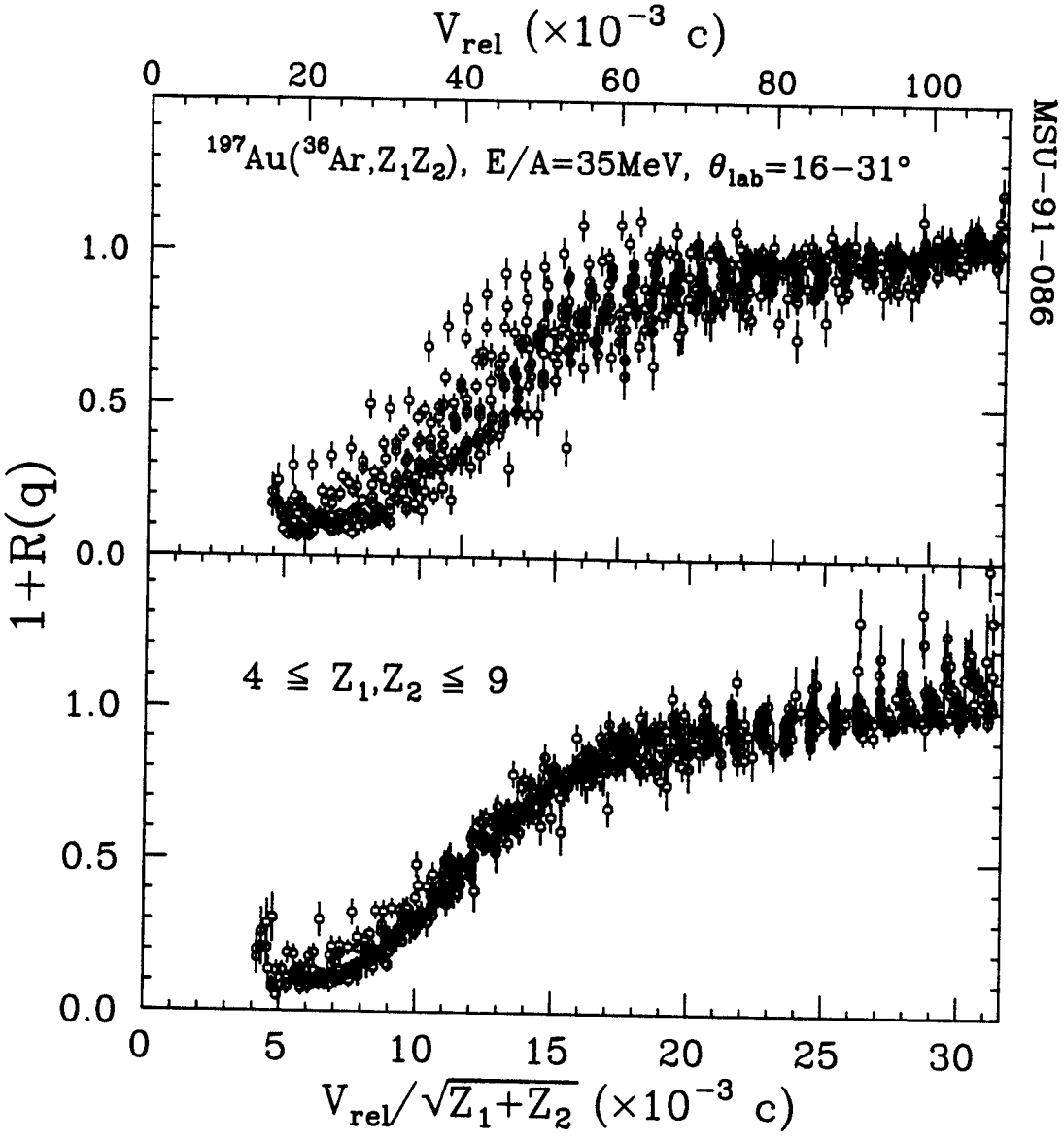

Figure 7.5 Dependence of inclusive, energy integrated two-fragment correlation functions on relative velocity v_{rel} (top panel) and on reduced relative velocity $v_{rel}/\sqrt{Z_1+Z_2}$ (bottom panel). Two-fragment correlation functions are shown for each combination of Z_1 and Z_2, with $4 \leq Z_1, Z_2 \leq 9$.

fragment correlation functions display superior resolution when they are evaluated as a function of the reduced relative velocity. Of course, the loss of resolution incurred for $1+R(v_{rel})$ can be incorporated into model calculations by performing corresponding averages [Tro87].

7.3 Gated correlation functions

Measured energy integrated two-fragment correlation functions, gated by various conditions on charged-particle and intermediate mass fragment multiplicities, are shown in Figure 7.6. The top and bottom panels show correlation functions gated by various conditions on charged-particle and IMF multiplicity, N_C and N_{IMF}, respectively. For orientation, we include calculations with the Koonin-Pratt formula, Eq. 6.17, for different emission times τ. Correlation functions measured for peripheral collisions or for events in which only two intermediate mass fragments were detected exhibit considerable distortions at larger reduced relative velocities. Since these distortions are not yet understood, they introduce slight uncertainties in the asymptotic normalization of the correlation functions. They become less significant for central collisions or for events in which at least four fragments are detected. The shapes of the energy integrated correlation functions depend only slightly on these multiplicity gates. The width of the minimum at $v_{red} \approx 0$ appears to decrease slightly as more central collisions (larger charged-particle multiplicities) are selected. This observation is qualitatively consistent with slightly longer time scales (or larger source dimensions) for fragments emitted in central as compared to peripheral collisions.

Central collisions are most important because they are better suited to study the properties of hot nuclear matter. Also they have the largest degree of

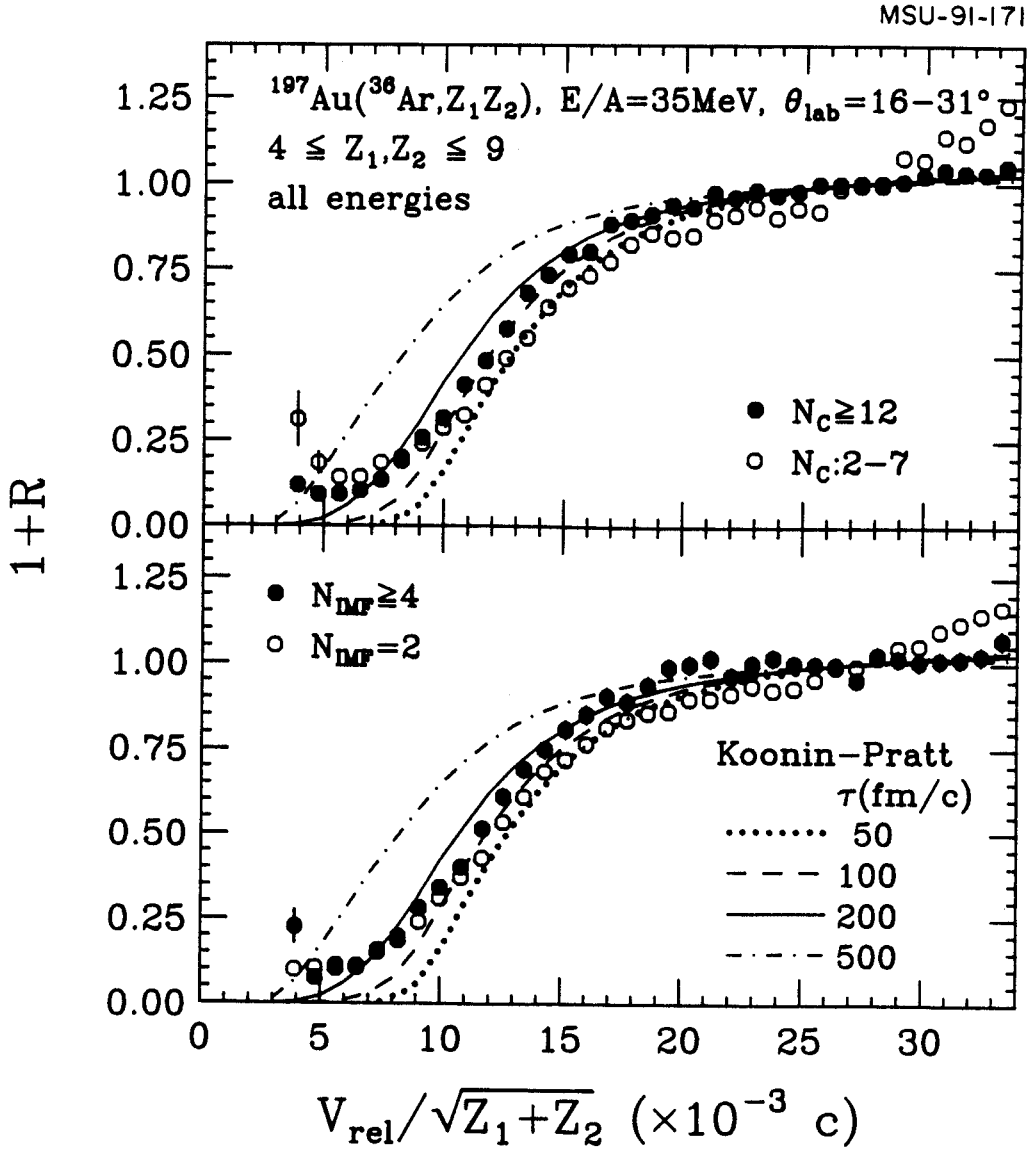

Figure 7.6 Two-fragment correlation functions summed over all combinations of Z_1 and Z_2 (with $4 \leq Z_1, Z_2 \leq 9$) and selected by the indicated gates on charged-particle multiplicity N_C (top panel) and on IMF multiplicity N_{IMF} (bottom panel).

equilibration according to energy spectra discussed in Section 6.4. For the remainder of our investigation, we will focus on correlation functions gated by central collisions.

Figure 7.7 depicts two-fragment correlation functions gated by central collisions ($N_C \geq 12$). In order to be able to study fragment emission time scales for different regions of the kinetic energy spectrum, we have evaluated the correlation functions for three different ranges of P/A, the total momentum per nucleon of the coincident fragment pair. The low momentum gate (P/A≤110 MeV/c: solid circular points) selects fragment kinetic energies at and below the exit channel Coulomb barrier. Kinetic energies slightly above the Coulomb barrier are selected by the intermediate momentum gate (P/A=110-120 MeV/c: open circular points). For these two gates, a considerable part of the emission cross section is consistent with equilibrium emission, see also Fig. 5.12. Kinetic energies significantly above the Coulomb barrier are selected by the high momentum gate (P/A≥140 MeV/c: solid square-shaped points). In this domain, fragment emission for central collisions is dominated by nonequilibrium emission processes different from projectile fragmentation. The experimental correlation functions exhibit a rather pronounced dependence on the total momentum per nucleon of the emitted fragment pairs. The minimum at $v_{red} \approx 0$ becomes considerably wider as the gate on P/A is raised from below 110 MeV/c to above 140 MeV/c. Since wider minima are indicative of smaller space-time dimensions, this observation is qualitatively consistent with the expectation that mean emission times should become shorter as the kinetic energy of the emitted fragment is raised from close to the Coulomb barrier to much higher values.

In Figure 7.8, the measured inclusive two-fragment correlation functions are compared to correlation functions calculated for the indicated emission times τ. Calculations with the Koonin-Pratt formula, Eq. 6.17, are presented in the top

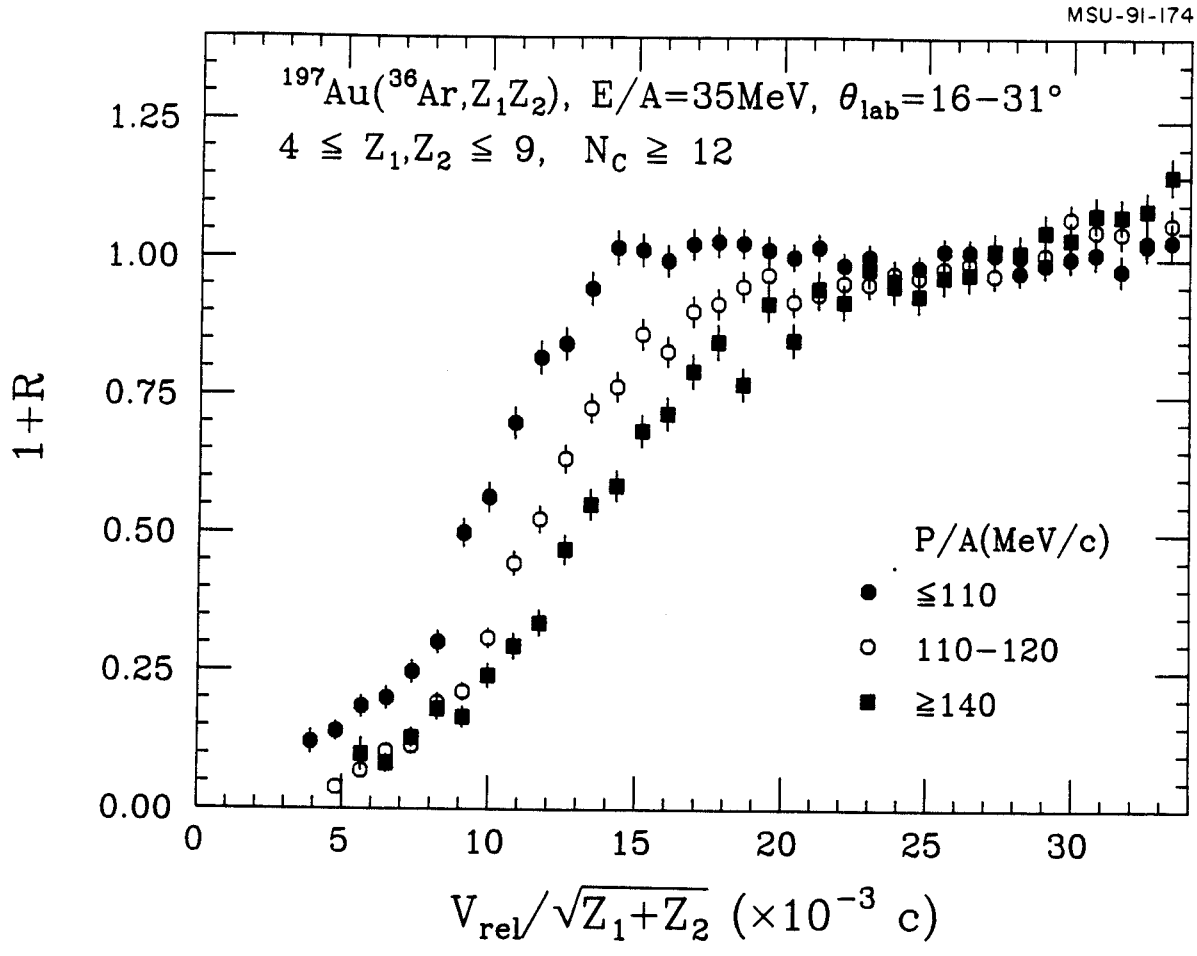

Figure 7.7 Two-fragment correlation functions summed over all combinations of Z_1 and Z_2 (with $4 \leq Z_1,Z_2 \leq 9$) and selected by central collisions ($N_C \geq 12$). The correlation functions are evaluated for the indicated ranges of P/A, the total momentum per nucleon of the detected fragment pair.

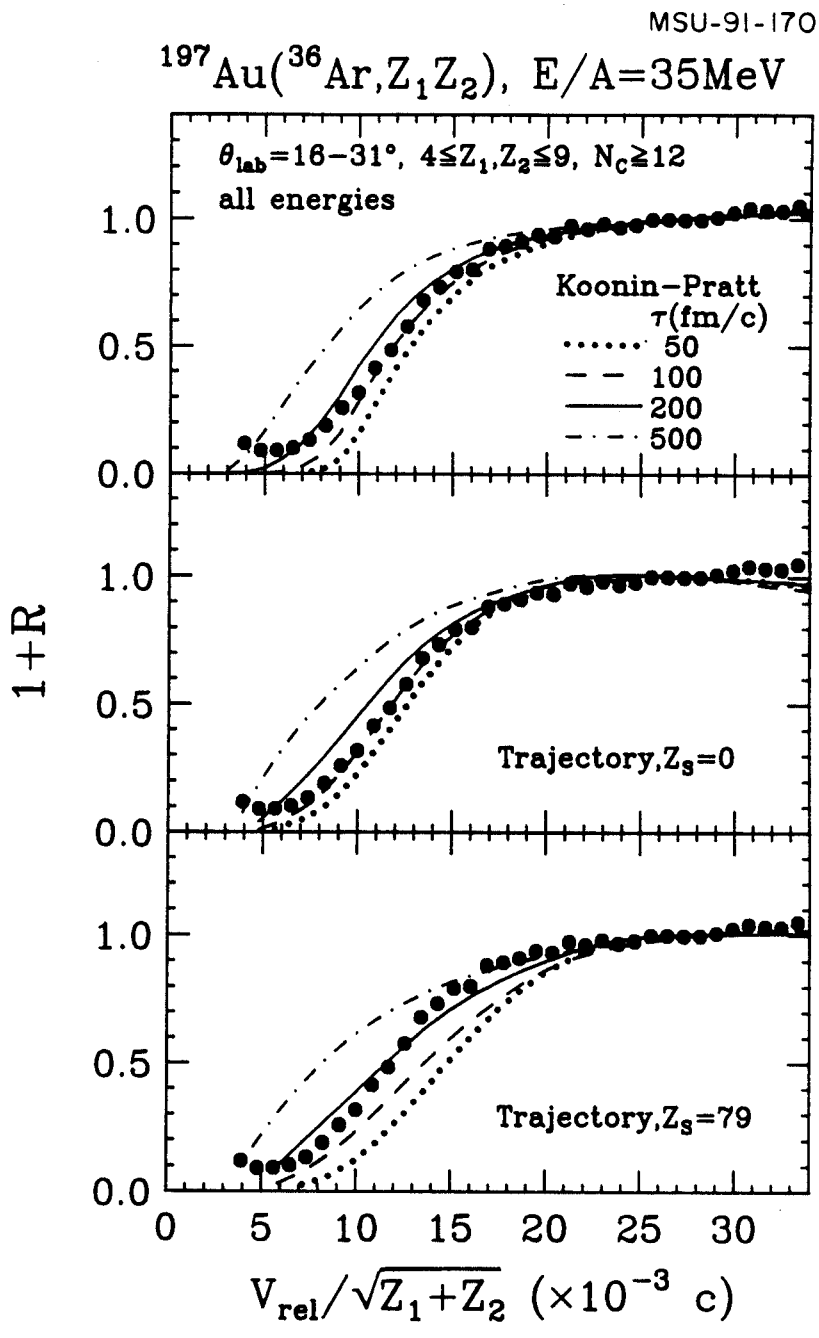

Figure 7.8 Inclusive, energy integrated two-fragment correlation functions summed over all combinations of Z_1 and Z_2 (with $4 \leq Z_1, Z_2 \leq 9$). The different panels give comparisons with different calculations discussed in the text.

panel; the center and bottom panels show the results of numerical trajectory calculations for Z_S=0 and 79, respectively. Calculations neglecting Coulomb interactions with the residual system (upper and center panels) predict shapes of correlation functions which are in slightly better agreement with the experimental correlation functions than the three-body calculations incorporating distortions in the field of a heavy reaction residue (bottom panel). Slightly smaller emission times are indicated by calculations with the Koonin-Pratt formula and by the Z_S=0 calculations than by the three-charged-body trajectory-calculations. Nevertheless, all calculations are consistent with emission times between τ=100-200 fm/c, in agreement with the results from equal-charge correlation functions.

Calculations for correlation functions measured for central collisions and for different cuts on P/A, the total momenta per nucleon of the coincident fragments pairs, are presented in Figures 7.9-11. Individual panels of these figures depict results for the indicated cuts on P/A. Figures 7.9, 7.10, and 7.11 present calculations for different emission times using the Koonin-Pratt formula, and trajectory calculations for Z_S=0 and Z_S=79, respectively. For the case Z_S=79, three-body trajectory calculations could only be performed for the two higher momentum cuts, P/A=110-120 MeV/c and P/A$\geq$140 MeV/c, as the cut P/A$\leq$110 MeV/c selects mostly energies below the Coulomb barrier. For clarity and consistency, we refrained from lowering the exit channel Coulomb barrier which would require a significant increase in source radius or a significant decrease of the source charge. Either of these parameter modifications would reduce Coulomb distortions and, hence, differences with the Koonin-Pratt and Z_S=0 calculations.

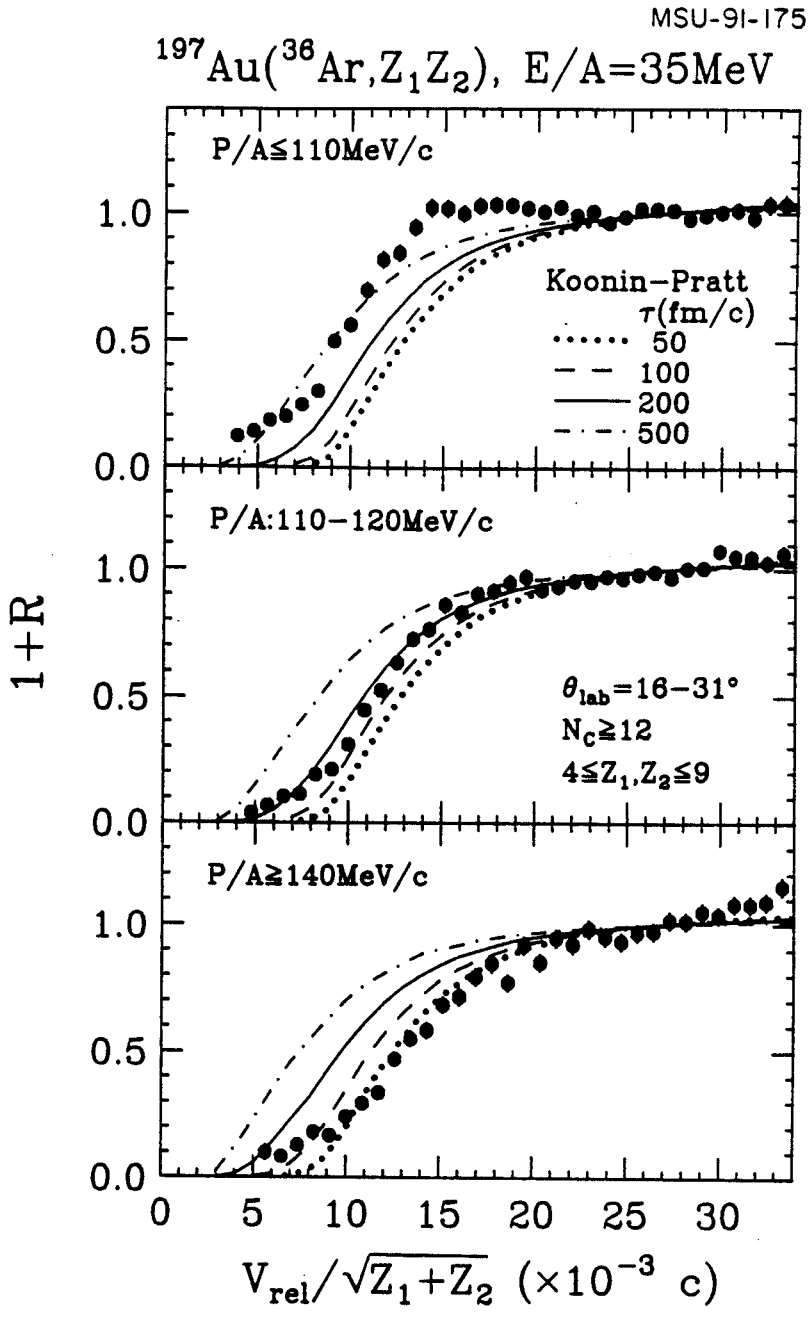

Figure 7.9 Two-fragment correlation functions summed over all combinations of Z_1 and Z_2 (with $4 \leq Z_1, Z_2 \leq 9$) and selected by central collisions ($N_C \geq 12$). Individual panels show the correlation functions for the indicated cuts on P/A, the total momentum per nucleon of the detected fragment pair. The curves represent calculations with the Koonin-Pratt formula for the indicated emission times.

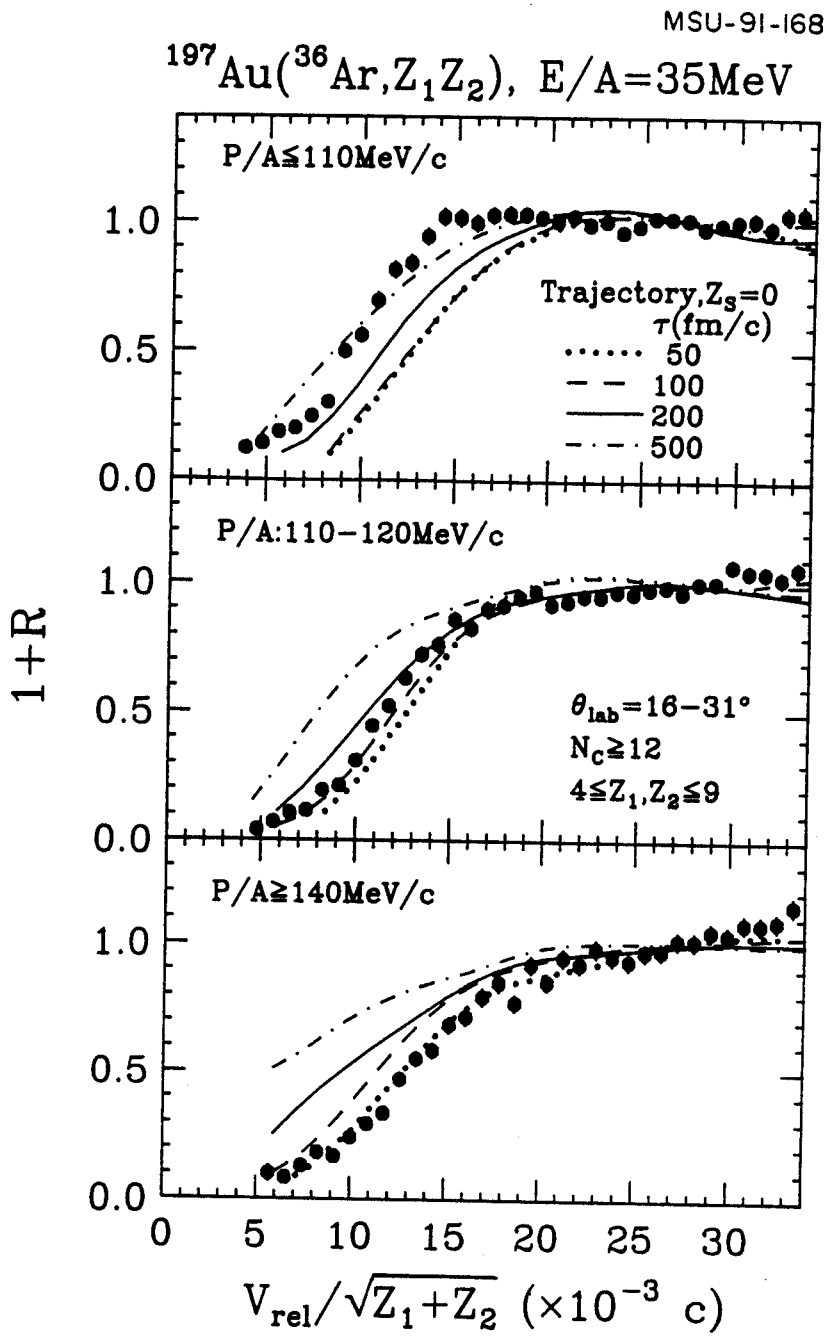

Figure 7.10 Two-fragment correlation functions summed over all combinations of Z_1 and Z_2 (with $4 \leq Z_1, Z_2 \leq 9$) and selected by central collisions ($N_C \geq 12$). Individual panels show the correlation functions for the indicated cuts on P/A, the total momentum per nucleon of the detected fragment pair. The curves represent the results of trajectory calculations for which the Coulomb interaction with the residual system is turned off. The key for emission times is given in the figure.

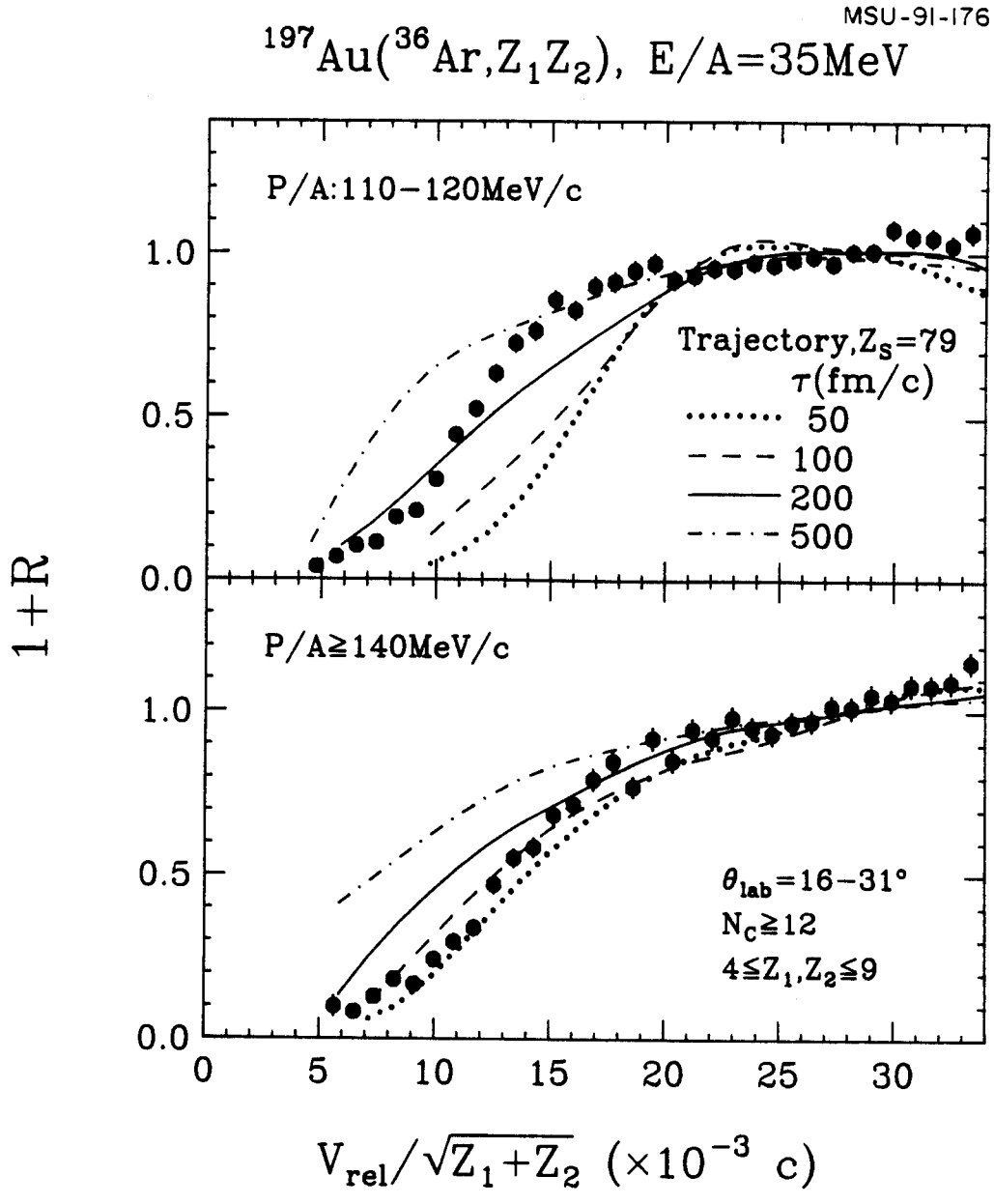

Figure 7.11 Two-fragment correlation functions summed over all combinations of Z_1 and Z_2 (with $4 \leq Z_1, Z_2 \leq 9$) and selected by central collisions ($N_C \geq 12$). Individual panels show the correlation functions for the indicated cuts on P/A, the total momentum per nucleon of the detected fragment pair. The curves represent the results of three-body Coulomb trajectory calculations in which the two fragments are assumed to be emitted from a source of initial charge number Z_S=79. The key for emission times is given in the figure.

For all three approximations investigated, comparisons between theoretical and experimental correlation functions lead to qualitatively similar conclusions: The emission of energetic fragments is governed by significantly smaller time scales than the emission of low-energy fragments with energies close to the exit channel Coulomb barrier. Such a dependence is consistent with the predominance of nonequilibrium emission processes for energetic fragment emissions and the increasing importance of emission from more equilibrated systems for particles emitted with energies close to the Coulomb barrier, see also Fig. 5.11. As was already observed for the inclusive correlation functions, calculations with the Koonin-Pratt formula and those for Z_S=0 predict shapes of correlation functions which are in better agreement with the experimental data than those predicted by three-body trajectory calculations. These former calculations indicate emission times of $\tau \lesssim 50$ fm/c for the emission of energetic fragments selected by P/A≥140 MeV/c and considerably larger emission times, $\tau \approx 500$ fm/c, for subbarier emission selected by P/A≤110 MeV/c. Emission times extracted for P/A=110-120 MeV/c are of the order of $\tau \approx 150$ fm/c. Qualitatively similar conclusions are drawn from a comparison with the three-body trajectory calculations for Z_S=79.

Emission time scales of the order of several hundred fm/c are consistent with time scales expected from statistical models of compound nuclear decays. For example, the model of reference [Fri90] predicts average time intervals of $\tau \approx 300$ fm/c between the emission of two carbon fragments from equilibrated heavy nuclei (A=226, Z=93) of 700 MeV excitation energy. Much shorter time scales, $\tau \approx 50$-100 fm/c, extracted for the emission of energetic fragments in central collisions, are incompatible with statistical emission from fully equilibrated heavy reaction residues. These emission times are of comparable

magnitude as those predicted [Aic88a,Aic88b,Pei89] by dynamical models of fragment production.

Chapter 8 Summary

In this thesis we addressed the questions related to multi-fragment emission. Theoretical studies show the sensitivity of the probability of multi-fragment breakup to the nuclear equation of state at low density. We tried to measure the multi-fragment emission at intermediate energy nucleus-nucleus collisions and characterize the reaction mechanism by studing the global observables and time scales of the fragment emission processes.

We have measured the relation between fission fragment folding angles and total charged particle multiplicities for the reactions $^{14}N+^{238}U$ at E/A=50 MeV and $^{36}Ar+^{238}U$ at E/A= 20 and 35 MeV. The mean values of these two quantities exhibit a monotonic relation. Both reaction filters have finite resolution due to the statistical nature of the decay processes, yet is is possible to distinguish central, large momentum transfer collisions from peripheral, small momentum transfer collisions by gates on very high ($M \geq 12$) or very low ($M=1$) multiplicity, respectively. Less extreme multiplicity gates, however, are less selective and do not result in cleanly separated momentum transfer distributions. Rather broad momentum transfer distributions are observed, for example, at intermediate multiplicities. In contrast to the total multiplicity or the multiplicity of charged particles emitted to backward angles, practically no selectivity was observed for a reaction filter utilizing the number of charged particles emitted to forward angles, $\theta<35°$. At least for the present reactions, the multiplicities in such forward arrays cannot be used to select violent projectile-target interactions in which large amounts of energy and/or momentum are dissipated.

We also established the occurrence of multi-fragment emission processes. Single and multiple emissions of intermediate mass fragments to large angles ($\Theta \geq 35°$) occur essentially in reactions characterized by large associated charged particle multiplicities and large linear momentum transfers to the heavy reaction residues. The measured fragment multiplicity distributions are well described by Poisson distributions consistent with a stochastic IMF production process. Final states with only one intermediate mass fragment in the exit channel represent only one of a family of final states.

We successfully constructed a low-threshold charged-particle detector array with high granularity and good particle identification, the MSU Miniball. With this device, we studied the emission of intermediate mass fragments in collisions between ^{36}Ar projectiles and ^{197}Au target nuclei at E/A=35 MeV. Intermediate mass fragments are preferentially emitted in violent central collisions characterized by large charged-particle multiplicities N_C. In peripheral collisions, fragment emission is a fairly unlikely process; the average IMF multiplicity increases from $\langle N_{IMF} \rangle \lesssim 0.1$ for $N_C = 2$ to $\langle N_{IMF} \rangle \approx 1.2$ for $N_C \gtrsim 15$. The elemental distributions observed for various cuts on charged-particle multiplicity exhibit a nearly exponential fall-off as a function of Z. In this reaction, the inclusive element distributions are rather similar to those observed in central collisions. The exponential fall-off is only slightly steeper for fragments produced in peripheral collisions than for fragments produced in central collisions. The angular distributions of fragments produced in peripheral collisions are steeper than those of fragments produced in central collisions. At forward angles, the energy spectra of fragments produced in peripheral collisions exhibit a high-energy shoulder which could be attributed to emission from a projectile-like source. Such a shoulder is not observed in energy spectra

gated on central collisions, for which the spectra exhibit nearly exponential shapes.

A detailed analysis of the energy and angular distributions of fragments emitted in central collisions (gated by $N_C \geq 12$) reveals important contributions from processes incompatible with emission from equilibrated sources. These contributions dominate for fragments emitted at forward angles and with kinetic energies well above the exit channel Coulomb barrier. Emission with kinetic energies close to the Coulomb barrier and at larger angles is consistent with increasing contributions from the decay of equilibrated heavy reaction residues.

The granularity of the apparatus and the statistics of two-fragment coincidences allowed the generation of good quality two-fragment correlation functions in the angular range of $16^\circ \leq \theta_{lab} \leq 31^\circ$. The two-fragment correlation function was found to depend mainly on the reduced relative velocity of the fragment pairs. This scaling allows the construction of mixed-fragment correlation functions with little loss in resolution and significantly improved statistics thus allowing a detailed investigation of two-fragment correlation functions for different multiplicity cuts and different ranges of fragment velocities. Average emission time scales of τ=100-200 fm/c were extracted from the Be-Be, B-B, and C-C correlation functions and inclusive, mixed-fragment correlation functions. These mean emission times are shorter than those extracted previously [Tro87,Bou89] for reactions induced by lighter projectiles. Only modest dependences were observed for various cuts on charged-particle or IMF multiplicity. These dependences were qualitatively consistent with slightly larger space-time dimensions for central than for peripheral collisions.

In order to suppress contributions from the decay of projectile-like residues, we constructed two-fragment correlation functions for central collisions (gated by $N_C \geq 12$). We explored various cuts on P/A, the total momentum per nucleon of

the emitted fragment pair, which select different ranges of fragment velocities and, hence, different relative contributions from equilibrium and nonequilibrium emission. The observed dependence on P/A indicated significant differences in emission time scales. In order to extract fragment emission times, we assumed, for simplicity, emission from the surface of a spherical source of 12 fm radius. For the most energetic fragments, the correlation functions were consistent with mean emission times of $\tau<100$ fm/c, possibly as short as $\tau\approx50$ fm/c. For fragments emitted with kinetic energies at or below the exit channel Coulomb barrier, the correlation functions indicate much longer emission time scales, $\tau\gtrsim300$ fm/c, possibly as large as $\tau\approx500$ fm/c. For comparison, average emission times predicted for the decay of equilibrated fusion residues are of the order of 300 fm/c; dynamical models of fragment production predict emission time scales on the order of 50 fm/c.

The shape of the fragment energy spectra and the emission time scales extracted from two-fragment correlation functions indicates that fragment emission in central collisions begins at the very early stages of the reaction and continues throughout the later equilibrated stages. Thus, realistic models of fragment production must strive to describe the competition between light particle and IMF emission from the early, possibly compressed stages of the reaction, to the later, equilibrated and possibly expanded stages.

LIST OF REFERENCES

LIST OF REFERENCES

[Aic88] J. Aichelin, G. Peilert, A. Bohnet, A. Rosenhauer, H. Stöcker, and W. Greiner, Nucl. Phys. A488, 437c (1988).

[Aic88] J. Aichelin, G. Peilert, A. Bohnet, A. Rosenhauer, H. Stöcker, and W. Greiner, Phys. Rev. C37, 2451 (1988).

[Ala86] J. Alarja, A. Dauchy, A. Giorni, C. Morand, E. Pollaco, P. Stassi, B. Billerey, B. Chambon, B. Cheynis, D. Drain, and C. Pastor, Nucl. Instr. and Meth. A242 (1986) 352.

[Ard89] D. Ardouin, F. Guilbault, C. Lebrun, D. Ardouin, S. Pratt, P. Lautridou, R. Boisgard, J. Québert, and A. Péghaire, University of Nantes, Internal Report LPN-89-02.

[Bad82] A. Baden, H.H. Gutbrod, H. Löhner, M.R. Maier, A.M. Poskanzer, T. Renner, H. Riedesel, H.G. Ritter, H. Spieler, A. Warwick, F. Weik, and H. Wieman, Nucl. Inst. and Meth. A203, 189 (1982).

[Ban85] Sa Ban-Hao and D.H.E. Gross, Nucl. Phys. A437, 643 (1985).

[Bar81] A.R. Barnett, Computer Physics Communications 21, 297 (1981).

[Bar86] C. Barbagallo, J. Richert, and P. Wagner, Z. Phys. A324, 97 (1986).

[Bar90] H.W. Barz, J.P. Bondorf, K. Sneppen, and H. Schulz, Phys. Lett. B244, 161 (1990).

[Bau86] W. Bauer, U. Post, D.R. Dean, and U. Mosel, Nucl. Phys. A452, 699 (1986).

[Bau87] W. Bauer, G.F. Bertsch, and S. Das Gupta, Phys. Rev. Lett. 58, 863 (1987).

[Bau88] W. Bauer, Phys. Rev. C38, 1297 (1988).

[Ben89] F. Benrachi, B. Chambon, B. Cheynis, D. Drain, C. Pastor, D. Seghier, K. Zaid, A. Giorni, D. Heuer, A. Lleres, C. Morand, P. Stassi, and J.B. Viano, Nucl. Instr. and Meth., A281, 137 (1989).

[Ber81] G. Bertsch and J. Cugnon, Phys. Rev. C24, 2514 (1981).

[Ber83] G. Bertsch and P.J. Siemens, Phys. Lett. 126B, 9 (1983).

[Bic90] "Bicron", Bicron (1990).

[Big61] J.A. Biggerstaff, R.L. Becker, and M.T. McEllistrem, Nucl. Instr. and Meth. 10 (1961) 327.

[Bir64] J.B. Birks, The theory and practice of scinitllation counting (Pergamon Press, New York, 1964), p. 92.

[Biz86] G. Bizard, A. Drouet, F. Lefebvres, J.P. Patry, B. Tamain, F. Guilbault, and C. lebrun, Nucl. Instr. and Meth. A244, 483 (1986).

[Blu91] Y. Blumenfeld, N. Colonna, P. Roussel-Chomaz, D.N. Delis, K. Hanold, J.C. Meng, G.F. Peaslee, G.J. Wozniak, L.G. Moretto, B. Libby, G. Guarino, N. Santoruvo, and I. Iori, Phys. Rev. Lett. 66, 576 (1991).

[Boa86] D.H. Boal and A.L. Goodman, Phys. Rev. C33, 1690 (1986).

[Boa88] D.H. Boal and J.N. Glosli, Phys. Rev. C37, 91 (1988).

[Boa90a] D.H. Boal and J. Glosli, Phys. Rev. C42, R502 (1990).

[Boa90b] D.H. Boal, C.K. Gelbke, and B.K. Jennings, Rev. Mod. Phys. 62, 553 (1990).

[Bon85a] J.P. Bondorf, R. Donangelo, I.N. Mishustin, C.J. Pethick, H. Schulz, and K. Sneppen, Nucl. Phys. A443, 321 (1985).

[Bon85b] J.P. Bondorf, R. Donangelo, I.N. Mishustin, and H. Schulz, Nucl. Phys. A444, 460 (1985).

[Bon85c] J.P. Bondorf, R. Donangelo, I.N. Mishustin, C.J. Pethick, and K. Sneppen, Phys. Lett. 150B, 57 (1985);

[Bon85d] J.P. Bondorf, R. Donangelo, H. Schulz, and K. Sneppen, Phys. Lett. 162B, 30 (1985).

[Bor88] B. Borderie, M. Montoya, M.F. Rivet, D. Jouan, C. Cabot, H. Fuchs, D. Gardes, H. Gauvin, D. Jacquet, F. Monnet, and F. Hanappe, Phys. Lett. B205, 26 (1988).

[Bou87] R. Bougault, J. Duchon, J.M. Gautier, A. Genoux-Lubain, C. LeBrun, J.F. Lecolley, F. Lefebvres, M. Louvel, P. Mosrin, and R. Regimbart, Nucl. Instr. and Meth. A259, 473 (1987).

[Bou88] R. Bougault, F. Delaunay, A. Genoux-Lubain, C. LeBrun, J.F. Lecolley, F. Lefebvres, M. Louvel, J.C. Steckmeyer, J.C. Adloff, B. Bilwes, R. Bilwes, M. Glaser, G. Rudolf, F. Scheibling, L. Stuttge, and J.L. Ferrero, Nucl., Phys. A488 255c (1988)

[Bou89] R. Bougault, J. Colin, F. Delaunay, A. Genoux-Lubain, A. Hajfani, C. LeBrun, J.F. Lecolley, M. Louvel, J.C. Steckmeyer, Phys, Lett. B232, 291 (1989)

[Bow87] D.R. Bowman, W.L. Kehoe, R.J. Charity, M.A. McMahan, A. Moroni, A. Bracco, S. Bradley, I. Iori, R.J. McDonald, A.C. Mignerey, L.G. Moretto, M.N. Namboodiri, and G.J. Wozniak, Phys. Lett. B189, 282 (1987).

[Bre77] A. Breskin and N. Zwang, Nucl. Instr. and Meth. A146, 461 (1977).

[Bre84] A. Breskin, R. Chechik, Z. Fraenkel, P. Jacobs, I. Tserruya, and N. Zwang, Nucl. Instr. and Meth. A221, 363 (1984).

[Bric65] .C. Brice, The Growth of Crystals from the Melt, North Holland, Amsterdam (1965).

[Brid25] P.W. Bridgman, Proc. Amer. Acad. Arts. Sci. 60, 305 (1925).

[Cam88] X. Campi, Phys. Lett. B208, 351 (1988).

[Cas89] Y. Cassagnou et al., Proceedings of the Symposium on Nuclear Dynamics and Nuclear Disassembly, held at Dallas, Texas, April 1989, edited by J. Natowitz, World Scientific, Singapore 1989, p. 386.

[Cav90] C. Cavata, M. Demoulins, J. Gosset, M.C. Lemaire, D. L'Hôte, J. Poitou, and O. Valette, Phys. Rev. C42, 1760 (1990).

[Cha88] R.J. Charity, M.A. McMahan, G.J. Wozniak, R.J. McDonald, L.G. Moretto, D.G. Sarantides, L.G. Sobotka, G. Guarino, A. Pantaleo, L. Fiore, A. Gobbi, and K.D. Hildenbrand, Nucl. Phys. A483, 371 (1988).

[Che87] Z. Chen C.K. Gelbke, J. Pochodzalla, C.B. Chitwood, D.J. Fields, W.G. Gong, W.G. Lynch, and M.B. Tsang, Nucl. Phys. A473 (1987) 564.

[Chi83] C.B. Chitwood, D.J. Fields, C.K. Gelbke, W.G. Lynch, A.D. Panagiotou, M.B. Tsang, H. Utsunomiya and W.A. Friedman, Phys. Lett. 131B, 289 (1983).

[Chi86] C.B. Chitwood, D.J. Fields, C.K. Gelbke, D.R. Klesch, W.G. Lynch, M.B. Tsang, T.C. Awes, R.L. Ferguson, F.E. Obenshain, F. Plasil, R.L. Robinson, and G.R. Young, Phys. Rev. C34, 858 (1986).

[Cse86] L.P. Csernai and J.I. Kapusta, Phys. Rep. 131, 223 (1986).

[Czo18] J. Czochralski, Z. Phys. Chem. 92, 29 (1918).

[Dan79] P. Danielewicz, Nucl. Phys., A314, 465 (1979).

[Dan85] P. Danielewicz and G. Odyniec, Phys. Lett. B157, 146 (1985).

[DeY89] P.A. DeYoung, M.S. Gordon, Xiu qin Lu, R.L. McGrath, J.M. Alexander, D.M. de Castro Rizzo, and L.C. Vaz, Phys. Rev. C39, 128 (1989).

[DeY90] P.A. DeYoung, C.J. Gelderloos, D. Kortering, J. Sarafa, K. Zienert, M.S. Gordon, B.J. Fineman, G.P. Gilfoyle, X. Lu, R.L. McGrath, D.M. de Castro Rizzo, J.M. Alexander, G. Auger, S. Kox, L.C. Vaz, C. Beck,

D.J. Henderson, D.G. Kovar, and M.F. Vineyard, Phys. Rev. C41, R1885 (1990).

[Din62] A. Dinsdale and F. Moore, Viscosity and its Measurement (Chapman-Hill, London, 1962).

[Don89] R. Donangelo, K. Sneppen, and J.P. Bondorf, Phys. Lett. B219, 165 (1989).

[Dos85] K.G.R. Doss, H.Å. Gustafsson, H.H. Gutbrod, B Kolb, H. Löhner, B. Ludewigt, A.M. Poskanzer, T. Renner, H. Riedesel, H.G. Ritter, A. Warwick, and H. Wieman, Phys. Rev. C32, 116 (1985).

[Dos87] K.G.R. Doss, H.A. Gustafsson, H. Gutbrod, J.W. Harris, B.V. Jacak, K.H. Kampert, A.M. Poskanzer, H.G. Ritter, H.R. Schmidt, L. Teitelbaum, M. Tincknell, S. Weiss, and H. Wieman, Phys. Rev. Lett. 59, 2720 (1987).

[Dra89] D. Drain, A. Giorni, D. Hilscher, C. Ristori, J. Alarja, G. Barbier, R. Bertholet, R. Billerey, B. Chambon, B. Cheynis,, J. Crançon, A. Dauchy, P. Désesquelles, A. Fontenille, L. Guyon, D. Heuer, A. Llères, M. Maurel, E. Monnand, H. Nifenecker, C. Pastor, J. Pouxe, H. Rossner, J. Saint-Martin, F. Schussler, P. Stassi, M. Tournier, and J.B. Viano, Nucl. Instr. and Meth. A281 (1989) 528.

[Fai82] G. Fai and J. Randrup, Nucl. Phys. A381, 557 (1982).

[Fai82] G. Fai and J. Randrup, Phys. Lett. 115B, 281 (1982).

[Fai83] G. Fai and J. Randrup, Nucl. Phys. A404, 281 (1983).

[Fat85] M. Fatyga, K. Kwiatkowski, V.E. Viola, C.B. Chitwood, D.J. Fields, C.K. Gelbke, W.G. Lynch, J. Pochodzalla, M.B. Tsang, and M. Blann, Phys. Rev. Lett. 55, 1376 (1985).

[Fat87] M. Fatyga, K. Kwiatkowski, V.E. Viola, W.G. Wilson, M.B. Tsang, J. Pochodzalla, W.G. Lynch, C.K. Gelbke, D.J. Fields, C.B. Chitwood, Z. Chen, and T. Nayak, Phys. Rev. Lett. 58, 2527 (1987).

[FieE89] D.E. Fields, K. Kwiatkowski, D. Bonser, R.W. Viola, V.E. Viola, W.G. Lynch, J. Pochodzalla, M.B. Tsang, C.K. Gelbke, D.J. Fields, and S.M. Austin, Phys. Lett. B220, 356 (1989).

[FieJ84] D.J. Fields, W.G. Lynch, C.B. Chitwood, C.K. Gelbke, M.B. Tsang, H. Utsunomiya and J. Aichelin, Phys. Rev. C30, 1912 (1984).

[FieJ86] D.J. Fields, W.G. Lynch, T.K. Nayak, M.B. Tsang, C.B. Chitwood, C.K. Gelbke, R. Morse, J. Wilczynski, T.C. Awes, R.L. Ferguson, F. PLasil, F.E. Obenshain, and G.R. Young, Phys. Rev. C34, 536 (1986).

[Fin82] J.E. Finn, S. Agarwal, A. Bujak, J. Chuang, L.J. Gutay, A.S. Hirsch, R.W. Minich, N.T. Porile, R.P. Scharenberg, B.C. Stringfellow, and F. Turkot, Phys. Rev. Lett. 49, 1321 (1982).

[Fis67] M.E. Fisher, Physics 3, 255 (1967).

[Fri83] W.A. Friedman and W.G. Lynch, Phys. Rev. C28, 950 (1983).

[Fri88] W.A. Friedman, Phys. Rev. Lett. 60, 2125 (1988).

[Fri89] W.A. Friedman, Phys. Rev. C40, 2055 (1989).

[Fri90] W.A. Friedman, Phys. Rev. C42, 667 (1990).

[Gal85] J. Galin, Nucl. Phys. A447 (1985) 519c.

[Gel87] C.K. Gelbke and D.H. Boal, Prog. in Part. and Nucl. Phys. 19, 33 (1987).

[Gol80] H. Goldstein, "Classical Mechanics", 2nd edition, Addison-Wesley, p102, 1980.

[Gon88] W.G. Gong, Y.D. Kim, G. Poggi, Z. Chen, C.K. Gelbke, W.G. Lynch, M.R. Maier, T. Murakami, M.B. Tsang, H.M. Xu, and K. Kwiatkowski, Nucl. Instr. and Meth. A268 (1988) 190.

[Gon90a] W.G. Gong, C.K. Gelbke, N. Carlin, R.T. de Souza, Y.D. Kim, W.G. Lynch, T. Murakami, G. Poggi, D. Sanderson, M.B. Tsang, H.M. Xu, D.E. Fields, K. Kwiatkowski, R. Planeta, V.E. Viola, Jr., S.J. Yennello, and S. Pratt, Phys. Lett. B246, 21 (1990).

[Gon90b] W.G. Gong, W. Bauer, C.K. Gelbke, N. Carlin, R.T. de Souza, Y.D. Kim, W.G. Lynch, T. Murakami, G. Poggi, D.P. Sanderson, M.B. Tsang, H.M. Xu, S. Pratt, D.E. Fields, K. Kwiatkowski, R. Planeta, V.E. Viola, Jr., and S.J. Yennello, Phys. Rev. Lett. 65, 2114 (1990).

[Gon90c] W.G. Gong, N. Carlin, C.K. Gelbke, and R. Dayton, Nucl. Instr. and Meth. A287 (1990) 639.

[Gon91a] W.G. Gong, W.Bauer, C.K. Gelbke, and S. Pratt, Phys. Rev. C43, 781 (1991).

[Gon91b] W.G. Gong, C.K. Gelbke, W. Bauer, N. Carlin, R.T. de Souza, Y.D. Kim, W.G. Lynch, T. Murakami, G. Poggi, D.P. Sanderson, M.B. Tsang, H.M. Xu, D.E. Fields, K. Kwiatkowski, R. Planeta, V.E. Viola, Jr., S.J. Yennello, and S. Pratt, Phys. Rev. C43, 1804 (1991).

[Gro82] D.H.E. Gross, L. Satpathy, T.C. Meng, and M. Satpathy, Z. Phys. A309, 41 (1982).

[Gro85] D.H.E. Gross and X.Z. Zhang, Phys. Lett. 161B, 47 (1985).

[Gro86] D.H.E. Gross, X.Z. Zhang, and S.Y. Xu, Phys. Rev. Lett. 56, 1544 (1986).

[Gro88] D.H.E. Gross, Phys. Lett. B203, 26 (1988).

[Gut82] H.H. Gutbrod, A.I. Warwick, and H. Wieman, Nucl. Phys. A387, 177c (1982).

[Har87] J.W. Harris, B.V. Jacak, K.H. Kampert, G. Claesson, K.G.R. Doss, R. Ferguson, A.I. Gavron, H.A. Gustafsson, H. Gutbrod, B. Kolb, F. Lefebvres, A.M. Poskanzer, H.G. Ritter, H.R. Schmidt, L. Teitelbaum,

M. Tincknell, S. Weiss, H. Wieman, and J. Wilhelmy, Nucl. Phys. A471, 241c (1987).

[Har88] "Harshaw Crystal Optics",Engelhard Cooporation, p21 (1988).

[Hil89] D. Hilscher, H. Rossner, B. Cramer, B. Gebauer, U. Jahnke, M. Lehmann, E. Schwinn, M. Wilpert, Th. Wilpert, H. Frobeen, E. Mordhorst, and W. Scobel, Phys. Rev. Lett. 62, 1099 (1989).

[Hir84] A.S. Hirsch, A. Bujak, J.E. Finn, L.J. Gutay, R.W. Minich, N.T. Porile, R.P. Scharenberg, B.C. Stringfellow, and F. Turkot, Phys. Rev. C29 508 (1984).

[Hur85] C.R. Hurlbut, "Plastic Scintillators, A Survey", Bicron (1985).

[Jaca87] B.V. Jacak, G.D. Westfall, G.M. Crawley, D. Fox, C.K. Gelbke, L.H. Harwood, B.E. Hasselquist, W.G. Lynch, D.K. Scott, H. Stöcker, M.B. Tsang, G. Buchwald, and T.J.M. Symons, Phys. Rev. C35, 1751 (1987).

[Jacq85] D. Jacqet, J. Galin, B. Borderie, D. Gardes, D. Guerreau, M. Lefort, M Monnet, M.F. Rivet, X. Tarrago, E. Duek, and J.M. Alexander, Phys. Rev. C32, 1594 (1985).

[Jaq83] H. Jaqaman, A. Mekjian, L. Zamick, Phys. Rev. C27, 2782 (1983).

[Kes69] S. Keszthelyi-Landori and G. Hrehuss, Nucl. Instr. and Meth A68, 9 (1969).

[Kim89] Y.D. Kim, M.B. Tsang, C.K. Gelbke, W.G. Lynch, N. Carlin, Z. Chen, R. Fox, W.G. Gong, T. Murakami, T.K. Nayak, R.M. Ronningen, H.M. Xu, F.Zhu, W. Bauer, L.G. Sobotka, D. Stracener, D.G. Sarantites, Z. Majka,V. Abenante, and H. Griffin, Phys. Rev. Lett. 63, 494 (1989).

[Kim91a] Y.D. Kim, R.T. de Souza, D.R. Bowman, N. Carlin, C.K. Gelbke, W.G. Gong, W.G. Lynch, L. Phair, M.B. Tsang, F. Zhu, and S. Pratt, Phys. Rev. Lett. 67, 14 (1991).

[Kim91b] Y.D. Kim, R.T. de Souza, C.K. Gelbke, W.G. Gong, and S. Pratt, to be published

[Kno89] G.F. Knoll "Radiation Detection and Measurement", second edition, John Wiley & Sons, New York, (1989).

[Koo77] S.E. Koonin, Phys. Lett. 70B, 43 (1977).

[Kop72] G.I. Kopylov and M.I. Podgoretskii, Sov. J. Nucl. Phys. 15, 219 (1972).

[Len86] R.J. Lenk and V.R. Pandharipande, Phys. Rev. C34, 177 (1986).

[Lev84] S. Levit and P. Bonche, Nucl. Phys. A437, 426 (1984).

[Lit80] U. Littmark and J.F. Ziegler, "Handbook of Range Distributions for Energetic Ions in All Elements", Volume 6 of "The Stopping and Ranges of Ions in Matter", edited by J.F. Ziegler, Pergamon Press, New York, 1980.

[Lyn87] W.G. Lynch, Ann. Rev. Nucl. Part. Sci. 37, 493 (1987).

[Man62] W.W. Managan, IRE Trans. Nucl. Sci. NS-9,3 (1962) 8.

[Mes61] A. Messiah, "Quantum Mechanics" vol. 1, North-Holland (1961).

[Mey78] D. Meyerhofer, J. Appl. Phys. 49 (1978) 3993.

[Min82] R.W. Minich, S. Agarwal, A. Bujak, J. Chuang, J.E. Finn, L.J. Gutay, A.S. Hirsch, N.T. Porile, R.P. Scharenberg, B.C. Stringfellow, Phys. Lett. 118B, 458 (1982).

[Mor75] L.G. Moretto, Nucl. Phys. A247, 211 (1975).

[Mor88] L.G. Moretto and G. Wozniak, Prog. Part. and Nucl. Phys. 38, 401 (1988).

[Ngo89] C. Ngô, H. Ngô, S. Leray, and M.E. Spina, Nucl. Phys. A499, 148 (1989).

[Nor87] E. Norbeck, T.P. Dubbs, and L.G. Sobotka, Nucl. Instr. and Meth. A262 (1987) 564.

[Pan84] A.D. Panagiotou, M.W. Curtin, H. Toki, D.K. Scott, and P.J. Siemens, Phys. Rev. Lett. 52, 496 (1984).

[Pei89] G. Peilert, H. Stöcker, W. Greiner, A. Rosenhauer, A. Bohnet, and J. Aichelin, Phys. Rev. C39, 1402 (1989).

[Pra87] S. Pratt and M.B. Tsang, Phys. Rev. C36, 2390 (1987).

[Qui59] A.R. Quinton, C.E. Anderson, and W.J. Knox, Phys. Rev. 115, 886 (1959).

[Qui89] J. Québert, R. Boisgard, P. Lautridou, D. Ardouin, D. Durand, D. Goujdami, F. Guilbault, C. Lebrun, R. Tamisier, A. Péghaire, and F. Saint-Laurent, Proceedings of the Symposium on Nuclear Dynamics and Nuclear Disassembly, held at Dallas, April 1989, edited by J.B. Natowitz, World Scientific, Singapore 1989, p. 337.

[Ran81] J. Randrup and S. Koonin, Nucl. Phys. A356, 223 (1981).

[Ric90] J. Richert and P. Wagner, Nucl. Phys A517 399 (1990).

[Sag85] H. Sagawa and G.F. Bertsch, Phys. Lett. 155B, 11 (1985).

[Sar88] D.G. Sarantites, L.G. Sobotka, T.M. Semkow, V. Abenante, J. Elson, J.T. Hood, Z. Li, N.G. Nicolis, D.W. Stracener, J. Valdes, and D.C. Hensley, Nucl. Instr. and Meth. A264 (1988) 319.

[Sau76] G. Sauer, H. Chandra, U. Mosel, Nucl. Phys. A264, 221 (1976).

[Sch84] H. Schulz, D.N. Voskresensky, and J. Bondorf, Phys. Lett. 147B, 17 (1984).

[Sch87] T.J. Schlagel, and V.R. Pandharipande, Phys. Rev. C36, 162 (1987).

[Sie83] P.J. Siemens, Nature 305, 410 (1983).

[Sne88] K. Sneppen, and L. Vinet, Nucl. Phys. A480, 342 (1988).

[Sob84] L.G. Sobotka, M.A. McMahan, R.J. McDonald, C. Signarbieux, G.J. Wozniak, M.L. Padgett, J.H. Gu, Z.H. Liu, Z.Q. Yao, and L.G. Moretto. Phys. Rev. Lett. 53, 2004 (1984).

[Sou90] R.T. de Souza, N. Carlin, Y.D. Kim, J. Ottarson, L. Phair, D.R. Bowman, C.K. Gelbke, W.G. Gong, W.G. Lynch, R.A. Pelak, T. Peterson, G. Poggi, M.B. Tsang, and H.M. Xu, Nucl. Instr. and Meth. A295, 109 (1990).

[Sta79] D. Stauffer, Phys. Rep. 54, 1 (1979).

[Sto58] R.S. Storey, W. Jack, and A. Ward, Proceedings of the Phys. Society 72 (1958) 1.

[Sur89] E. Suraud, Nucl. Phys. A495, 73 (1989).

[Tro87] R. Trockel, U. Lynen, J. Pochodzalla, W. Trautmann, N. Brummund, E. Eckert, R. Glasow, K.D. Hildenbrand, K.H. Kampert, W.F.W. Müller, D. Pelte, H.J. Rabe, H, Sann, R. Santo, H. Stelzer, and R. Wada, Phys. Rev. Lett. 59, 2844 (1987).

[Tro89] R. Trockel, K.D. Hildenbrand, U.Lynen, W.F.W. Müller, H.J. Rabe, H. Sann, H. Stelzer, W. Trautmann, R. Wada, e. Eckert, P. Kreutz, A. Kühmichel, J. Pochodzalla, and D. Pelte, Phys. Rev. C39, R729 (1989).

[Tsa89] Gong, W.G. Lynch, T. Murakami, T.K. Nayak, R.M. Ronningen, H.M. Xu, F. Zhu, L.G. Sobotka, D. Stracener, D.G. Sarantites, Z. Majka, V. Abenante, and H. Griffin, Phys. Lett. B220, 492 (1989).

[Val90] E. Valtonen, J. Peltonen, and J. Torsti, Nucl. Instr. and Meth., A286, 169 (1990)

[Vic85] A. Vicentini, G. Jacucci, and V.R. Pandariphande, Phys. Rev. C31, 1783 (1985).

[Wes76] G.D. Westfall, J. Gosset, P.J. Johansen, A.M. Poskanzer, W.G. Meyer, H.H. Gutbrod, A. Sandoval, R. Stock, Phys. Rev. Lett. 37, 1202 (1976).

[Wil91] J.L. Wile, D.E. Fields, K. Kwiatkowski, K.B. Morley, E. Renshaw, S.J. Yennello, V.E. Viola, N. Carlin, C.K. Gelbke, W.G. Gong, W.G. Lynch, R.T. de Souza, M.B. Tsang, and H.M. Xu, Phys. Lett. (1991) in print.

[Zha87] X.Z. Zhang, D.H.E. Gross, S.Y. Xu, and Y.M. Zheng, A461, 668 (1987).

[Zha87] X.Z. Zhang, D.H.E. Gross, S.Y. Xu, and Y.M. Zheng, Nucl. Phys. A461, 641 (1987).

[Zie85] "The stopping and Range of Ions in Solids", by J.F. Ziegler, J.P. Biersack, and U. Littmark, Pergamon Press, New York, 1985